

PHASE DEVELOPMENTS BETWEEN XENOTIME (YPO<sub>4</sub>)  
REFRACTORY AND AN ALKALI ALUMINOSILICATE GLASS MELT

BY

DALE M. FISHER JR.

A THESIS  
SUBMITTED TO THE FACULTY OF

ALFRED UNIVERSITY

IN PARTIAL FULFILLMENT OF THE REQUIREMENTS  
FOR THE DEGREE OF

MASTER OF SCIENCE

IN

GLASS SCIENCE

ALFRED, NEW YORK

OCTOBER, 2015

Alfred University theses are copyright protected and may be used for education or personal research only. Reproduction or distribution in part or whole is prohibited without written permission from the author.

Signature page may be viewed at Scholes Library, New York State College of Ceramics, Alfred University, Alfred, New York.

PHASE DEVELOPMENTS BETWEEN XENOTIME ( $\text{YPO}_4$ )  
REFRACTORY AND AN ALKALI ALUMINOSILICATE GLASS MELT

BY

DALE M. FISHER JR.

B.S. ALFRED UNIVERSITY (1995)

SIGNATURE OF AUTHOR \_\_\_\_\_

APPROVED BY \_\_\_\_\_

ALEXIS CLARE, ADVISOR

\_\_\_\_\_  
WILLIAM LACOURSE, ADVISORY COMMITTEE

\_\_\_\_\_  
MATTHEW HALL, ADVISORY COMMITTEE

\_\_\_\_\_  
CHAIR, ORAL THESIS DEFENSE

ACCEPTED BY \_\_\_\_\_

DOREEN D. EDWARDS, DEAN  
KAZUO INAMORI SCHOOL OF ENGINEERING

## **ACKNOWLEDGEMENTS**

My deepest gratitude goes to my parents without whom none of what I have achieved would have been possible. Your guidance and faith through these many years led me to be the person I am today and for that, there will never be a way to say thank you. My heartfelt thanks to my wife and daughter who have supported me through many difficult and challenging times throughout the course of this work.

None of this would have been possible without the support of many individuals in my professional life. Within Corning Inc., my boss, David Sonnefeld, deserves much credit and thanks for seeing in me a desire to go further and for his offer of support throughout this effort. Technically, Dr. Joe McIntosh, Joe Cukjati, Dr. William Mattingly, Dr. Bryan Wheaton, Dr. Ben Hanson, Dr. Nicolas LeBlond, Jeff Davis and Brett Abel all have provided me the greatest support in developing an understanding of the many subject areas and deserve praise for helping me through challenging questions.

Finally, through the coursework and this thesis, Dr. Alexis Clare deserves profound credit for guiding me, helping me and for the many on and off subject conversations, which I have enjoyed immensely. Your guidance, tolerance and critical thinking made this journey a valuable one.

# TABLE OF CONTENTS

	<b>Page</b>
Acknowledgements .....	iii
Tale of Contents .....	iv
List of Tables .....	v
List of Figures .....	vii
Abstract.....	xiii
<b>INTRODUCTION .....</b>	<b>1</b>
<b>LITERATURE REVIEW.....</b>	<b>4</b>
<b>EXPERIMENTAL PROCEDURE .....</b>	<b>9</b>
A. Glass Preparation .....	9
B. SEM/EDS .....	11
C. Powder XRD.....	20
D. HTXRD .....	26
E. Sessile Drop.....	31
F. EPMA.....	39
G. DSC-TGA.....	42
<b>RESULTS .....</b>	<b>43</b>
A. SEM/EDS .....	43
B. Line Scans .....	67
C. Chemical Recalculation.....	82
D. Powder XRD and HTXRD.....	85
E. Sessile Drop.....	98
F. EPMA.....	104
G. DSC-TGA.....	107
<b>DISCUSSION .....</b>	<b>110</b>
<b>CONCLUSIONS.....</b>	<b>118</b>
<b>FUTURE WORK.....</b>	<b>119</b>
<b>REFERENCES .....</b>	<b>121</b>
<b>APPENDIX .....</b>	<b>122</b>

## LIST OF TABLES

		<b>Page</b>
Table I.	727XW Glass Composition Data .....	9
Table II.	Comparison of Glass Composition Data .....	11
Table III.	Matrix for Xenotime and Glass Thermal Gradient Experiment.....	12
Table IV.	Sequence of Polishing Abrasives used During Sample Preparation .....	20
Table V.	Six Samples Were Prepared for XRD Samples .....	25
Table VI.	Xenotime XRD Powder Samples Firing Schedule .....	25
Table VII.	Firing Schedule for Sheet Fusing .....	34
Table VIII.	Seven Samples run During the Sessile Drop Tests .....	37
Table IX.	Isothermal Sessile Drop Tests at 950 °C .....	39
Table X.	Nine Species Scanned for in the Samples on the JEOL Superprobe .....	41
Table XI.	Nine Species Matched to Three Standards .....	41
Table XII.	Point Spectrum Data from Region of Devitrification.....	53
Table XIII.	Point Spectrum Data from Region of Devitrification.....	55
Table XIV.	Line Scan Parameters .....	67
Table XV.	Estimated Elemental Concentrations in Regions 3 and 4 .....	72
Table XVI.	Line Scan Data at 5 μm is Compared to Point Spectrum Data.....	75
Table XVII.	Line Scan Data at 10 μm is Compared to Point Spectrum Data.....	76

Table XVIII.	Line Scan Data at 27 $\mu\text{m}$ is Compared to Point Spectrum Data .....	77
Table XIX.	Line Scan Data at 33 $\mu\text{m}$ is Compared to Point Spectrum Data .....	78
Table XX.	Chemical Recalculation for Sampled Data .....	82
Table XXI.	Long Duration Chemical Data .....	84
Table XXII.	Commercial Chemical Recalculation Software .....	85
Table XXIII.	Phases Identified in XRD Samples .....	86

## LIST OF FIGURES

	<b>Page</b>
Figure 1. Isopipe design for the fusion glass process as referenced in US8028544 B2. ....	2
Figure 2. Geometric configuration for an isopipe. ....	3
Figure 3. For ABX <sub>4</sub> REE compounds, crystal structure stability is represented as a function of A and B ionic radius. ....	5
Figure 4. Creep rate as a function of TiO <sub>2</sub> content. ....	6
Figure 5. Glass forming region in the yttrium aluminosilicate system. ....	8
Figure 6. Micrographs taken from two samples used to characterize glass composition. ....	10
Figure 7. Refractory sample positioned in the Pt/Rh 20 mil boat in cross section. ....	13
Figure 8. Gradient boat cross section with cullet added. ....	13
Figure 9. Lateral and longitudinal cross sections of gradient furnace. ....	14
Figure 10. Tube furnace arrangement with thermocouple probe inserted into the sample tube (a.). ....	15
Figure 11. The platinum boat with glass and refractory sample in the line transfer device. ....	15
Figure 12. Loctite super glue applied liberally on the exposed glass surface. ....	16
Figure 13. Glass and refractory sample following extraction from the platinum boat. ....	16
Figure 14. Loctite Double Bubble two-part epoxy used to maintain the sample integrity. ....	17

Figure 15.	Struers low speed diamond cut saw used for sample preparation.....	17
Figure 16.	The three pieces from each sample oriented on slide.....	18
Figure 17.	Permabond ET515 epoxy used to secure sample to slide.....	19
Figure 18.	Samples were polished for SEM characterization.....	19
Figure 19.	Buehler Petrothin thin sectioning system used for the initial grind on the samples. ....	20
Figure 20.	PSD for xenotime sample, first run. ....	22
Figure 21.	PSD for xenotime sample, second run.....	22
Figure 22.	PSD for xenotime sample, third run. ....	23
Figure 23.	PSD for xenotime sample, fourth run. ....	24
Figure 24.	PSD for xenotime sample, fifth run.....	25
Figure 25.	Finished samples for XRD characterization. ....	26
Figure 26.	Sample prepared for HTXRD measurements. ....	28
Figure 27.	Slide for HTXRD shown in holder.....	29
Figure 28.	HTXRD firing schedule.....	30
Figure 29.	HTXRD sample following scanning. ....	31
Figure 30.	Definition of coordinate system used in digitized software solver <sup>21</sup> .....	33
Figure 31.	Firing schedule set-point plotted with the actual control temperature for the glass sheet fusing procedure. ....	35
Figure 32.	Core drilled, fused sheet. ....	35
Figure 33.	Thermolyne 59300 tube furnace (a.) and data collection server .....	36

Figure 34.	NI Vision builder user interface used to capture images and control the imaging system. ....	37
Figure 35.	Sessile drop sample arrangement during testing. ....	38
Figure 36.	A sampling of micrographs are shown from the time/temperature matrix.....	45
Figure 37.	Micrograph displaying reaction layer.....	46
Figure 38.	Point spectrum data of base refractory and light phase. ....	46
Figure 39.	Point spectrum data of mid-level and dark grey phases. ....	47
Figure 40.	Point spectrum data of dark grey and glassy phases. ....	48
Figure 41.	Point spectrum data for the five primary phases. ....	49
Figure 42.	Point spectrum data compiled for all samples run at 24 h. ....	51
Figure 43.	Devitrification near reaction interface. ....	52
Figure 44.	High magnification of devitrification near interface. ....	53
Figure 45.	Devitrification and sack development near interface. ....	54
Figure 46	Phase diagram of REO, alumina and silica.....	56
Figure 47.	Cloudy regions observed near reaction interface. ....	57
Figure 48.	Elemental maps for Y and P. ....	57
Figure 49.	Elemental maps for Ca and Mg.....	58
Figure 50.	Elemental maps for Si, Al and K.....	59
Figure 51.	Elemental map for Na.....	60
Figure 52.	Micrograph of chemical map region. ....	61
Figure 53.	Elemental maps for P and Y. ....	62

Figure 54.	Elemental map for Si. ....	62
Figure 55.	Elemental map for Ca. ....	63
Figure 56.	Elemental maps for Al, K and Na. ....	64
Figure 57.	Micrograph of chemical map region. ....	65
Figure 58.	Elemental maps for P, Y, Si, Al, Na, K, Ca.....	66
Figure 59.	Line scan data for all elements with regions indicated.....	68
Figure 60.	Line scan data for select elements.....	69
Figure 61	Full matrix of line scan plots in wt% oxide. ....	71
Figure 62.	Plot of Y depleted layer thickness. ....	73
Figure 63.	Line scan data is plotted.....	74
Figure 64.	Micrograph for point spectrum 75.....	79
Figure 65.	Matrix of line scans converted to mol %. ....	81
Figure 66.	Micrograph from long duration spectral scan. ....	83
Figure 67.	Room temperature powder XRD trace with phase ID.....	88
Figure 68.	Powder XRD trace with phase ID. ....	88
Figure 69.	Powder XRD trace with phase ID. ....	89
Figure 70.	Powder XRD trace with phase ID. ....	89
Figure 71.	Powder XRD trace with phase ID. ....	90
Figure 72.	Powder XRD trace with phase ID. ....	90
Figure 73.	Powder XRD trace with phase ID. ....	91

Figure 74.	Matrix of XRD traces. P-7 (a., b.), FC-01 (c., d.), XB-1 (e., f.).	92
Figure 75.	HTXRD trace with phase development.	94
Figure 76.	3-D plot of HTXRD scans.	95
Figure 77.	HTXRD scans are plotted in a 2-D overlay.	96
Figure 78.	Room temperature scan of HTXRD sample.	97
Figure 79.	Sessile drop slumping.	98
Figure 80.	User interface of the Sessile drop image analysis software.	99
Figure 81.	Contact angles as measured during the sessile drop experiments for the 727XW glass	100
Figure 82.	Contact angles as measured for SLS and 727XW glass compositions with xenotime	101
Figure 83.	Sessile drop tests showed remarkably different wetting behavior between the A-1148.	102
Figure 84.	Calculated interfacial tension for the 727XW on xenotime samples at varied temperature.	103
Figure 85.	Calculated interfacial tension measurements for the SLS and 727XW glass compositions.	104
Figure 86.	EPMA micrograph showing four regions of interest.	106
Figure 87.	Data from EPMA characterization corresponding to scan locations indicated in Figure 88.	107
Figure 88.	DSC-TGA data recorded on xenotime sample from ambient to 1400 °C.	108
Figure 89.	DSC-TGA data recorded on 727XW sample from ambient to 1400 °C.	109
Figure 90.	DSC-TGA data recorded on 727XW with xenotime sample from ambient to 1400 °C	109

Figure 91.	A binary phase diagram of Glass A-B. Refractory is component A. ....	111
Figure 92.	Line scan data plotted relative to alkaline and alkali earth species. ....	114

## ABSTRACT

Xenotime ( $\text{YPO}_4$ ) has been identified as a possible refractory solution to the need for creep resistant refractory materials used in fusion draw isopipes. This is driven by the continued demand for larger substrate sizes for the display panel industry. Previous testing of xenotime against certain alkali aluminosilicate glass compositions revealed significant dissolution and new phase development when in contact with such glass compositions. Xenotime was tested against an alkali aluminosilicate glass composition at typical sheet forming temperatures (1050- 1450 °C) for durations of 24, 72 and 168 h. SEM/EDS and EPMA characterization methods were used to evaluate the migration of refractory and glass components and to determine chemistry to aid in phase identification at the reaction interface layers. Data revealed significant penetration into the base refractory by Ca and distinct developments of different phases throughout the reaction layer and in the glassy matrix. Line scans were compiled from both lower and upper temperature samples to evaluate species migration between the refractory and glass. Chemical mapping was performed to reveal the spatial distribution of species and compositional zoning within the samples. Powder XRD samples were prepared from mixtures of glass and xenotime that were heated at 1150 °C and 1400 °C for 24 and 72 h and evaluated for specific phase identification. Calcium potassium phosphate,  $\text{Ca}_{10}\text{K}(\text{PO}_4)_7$  and calcium yttrium oxide silicate  $\text{Ca}_4\text{Y}_6\text{O}(\text{SiO}_4)_6$  phases were identified from scans performed on powder XRD samples.

## INTRODUCTION

During the growth period of the past fifteen years, flat screen glass manufacturers have continued to strive for ever larger product size. Several factors drive this trend. First and foremost, larger size displays command a higher price range. These larger LCD sizes can effectively compete with alternative displays for an appreciable share of the market. Larger size manufacturing also provides the manufacturer with some degree of versatility as these larger production processes not only produce the larger display sizes but smaller displays as well. This gives the producer significant advantages in economies of scale from which to leverage on. It is well known that Corning Inc. produces LCD substrates through the fusion draw process. At the heart of this process is the isopipe, a wedge like structure made of a monolithic refractory precisely ground to a specified prescription to achieve even mass flow distribution at a particular flow rate (Figure 1).

This process may be more specifically described as an overflow downdraw fusion process. Molten glass passes from the delivery system of the melting process and into a trough created by two weirs on either side of the isopipe. As the glass overflows the two weirs, two separate but uniformly distributed glass flows are established which then meet at the root of the isopipe where they fuse together creating a single fused sheet of substrate. The external surfaces of the glass remain pristine in this process and ideal for LCD manufacture, as they have never been in direct contact with refractory or other forming implements.

The high temperatures involved with the fusion process, approximately 1200 °C, and the design which provides support only from the ends of the isopipe, leaving the length suspended, subject this refractory monolith to potential for significant creep. Initially this characteristic behavior can lead to non-uniform flow distributions as the weirs deflect vertically downward from their nominal positions thereby impacting final product attributes. In the long term, if left unmitigated, this behavior can cause the need for a premature repair, downtime, significant expense and lost revenue.

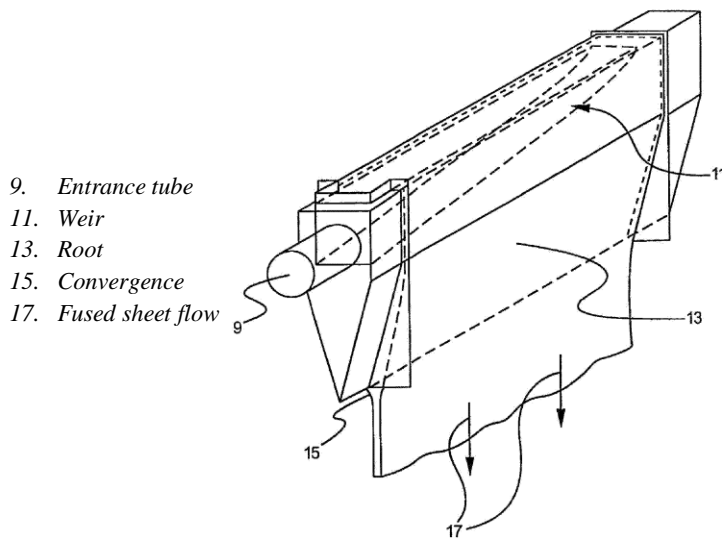


**Figure 1. Isopipe design for the fusion glass process as referenced in US8028544 B2.<sup>1</sup>**

It is well known and understood that the rate of deflection of a beam under load increases with length, time and temperature. Current trends in the industry call for larger substrates as discussed earlier. Additionally, increased temperature requirements to manufacture new, harder to melt glass compositions are being imposed on the industry to arrive at improved product attributes, both of which lead to a need for the development of more creep resistant refractory materials.

In order to withstand these demanding conditions and requirements, isopipes in use today have been fabricated from isostatically pressed refractory blocks. Zircon represents the current state of the art in refractory technology for fusion draw processes<sup>1</sup>, but its use is limited in two ways. First, zircon dissolves into the glass in the higher temperature regions, typically from the weirs, and then this dissolved zircon precipitates as secondary zircon crystals in colder regions near the root of the pipe.

This mechanism has been a source of significant concern and losses for the industry. These secondary crystals are sheared off by the shearing force from the glass flow, becoming solid inclusions in the finished product. It has been discovered by maintaining a  $\Delta T$  of less than 100 °C from weir to root<sup>1</sup>, that this mechanism can be controlled. This constraint greatly restricts the possibility of new glass compositions being implemented as only glasses of a specific viscosity curve can be produced under

this condition. The development of an isopipe material that does not possess this constraint would open up a much greater glass composition operating window.

Second, zircon restricts the operating temperature and lifetime of an isopipe due to limitations of its high temperature creep resistance properties. Creep can be attributed to stress relief and results in a permanent change in shape of a material at elevated temperatures. Grain boundary sliding or material diffusion act in a way to relieve stresses resulting in the deformation of the refractory from the desired shape. Specific to an isopipe which is fixed at both ends, suspended along its length and may exceed 15,000 pounds, the maximum stresses are encountered in the mid-point of the body. Deformation causes uneven vertical displacement of the weirs resulting in a change in the mass distribution of glass flow as described earlier. This alters the sheet thickness profile and eventually drives the glass sheet out of the quality specifications.

The rate of deformation of an isopipe is proportional to the length “L” of the body raised to the fourth power and is inversely proportional to the square of its height “H”, Figure 2.<sup>2</sup> Doubling the length of the isopipe would require an increase in its height. To enable this increase in length, the required increase in height would exceed the practical limits for the manufacture of such a large monolith and even if possible, would exceed the practical limitations for installation into the forming process. The maximum length for isopipes fabricated from zircon therefore have either been reached, or will shortly be achieved with current technology.

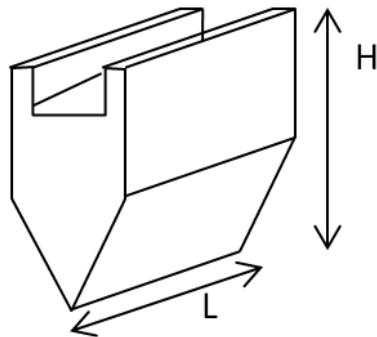


**Figure 2. Geometric configuration for an isopipe.**

## LITERATURE REVIEW

Xenotime occurs naturally, is chemically stable in most geological environments and has been found to be relatively insoluble in glass melts.<sup>3,4</sup> Xenotime grows in low to granulite-grade metamorphic rocks and is common in peraluminous rocks. It is a rare-earth element phosphate mineral (REEPO<sub>4</sub>) of which the major constituent is yttrium orthophosphate (YPO<sub>4</sub>). The reported melting temperature is 2150 °C.<sup>5</sup> As is the case with zircon, xenotime is classified as a NORM (naturally occurring radioactive material) due to it containing small amounts of Th, U and Ra. Specimens may be strongly or weakly radioactive. Xenotime also grows over a broad range of temperatures and pressures giving it a distinct advantage over monazite in the application of geochronological dating.<sup>6</sup>

Xenotime, is isostructural with ZrSiO<sub>4</sub> and lies at one end of a compositional solid solution with monazite (Ce, La) PO<sub>4</sub>, Figure 3. The charge coupled substitution for Zr<sup>+4</sup> is Y<sup>+3</sup> and for Si<sup>+4</sup> it is P<sup>+5</sup>. Xenotime has been used as a complement or alternative to monazite or zircon in geochemical studies.<sup>7</sup> Smaller, heavy rare-earth orthophosphates adopt the xenotime structure preferably to the monazite structure which is the stable form for the larger, light rare-earth orthophosphates such as (La,Nd)CEPO<sub>4</sub>. The Lanthanum contraction explains this seemingly contradictory behavior of size and weight and can be referenced outside of this work.<sup>8</sup> Although Y itself is not part of the lanthanide series it is often referred to in similar context owing to similar properties.

The xenotime structure is less common than is monazite. It is suggested that this may be in part due to the bulk rock composition in which it is not stable but also may be as a result of less likely identification owing to the smaller grain size.

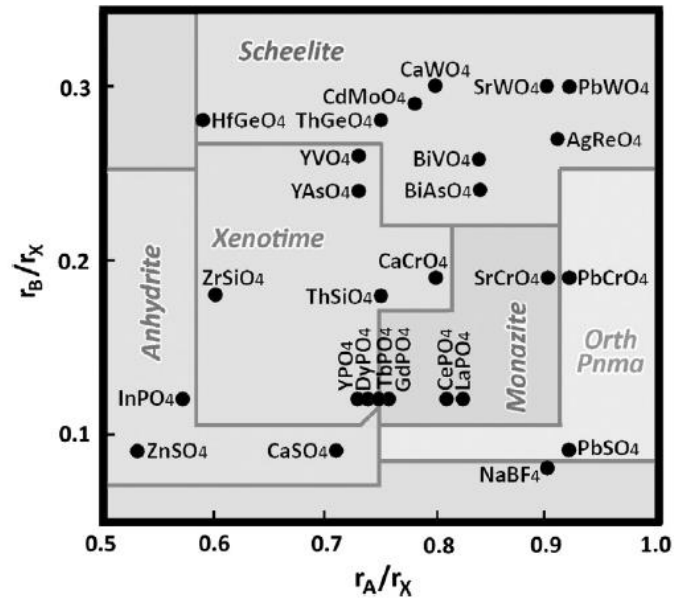


Figure 3. For  $ABX_4$  REE compounds, crystal structure stability is represented as a function of A and B ionic radius.<sup>9</sup>

Both xenotime and zircon belong to the tetragonal space group with less than a 3 % difference in their lattice volumes. Y resides in an eight-fold oxygen coordinated polyhedron in the xenotime structure whereas the rare-earth cations of monazite reside in a nine-fold coordination. As already mentioned, xenotime structures are common for smaller, heavy rare-earth elements (Gd to Lu). It has also been noted that slightly larger, light rare-earth elements (LREE) (La to Eu) may be accommodated in the structure so long as no more than 50 % of sites are occupied by LREE's. Additionally, a number of simple isostructural substitutions may occur for xenotime's phosphate ion, (e.g.  $YAsO_4$ ).<sup>7</sup> Crystallographically less favorable, it has been recorded that the  $Ca^{2+}$  ion can fill the xenotime cation site, though rarely filling more than 10 % of sites.<sup>10</sup>

Of particular interest here is the need for a suitable high temperature, creep resistant material with the capability of being machined which is stable with a variety of glass compositions. Current technology creates an isopressed monolith for isopipe applications. Significant tooled machining is necessary to produce the finished piece from the as formed blank. Deformation mechanisms have been recorded in xenotime which include one deformation twinning mechanism and a variety of slip systems.<sup>11</sup> The

resulting ductility induced in the material by these mechanisms makes REPO<sub>4</sub> structures machinable.

Xenotime has also been studied for its capability in the formation of ceramic composites suitable for application in oxidizing environments at high temperatures.<sup>12</sup> It is claimed that use of xenotime or monazite as a weak bond interphase between the composite constituents increases the fracture toughness of high temperature composites that remain stable in high temperature, oxidizing environments. This work has continued in the development of fiber coatings to promote crack deflection and fiber pullout in oxide-oxide ceramic matrix composites.<sup>13</sup>

Two issues to be addressed in their application are the thermo-mechanical stability of fiber coatings controlled by coating CTE and the high temperature microstructural instability of coatings. Current technology experiences fiber strength degradation due to high temperature stress corrosion. Fibers tested with a two-phase xenotime-monazite composite demonstrated that they were capable of retaining their strength following heat treatments<sup>13</sup>.

As previously mentioned, the creep resistance of fusion draw isopipe refractory materials is of considerable interest. Developmental work has been performed to understand and improve creep properties of the current zircon refractory.<sup>14</sup> It was found that TiO<sub>2</sub> content in the zircon of between 0.2 and 0.4 wt% resulted in isopipes with a lower creep rate than those with constituents outside of those boundaries, Figure 4.

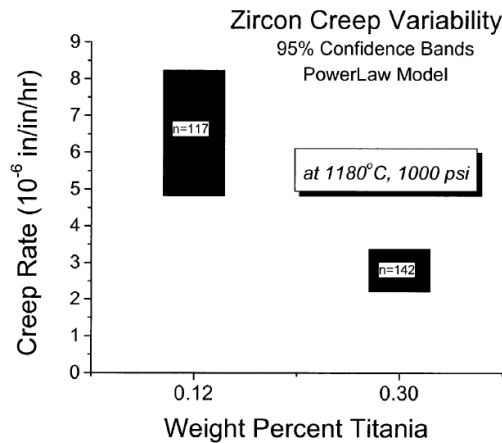


Figure 4. Creep rate as a function of TiO<sub>2</sub> content.<sup>14</sup>

Nevertheless, as temperatures required for fusion draw processes increase with new glass compositions and demands for larger substrate mounts, zircon as the material of choice for such applications possesses a limited future.

It has been stated that xenotime has been claimed as a possible replacement for the current zircon material utilized in the fusion draw process.<sup>15</sup> Until recently, studies of xenotime have been limited to theoretical understanding. To the best of the author's knowledge, xenotime has not been used as a refractory material in any commercial glass manufacturing applications. There are however references to xenotime in patent literature beyond those cited in this work. See U.S. Patent application publications Nos. 2002/0189496, 2003/0035907 and 2004/0020568. It is not claimed in any of these however, that xenotime can be used as a refractory glass contact material.

In 2008 Corning Incorporated initiated a program to pursue an understanding of xenotime and determine the feasibility of its use as a refractory isopipe material. Testing efforts initially focused on mechanical properties and understanding prior to being expanded into glass and refractory compatibility studies for current and projected glass compositions.

Developments for a scale-up from laboratory-oriented samples to production oriented samples were performed.<sup>16</sup> X-block 1 (to be referred to as XB-1 throughout this work) was the first attempt at this and resulted in significant stoning and dissolution of the refractory when in contact with certain glass compositions. Efforts to understand the reactions at the glass/refractory interface were abandoned, although significant interest in understanding the dissolution process and phase developments experienced during that effort remained. One glass composition, an alkali aluminosilicate, Corning glass code 727XW, resulted in significant dissolution of the xenotime refractory. With the permission of Corning Inc., samples of this glass were acquired together with samples of XB-1 for the purpose of developing an understanding of the dissolution process and to identify phases developed during the interaction of XB-1 and 727XW glass at typical forming temperatures.

Little work has been conducted or published in the area of combining rare earth element refractories with glass melt applications. Even less has been produced specific to applications with alkali aluminosilicate glass melts. What has been published suggests a

rare earth refractory glass composition, in fact among the most refractory reported, with use temperatures in excess of 900 °C.<sup>17</sup> Other than vitreous silica, there are very few glass compositions which can exceed these temperatures. Glasses in the high silica region of glass formation for the ternary system of  $Y_2O_3$ - $Al_2O_3$ - $SiO_2$  (YAS), have demonstrated phase separation and crystallization, Figure 5. When combining the 727XW alkali aluminosilicate glass with the xenotime refractory at elevated temperatures, this may prove detrimental to desirable drawn glass quality due to stoning potential.

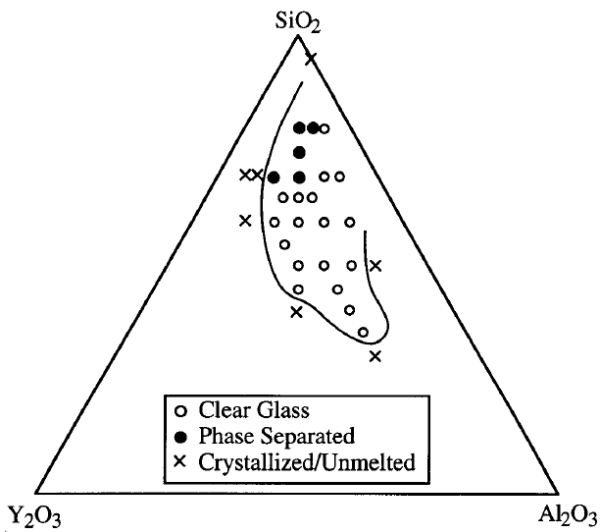


Figure 5. Glass forming region in the yttrium aluminosilicate system.<sup>17</sup>

Significant efforts continue to be made towards developing improved materials for use in glass fusion operations. Despite early failures in glass compatibility with xenotime for this application, there remains promise for its use in glass manufacturing applications. A high level of refractoriness has been demonstrated and only certain glass compositions have exhibited accelerated corrosion. This current work will revisit the application of xenotime in contact with an alkali-aluminosilicate glass at glass fusion temperatures and conditions. Phase developments at the reaction interface will be characterized and identified.

# EXPERIMENTAL PROCEDURE

## A. Glass Preparation

Glass samples of an alkali aluminosilicate composition, Corning glass code 727XW (Table I), were obtained from Corning Incorporated. Alkali aluminosilicate glass compositions are typically used today for many chemically strengthened glass products. The most famous of which being Gorilla<sup>®</sup> glass which can be found on many electronic hand held devices. These chemically strengthened glass products achieve their high level of strength and scratch resistance through a process which exchanges Na ions for larger K ions to create compression in the surface layer.

Table I. 727XW Glass Composition Data

<i>727XW</i>	<i>wt. %</i>	<i>mol %</i>
<b>Al<sub>2</sub>O<sub>3</sub></b>	19.73	13.01
<b>CaO</b>	2.63	3.154
<b>Fe<sub>2</sub>O<sub>3</sub></b>	.02	.008
<b>K<sub>2</sub>O</b>	5.74	4.1
<b>MgO</b>	1.88	3.14
<b>Na<sub>2</sub>O</b>	10.42	11.31
<b>SiO<sub>2</sub></b>	56.92	63.71
<b>SrO</b>	2.41	1.56
<b>TiO<sub>2</sub></b>	.01	.008

Glass samples were obtained in two forms; sheet and crushed cullet. Crushed cullet (having a mean particle size of 100  $\mu\text{m}$ ) was utilized as supplied for the thermal gradient boat tests. This cullet was further processed for the XRD samples to a mean particle size of 25  $\mu\text{m}$ . Glass sheets were utilized to prepare the samples used for sessile drop experiments.

Microprobe analysis was performed on the glass to gain a baseline of the glass chemistry. Two samples were chosen from the sessile drop test (refer to section E for additional details on sessile drop test) and a point spectrum was taken on each sample. The first was taken at a position approximately 300  $\mu\text{m}$  from the refractory boundary and the other at 100  $\mu\text{m}$  from the refractory boundary, Figure 6. This spectral data was

compared to composition data provided with the glass sample through Corning Inc. Data were plotted against the supplied glass compositional data (Table II). Neither Y nor P species were identified in the analysis and as the spectrums were taken from the interior of the sample, surface volatilization is not suspected to have perturbed the results.

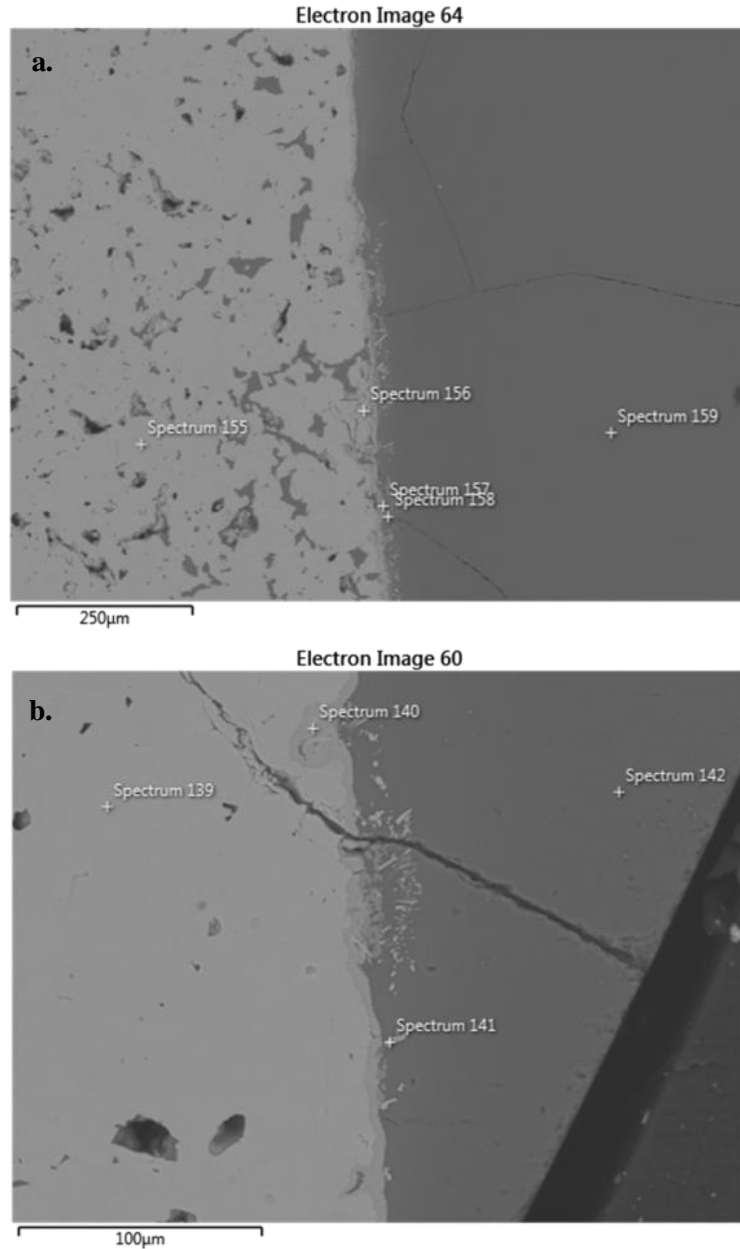
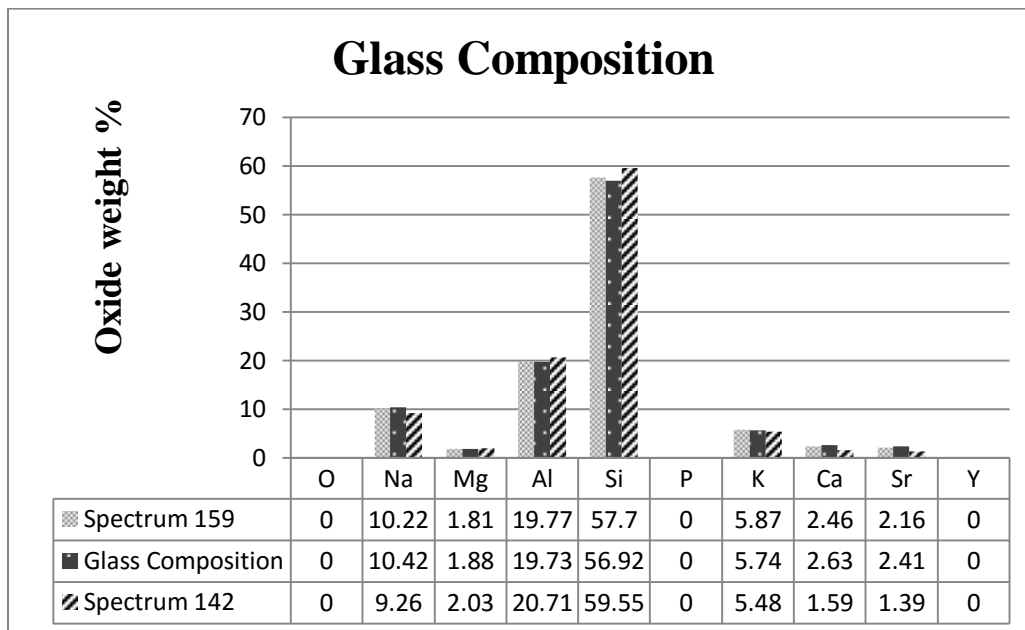


**Figure 6. Micrographs taken from two samples used to characterize glass composition.**

Table II. Comparison of Glass Composition Data



## B. SEM/EDS

Characterization of the thermal gradient boat samples was performed using a ZEISS Sigma Gemini SEM with an Oxford Instruments X-max 8mm<sup>2</sup> Schottky field emitter EDS for elemental analysis of the phase developments at the glass/refractory reaction interface. Accelerating voltage of 20 kV was typical with amperage between 200 and 500 pico-amps. The targeted working distance was 8.5 mm. Long and short duration scans were performed for both EDS mapping and line scans. Due to the number of samples, the exact parameters of each individual scan are not presented here but are available upon request.

Glass contact refractories often interact with glass melts differently at varied temperatures. Forming temperatures at which XB-1 would be expected to be in contact with glass in a fusion isopipe would be in the range of 1100-1400 °C. To facilitate the study of phases and their development associated with xenotime refractory in contact with alkali aluminosilicate glass melts, a time-temperature matrix was constructed to explore the range of temperatures where these materials are likely to operate in glass forming operations. Samples were characterized at intervals of 50 °C between 1050 °C

and 1450 °C and exposed to the furnace environment for durations of 24, 72 and 168 h (Table III). This allowed for the development of a matrix of what would be the most representative area of interest in the glass melting community.

**Table III. Matrix for Xenotime and Glass Thermal Gradient Experiment**

<i>Time (h)</i>	<i>Temperature (°C)</i>								
<b>24</b>	1050	1100	1150	1200	1250	1300	1350	1400	1450
<b>72</b>	1050	1100	1150	1200	1250	1300	1350	1400	1450
<b>168</b>	1050	1100	1150	1200	1250	1300	1350	1400	1450

As supplied, the samples of XB-1 are greater than 99 % crystalline. This level of homogeneity distinguishes this particular refractory from others as the majority of industrial refractories are a heterogeneous mixture of two or more phases with one primary crystalline phase and a secondary glassy phase filling the interstitial voids between grains. There is no distinguishable glassy phase contained within the as tested XB-1 material. The supplied XB-1 material was fabricated through cold isostatic pressing achieving a green density of 73.1 % and an as fired density of 91.3 % of theoretical. The firing temperature for XB-1 was 1750 °C. Theoretical density is 4.27 g/cc while the as fired density was measured as 3.9 g/cc. Mercury porosimetry was found to be 6.473 % with a median pore diameter of 3.35 µm. Typical closed porosity threshold is 93 % of theoretical therefore, minimal porosity of the finished piece is expected. Average grain size was reported as 13 µm.

A thermal gradient boat test was developed to provide an efficient means by which a time-temperature matrix experiment could be executed. Similar gradient tests are commonly performed to determine the liquidus temperature of glass compositions. Four refractory strips were prepared on a wet tile cutting saw. The strips were cut to 200 mm x 2.5 mm x 5 mm from the supplied refractory block, XB-1. The strips were then surface ground with a Supra 1080 surface grinder. To remove particles and cutting residues from the refractory strip, samples were then washed in an ultrasonic bath using a Branson 5510 ultrasonic cleaner with a cleaning solution of Alconox and DI water for a duration of 30 min. Samples were removed from the cleaner and allowed to air dry. Only

three of the four refractory strips were used in the testing with one being held as a back-up in the event of a failure.

727XW glass cullet was prepared by crushing samples in an automated Carver press. Glass was then sieved to a 20 mesh particle size to be used as the glass medium in contact with the refractory strips and contained within the platinum boat. Stock platinum boats from Corning Incorporated's inventory were utilized for this experiment. The platinum boats were fabricated from 80/20, platinum/rhodium alloy, with a metal thickness of 30 mil. The refractory strips were placed into the platinum boat lengthwise and on edge as shown in Figure 7.

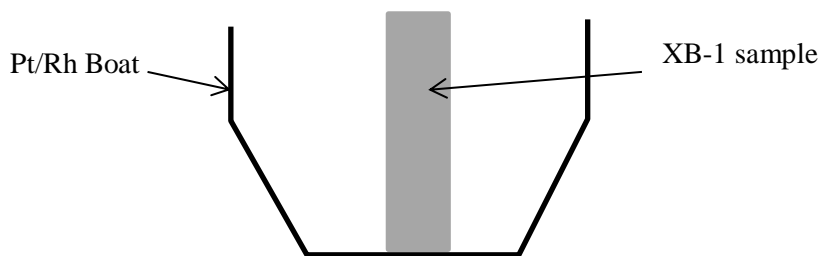


**Figure 7. Refractory sample positioned in the Pt/Rh 20 mil boat, in cross section.**

The crushed cullet was then placed in the boat so as to surround the sides of the sample but leaving the top surface of the refractory strip exposed to air (Figure 8). The refractory surface above the cullet was discarded during the sample preparation procedure.

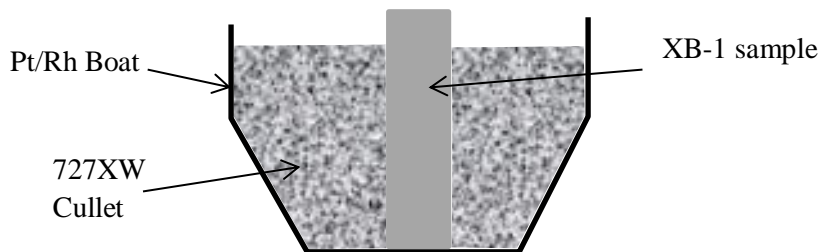


**Figure 8. Gradient boat cross section with cullet added.**

The boat, including the platinum, refractory and crushed cullet was inserted into a tube furnace which was made of a cylindrical mullite sample holder which was surrounded by a platinum wound heating element embedded in an alumina backer. The sample holder and heater were contained in refractory insulation material encased in an outer steel support casing. The design of the winding varies its turns per inch from the hot zone to the cooler zones in order to create a thermal gradient within the test cavity. The hot zone is more tightly wound than the cooler zone with the higher winding density supplying higher energy input and higher temperatures than the less tightly wound lower temperature region (Figure 9).

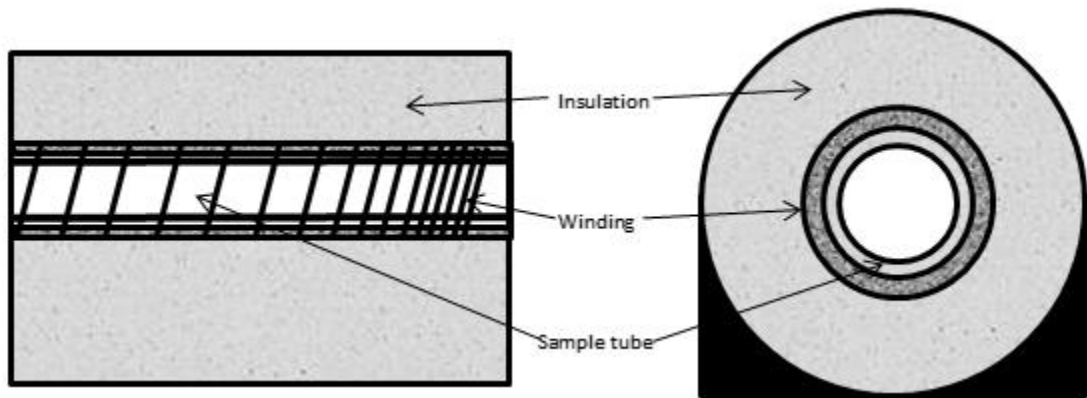


**Figure 9. Lateral and longitudinal cross sections of gradient furnace.**

Samples were loaded individually into the mullite tube of the pre-heated furnace where the sample was subjected to the desired temperature range and allowed to remain in this condition for the duration of time prescribed by the three required times of 24, 72 and 168 h. A type S thermocouple was used to probe the sample such that the position of the sample with respect to the temperature could be mapped. The thermocouple was clamped to a lab stand to secure it in a horizontal arrangement and was inserted into the furnace above the sample to map the temperature regions and recorded (Figure 10). On removal from the gradient furnace, samples were placed on a refractory holder and allowed to air cool to ambient temperature.

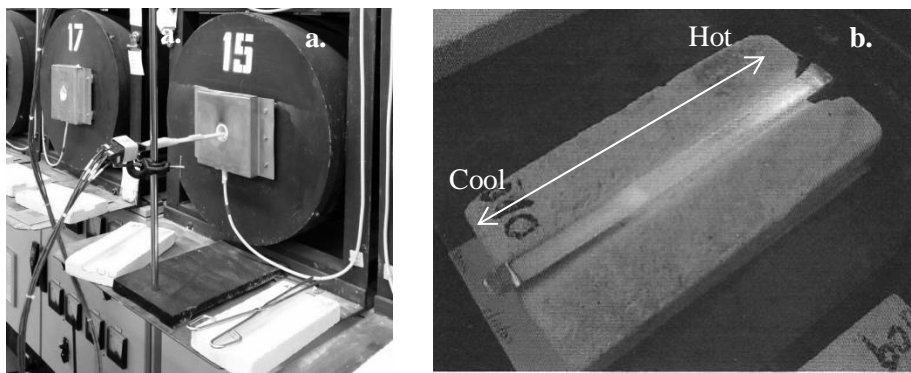


**Figure 10. Tube furnace arrangement with thermocouple probe inserted into the sample tube (a.). Sample shown removed from the furnace (b.).**

Once the sample had achieved ambient conditions, the temperature positions probed during insertion in the furnace are transposed onto the sample. This was performed prior to removing the glass and refractory from the platinum boat. An existing alignment device prepared with established reference positions that directly correlate to the thermocouple positions used during the probe process was utilized to ensure accurate and representative demarcations on the sample (Figure 11).

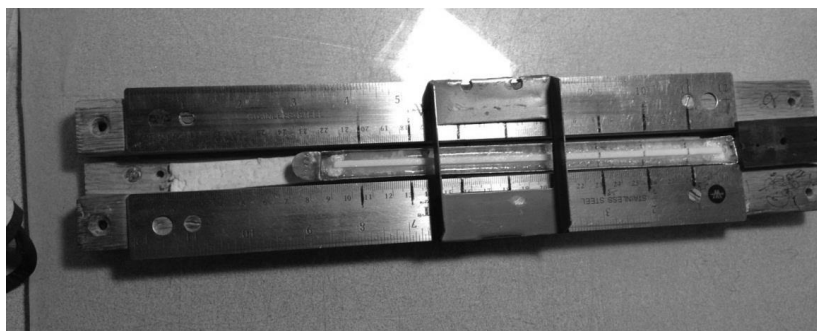


**Figure 11. The platinum boat with glass and refractory sample in the line transfer device.**

As the glass and refractory have considerably different coefficients of thermal expansion, significant cracking and separation of the glass from the refractory sample often occurs. Loctite super glue was applied to the refractory and glass surface (Figure 12) prior to extraction from the platinum boat in an effort to keep the sample intact during

removal from the platinum boat. Glue was applied liberally on the surfaces and allowed to air dry prior to extraction from the platinum boat.



**Figure 12. Loctite super glue applied liberally on the exposed glass surface.**

Once the glue was dried, the refractory and glass sample was extracted from the platinum boat. First, the walls of the platinum boat were peeled away from the glass using gloved hands and a pair of pliers. Starting at one point and working around the sample, the platinum was carefully pulled away while attempting to keep the sample strip intact. A twisting motion was then used to try to free the bottom surface from the platinum boat. Slowly and carefully, the sample was worked until it was fully released. It proved difficult to keep the sample entirely intact during this process and several pieces of samples broke off (Figure 13). All pieces were captured during the extraction process and the complete sample was maintained and reassembled during the preparation stages for characterization.



**Figure 13. Glass and refractory sample following extraction from the platinum boat.**

All three samples were prepared for characterization using the SEM in the same manner. Two of the samples had broken during the extraction process and the one that was not damaged remained extremely fragile. Each sample was treated with a two part epoxy resin, brand name Double Bubble (Figure 14) to aid in maintaining their structural

integrity during the sample preparation stage. Epoxy was mixed per the manufacturer's instructions using the included wooden mixing sticks. The same mixing sticks were used to apply epoxy to the samples. After mixing, the resin was applied over all surfaces of the samples, focusing on any areas where obvious cracks or voids existed. Samples were allowed to cure for twenty min following application of the epoxy. The minimum cure time stated by the manufacturer is three to five min. Excess epoxy was removed from the samples following curing with a razor knife.



**Figure 14. Loctite Double Bubble two-part epoxy used to maintain the sample integrity.**

Samples were prepared for mounting to a slide for characterization. All samples were cut down to lengths varying from 50 to 75 mm using a Struers low speed diamond cut saw (Figure 15). This resulted in each gradient boat strip being cut two times to create three pieces from each sample for mounting.



**Figure 15. Struers low speed diamond cut saw used for sample preparation.**

The bottom surface of each sample (side nearest to the platinum boat bottom) was to be characterized and would be the surface facing up and off the sample slide in the

final arrangement. An initial hand grinding of the bottom surface of each sample was performed by grinding on a Buehler grinder. Samples were allowed to air dry before transferring marks to the bottom surface. Recall, the initial markings for the gradient positions had been marked on the top surface prior to the removal from the platinum boat. These marks were transferred to the bottom surface by placing the samples on a stage with a square edge. The lower marks were then aligned with the edge and a new mark was placed on the corresponding location on the bottom surface, which had just been ground flat.

Each sample was then prepared for mounting to a glass slide. Prior to mixing the epoxy, each sample was arranged in an “S” type configuration in order to improve the accuracy and efficiency during scanning with the SEM (Figure 16).

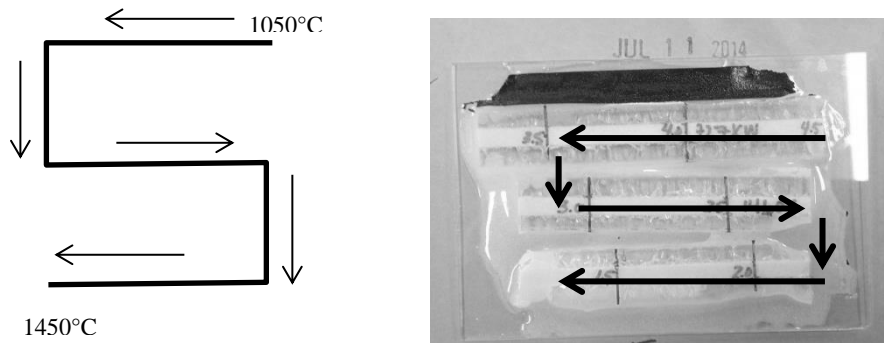


**Figure 16. The three pieces from each sample oriented on slide.**

Permabond ET515 (Figure 17) two part epoxy was utilized to secure the sample pieces to the glass slide. The slide dimensions were 2” tall by 3” wide. Each component was applied to the slide where it was mixed in place and spread evenly over the entire slide. The three pieces of each sample were then positioned on the slide in the preset “S” configuration and pressed into the epoxy. Samples were allowed to dry and cure for 24 h.



**Figure 17. Permabond ET515 epoxy used to secure sample to slide.**

Following the required one day drying time, all three of the samples were prepared for polishing on a Struers Tegramin 30 polisher (Figure 18). An initial cut was made to each sample on a Buehler Petrothin thin sectioning system (Figure 19). Samples were aligned such that the exposed surface would be cut flat and parallel to one another in preparation for sample polishing. The three samples were mounted into a carbon sample holder and pressed into the Struers specimen mover plate. This aligned all surfaces parallel with one another, on the same plane, to ensure even polishing.



**Figure 18. Samples were polished for SEM characterization on a Struers Tegramin 30.**

The specimen mover plate was inserted into the Struers Tegramin 30 grinding and polishing machine for polishing. A series of pads were utilized during the sample polishing (Table IV). Upon completion of the polishing sequence, samples were removed from the holder. Samples were washed and allowed to air dry. The samples were then removed from the sample mounts prior to washing with deionized water and allowed to air dry.

Table IV. Sequence of Polishing Abrasives used During Sample Preparation

<i>Sequence</i>	<i>1</i>	<i>2</i>	<i>3</i>	<i>4</i>	<i>5</i>	<i>6</i>	<i>7</i>
<b>Grit</b>	80	220	500	1200	2000	4000	1 $\mu\text{m}$



Figure 19. Buehler Petrothin thin sectioning system used for the initial grind on the samples.

### C. Powder XRD

Identification of the phases developed between the 727XW glass and the xenotime refractory was of primary importance to this effort. In addition to the elemental analysis that was performed with the SEM/EDS, efforts were made to prepare samples for XRD analysis. Results of the SEM characterization were shared with Bryan Wheaton of the Corning Inc. characterization labs to determine the feasibility of performing XRD on samples of xenotime and 727XW glass. Due to the small size of the crystals found in the glassy region and the complexity of the interface region, it was determined that this would prove to be a challenging task to accomplish. It was determined that if a sample could be prepared such that a significant number of crystals were available then it may be possible to collect quantitative results. To achieve this, a new sample needed to be formed with xenotime particles interspersed throughout the glass to form a sample with significant opportunities for crystal formation.

To achieve the highest potential for crystal formation and detection with XRD, a target particle size for mixing with the glass cullet was required. A particle size that correlated with the larger crystals observed in the glassy regions from the SEM samples

would provide the best opportunity for crystal phase development and analysis. Utilizing the SEM results, 25  $\mu\text{m}$  was determined to be the approximate size of larger crystals forming in the glassy region.

A total of six samples were prepared for powder XRD analysis, two samples from the XB-1 xenotime refractory block utilized in the SEM procedure, two samples of a commercially supplied raw material to fabricate XB-1 (FC-01) and two samples of a synthesized solid state  $\text{YPO}_4$ , (P7). The commercially supplied raw material FC-01 was supplied by Molycorp/Chevron mining. The solid state sample was synthesized by Corning Inc. from phosphorous pentoxide and yttria to form yttrium phosphate:



Both the FC-01 and the P7 materials were supplied already processed to a fine powder from Corning Inc. From supplied data, the particle size of these samples was 55 % +44  $\mu\text{m}$ /-100  $\mu\text{m}$ , 20 % -44  $\mu\text{m}$  and 25 % fines ( $d_{50}$ ) =2  $\mu\text{m}$ .

Xenotime samples taken from the XB-1 xenotime block required extensive processing to achieve the target PSD. For unknown reasons, the xenotime samples proved significantly challenging in achieving a mean PSD of 25  $\mu\text{m}$ . A variety of milling and sample preparation methods were utilized, as detailed below, in the effort to create a suitable sample with a mean PSD of 25  $\mu\text{m}$ .

A xenotime sample was prepared initially by jaw crushing the sample in a Retsch model BB200 crusher to mill the material to approximately 2 mm. The material was then transferred to the ball milling apparatus and loaded into the “000” jar with ½” high purity yttria stabilized zirconia milling media. The initial attempt utilized ball milling for a duration of 3 h. Particle size analysis was performed by light scattering on a Microtrac S3500 particle size analyzer. The dispersant used was a 99 % IPA solution. Ultrasonic washing was performed for a duration of 5 min. Particle size analysis revealed a majority population distribution at 100  $\mu\text{m}$  and what appears to be a small population at approximately 10  $\mu\text{m}$ , (Figure 20).

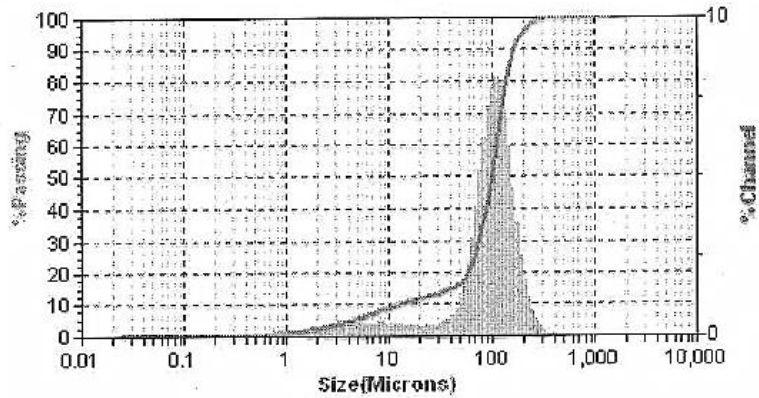


Figure 20. PSD for xenotime sample, first run.

Following the first attempt to ball mill, it was believed the duration of the procedure might have been responsible for the large particle size. A second attempt was made to achieve a 25  $\mu\text{m}$  particle size target by increasing the duration of ball milling from the initial 3 h to 8 h. The intent was to further break down the xenotime particles to achieve a smaller PSD. All other aspects of the preparation remained the same as the first attempt. The resulting PSD exhibited similar results to the first with a primary peak at the 100  $\mu\text{m}$  particle size and a secondary peak at a smaller particle size of with a distribution centered around 5  $\mu\text{m}$ . Compared to the first sample, the peak at the smaller particle size was stronger and broader, (Figure 21).

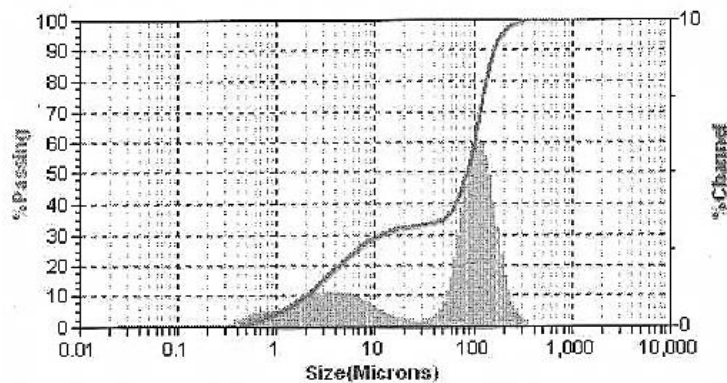


Figure 21. PSD for xenotime sample, second run.

The duration of the ball milling was increased a third time to 18 h while maintaining all other parameters the same as the first two attempts. This third iteration

greatly reduced the overall particle size but still maintained two distinct populations centered around 5  $\mu\text{m}$  and 100  $\mu\text{m}$  (Figure 22). Examination of the data revealed in fact that two populations appear to exist in the lower range centered around .9 and .8  $\mu\text{m}$ . It was promising that the particle size population on this third sample was dramatically shifted towards the lower range relative to the first two attempts but, it still did not satisfactorily achieve the objective.

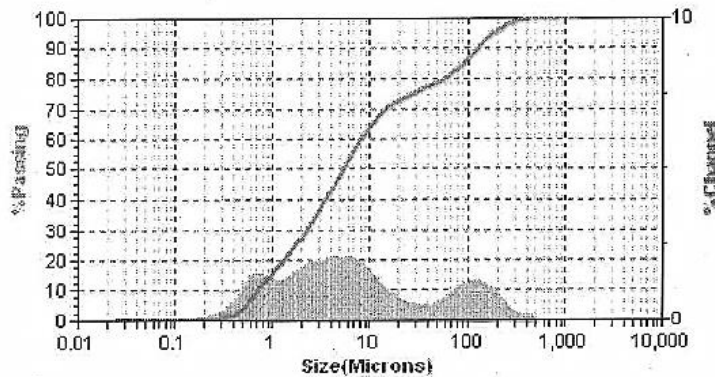
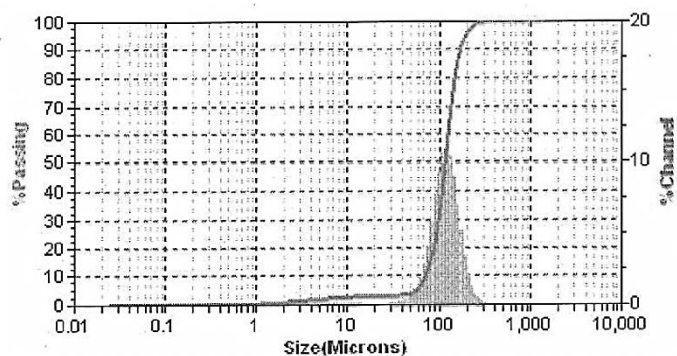


Figure 22. PSD for xenotime sample, third run.

Following the failure of the first three attempts to produce a suitable sample with a PSD centered around 25  $\mu\text{m}$ , it was believed a different method of media milling was required to achieve the 25  $\mu\text{m}$  target particle size. Individuals within the Corning particle technology group were consulted and it was recommended to perform a vibramill stage following the ball milling of the sample in order to try to eliminate the various populations in favor of the desired single population centered around 25  $\mu\text{m}$ .

A sample was prepared by initially ball milling for 8 h followed by a 1 h vibramill stage to test this suggestion. A SWECO low amplitude vibramill model M-18 was used with 1/2" high purity YTZ cylinders as the milling media in a Nalgene container, .1 mL of methanol was added as a milling aid.

Results from this first sample preparation attempt which included the vibramill step were promising as PSD analysis revealed a single population. This single population was centered around a mean value of 117.7  $\mu\text{m}$  (Figure 23) which was significantly off target from the desired 25  $\mu\text{m}$  particle size.



**Figure 23. PSD for xenotime sample, fourth run.**

Despite the larger than desired particle size, the elimination of the second population was encouraging and it was decided to continue to explore this method of sample preparation. Two additional samples were prepared and ball milled for 8 h as was done on the previous sample. Both samples were then subjected to a significantly increased duration of vibramilling. The time was increased to 42 h versus the original sample vibramill time of 1 h. Following the vibramilling operation, one of the two samples was mortar milled for 66 min while the other sample was not. Both samples were sieved to -270 using a nylon hand sieve.

As an additional alteration to the preparation method from the first four samples, the dispersant used during particle size characterization for these final two samples was altered from IPA to a 4 % Triton X100 solution. The mortar milled sample exhibited a much narrower PSD than that of the non-mortar milled sample (Figure 24). The mean particle size of this mortar milled sample was 31.73  $\mu\text{m}$  while the non-mortar milled sample was 47.43  $\mu\text{m}$ . It was concluded that the mortar milled sample with the mean particle size of 31.73  $\mu\text{m}$  would be utilized for XRD characterization as efforts to further refine the process to achieve the 25  $\mu\text{m}$  particle size would prove too costly.

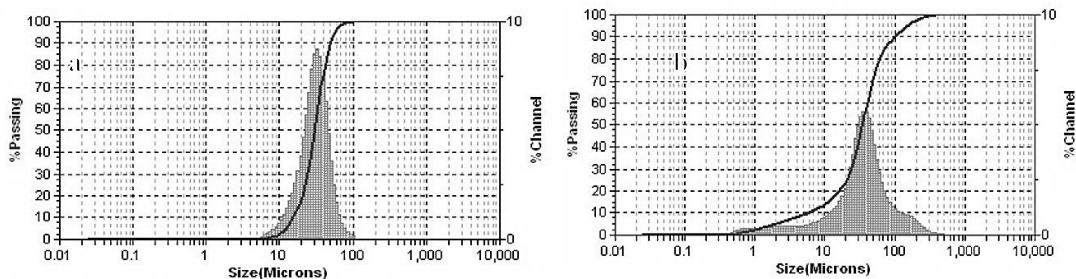


Figure 24. PSD for xenotime sample, fifth run.

All iterations of particle sample preparation are listed with their resultant PSD, (Table V).

Table V. Six Samples Were Prepared for XRD Samples

	<i>Ballmill duration (h)</i>	<i>Vibramill duration (h)</i>	<i>Mortar Mill (min)</i>	<i>Seive</i>	<i>Dispersant</i>	<i>PSD Mean Value (µm)</i>
<b>Sample 1</b>	3	-	-	-	IPA	99.1
<b>Sample 2</b>	8	-	-	-	IPA	80.3
<b>Sample 3</b>	18	-	-	-	IPA	35.0
<b>Sample 4</b>	8	1	-	-	IPA	118.0
<b>Sample 5</b>	8	42	-	-270	Triton x100	47.4
<b>Sample 6</b>	8	42	66	-270	Triton x100	31.7

Each of the three powder samples (XB-1, FC-01 and P7) were used to prepare a total of six samples allowing for a low (1150 °C) and high (1400 °C) temperature sample to be prepared for each powder. Separately, one gram of XB-1, FC-01 and P7 was combined with two grams of 727XW cullet to create three pairs of samples (two of each powder). The cullet was rolled to achieve a mean PSD of 25 µm prior to mixing with the powder sample. Each mixed sample was placed in a 100 % platinum thimble and heated to the prescribed temperature for a duration of 24 or 72 h (Table VI).

Table VI. Xenotime XRD Powder Samples Firing Schedule

<i>Sample</i>	<i>Schedule</i>	<i>Schedule</i>
<b>XB-1</b>	72 h @ 1150 °C	24 h @ 1400 °C
<b>FC-01</b>	72 h @ 1150 °C	24 h @ 1400 °C
<b>P7</b>	72 h @ 1150 °C	24 h @ 1400 °C

Samples were removed from the furnace at the specified time and allowed to cool in ambient conditions. This was done in an attempt to quench the melt and minimize any possibility for crystallization during cooling. Each of the samples were removed from the platinum thimbles once they had reached ambient temperatures and sealed in a plastic sample bag for transport to the XRD facility, (Figure 25).

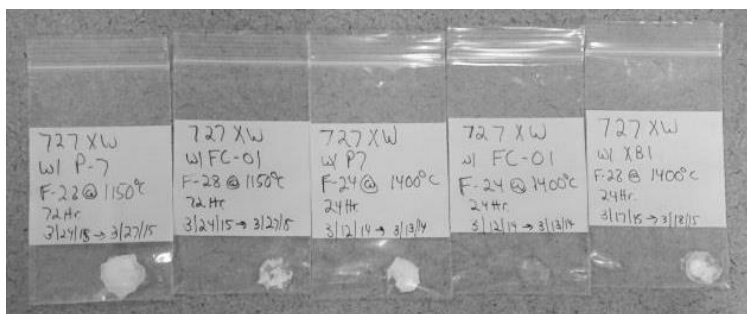


**Figure 25. Finished samples for XRD characterization.**

Samples were pulverized for room temperature powder XRD using a Rocklab Standard Ring Mill batch pulverizer. Each sample was individually placed into the tungsten carbide head, inserted into the pulverizer and run for a duration of 30 seconds. The sample was removed from the head and placed in the sample holder using a glass slide to pack and level the sample. Samples were then inserted into the sample tray for analysis.

A Bruker D4 Endeavor XRD process unit was utilized to perform crystalline phase identification using a Cu tube source at 40kV and 40 mA utilizing a LYNXEYE strip detector. Scans were made from 5-80° two-theta. The Bruker D4 Endeavor utilizes a queue with auto load allowing the samples to be placed in the queue to be automatically scanned during the night.

#### **D. HTXRD**

One additional sample was prepared for high-temperature X-ray diffraction (HTXRD) and testing was completed at Alfred University. Measurements were performed using a Siemens diffractometer with a custom high temperature furnace using

a cobalt radiation source. The powder sample was prepared from the same XB-1 powder used for the room temperature measurements. This powder sample was prepared to a mean PSD of 25  $\mu\text{m}$ . Similarly, the 727XW glass cullet powder used in the room temperature XRD scans was utilized in the high temperature experiments.

As was done for the room temperature scans, the xenotime (XB-1) powder was mixed with the glass powder to disperse the xenotime (XB-1) amongst the cullet. Differing from the samples prepared for the room temperature scans where one gram of xenotime powder was mixed with 2 grams of cullet, a 50/50 mix was prepared for the high temperature scan.

On a calibrated bench scale, a sample tray was zeroed and 0.2506 grams of 727XW glass powder was added to 0.2514 grams of the XB-1 powder. The combined sample was placed in a mortar and pestle, IPA was added and the sample was mixed for 1 min. The sample was allowed to thicken as the IPA evaporated until the mixture was viscous enough to be placed on the sample tray without risking run-off. This was especially important, as it was desired to prepare a sample thick enough to minimize any potential Al in the corundum sample tray diffusing into the sample and becoming a source of error in the diffraction patterns.

A sample tray was prepared for the experiment, Figure 26. A 15 mm wide x 1 mm thick strip of corundum was cut to approximately 75 mm length. This strip was placed on the lab bench and cement was applied to the surface in several positions along the length. A quartz strip approximately 0.5" shorter than the corundum and of the same width was then affixed to the top surface of the corundum, affixing it to the corundum. The corundum strip was cut to a length suitable to insert it into the sample holder as it is supported from either end by two posts when inserted into the sample holder on the diffractometer. The quartz strip was used to reinforce the corundum strip against creep while at high temperature though its length was insufficient to span the entire length of the sample holder. To complete the assembly, a 0.75" x 0.75" x 0.0625" thick corundum strip was cemented to the quartz at the mid-point of the quartz strip.

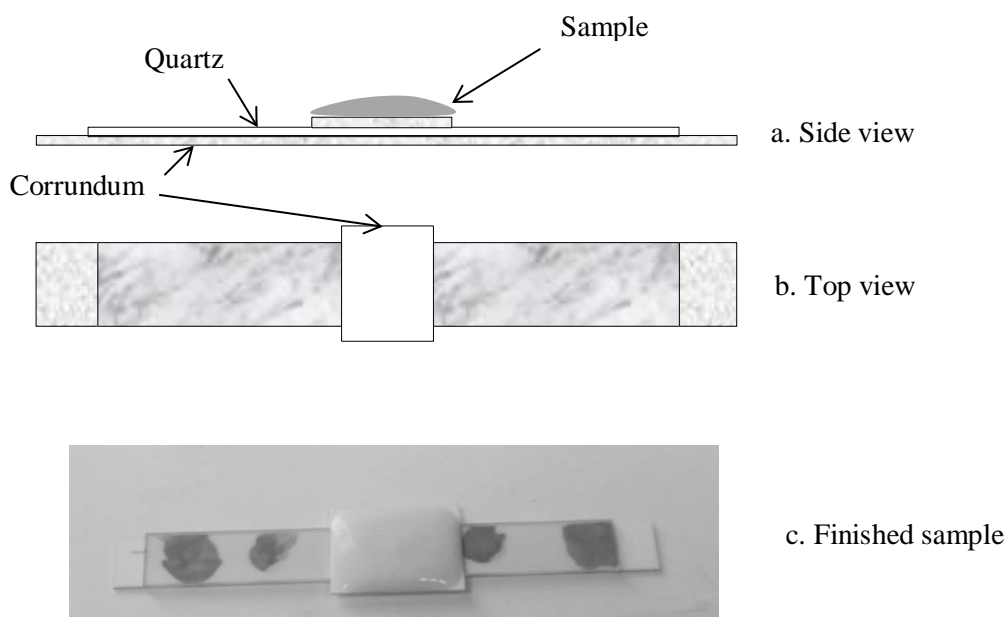


**Figure 26. Sample prepared for HTXRD measurements.**

The prepared sample was placed in the diffraction furnace, supporting it on either end by two pins (Figure 27) positioned inside the refractory insulation. No purging atmosphere was utilized during this experiment and the sample was tested in air as was done with the previous room temperature samples. The furnace was heated by a resistive heating Pt coil contained within a SALI (Zircar Refractories) refractory insulative chamber to provide a large volume heating effect as opposed to strip heaters found in other designs. During the experiment, the sample position is maintained and rotation of the diffractometer is achieved by dual goniometers. Details for this equipment are well documented by Misture.<sup>18</sup>

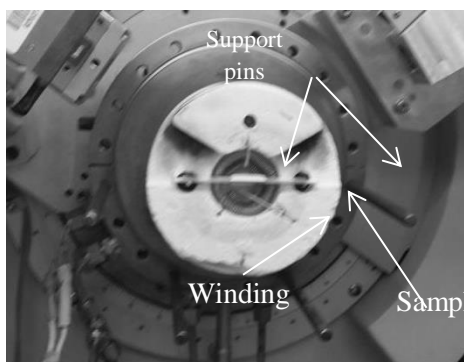


**Figure 27. Slide for HTXRD shown in holder.**

With the sample inserted on the support pins, the chamber was sealed and the unit was set to 40 kV and 30 milliamps. The furnace controller was turned on and set to 25 °C. Calibration of the sample was achieved using a xenotime peak at 19.55° two-theta. A calibration scan was made from 10-60° two-theta. The resulting diffraction pattern was found to be skewed to the right and the stage was adjusted down until the peaks were centered. This calibration was necessary as the height of the sample surface is a variable during the preparation stage. This calibration allows the surface to be adjusted to a nominal position calibrating it to the known sample.

The temperature range of interest for the sample was between 900 and 1400 °C. The condition of the high temperature diffractometer was such that only 1350 °C was possible at the time of testing. Considering the significant amorphous phase discovered in the room temperature XRD results conducted on the sample heat treated to 1400 °C (see results section D), it was decided to proceed and only scan up to 1350 °C. A schedule was programmed into the controller (Figure 28) to scan the sample at 50 °C intervals starting at 900 °C with the final scan at 1350 °C. Initial heating from room temperature was performed at 10 °C/min to 900 °C where the first scan was performed. Scan duration was 25 min after which the furnace was programmed to increase temperature at a ramp rate of 5 °C/min, stopping every 50 °C to perform a scan. Once the scan at 1350 °C was completed, the system was allowed to cool naturally back to ambient conditions. Scans were also performed before and after high temperature scans at both the beginning and end of the sequence.

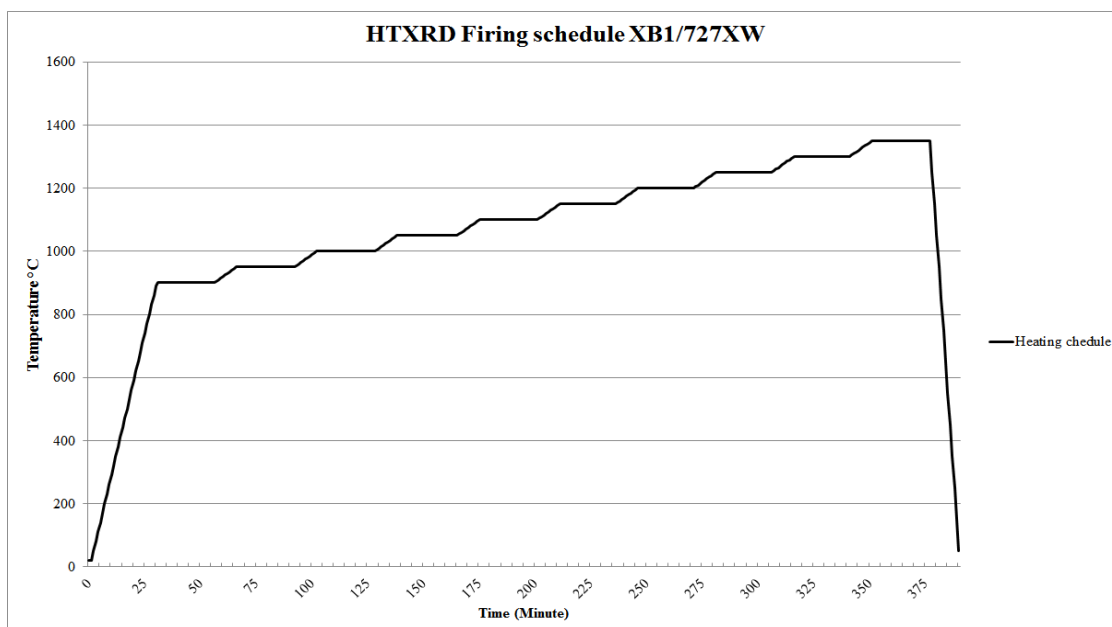


**Figure 28. HTXRD firing schedule.**

It was found in the data and will be discussed later, that there was a peak shift during the scanning process. It is believed that a vertical displacement in the surface during heating caused this shift. It is not known at this time the exact cause of this shift but it is likely a component in the sample mixture melted at elevated temperature causing the surface to slump (Figure 29).

A final room temperature XRD scan of the sample was made following the high temperature treatment on a Bruker D8 advanced XRD with copper radiation and was used to make the initial phase identifications. It is noted that the copper radiation source shifted the peak position from the HTXRD sample data which utilized cobalt and this is accounted for in the data in the results section for HTXRD.

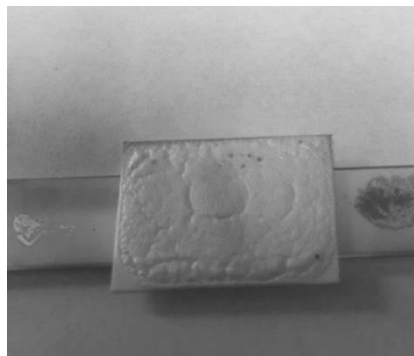


Figure 29. HTXRD sample following scanning.

### E. Sessile Drop

Within the glass industry and specific to mechanisms of refractory corrosion, surface tension is often referred to as a key element in the understanding of the rates of reaction and the life limiting reactions at glass/refractory interfaces. Most commonly, this effect is discussed when examining the “metal line” or the interface where the glass bath, atmosphere and refractory come into contact with one another. This triple point is often the source of life limiting behavior for any glass melting furnace. The continual movement of the surface in this area is driven by molecules moving inwards at a rate faster than those moving outwards. This creates micro-convective currents, which enable the transport of the products of reaction away from the refractory surface and driving the rate of corrosion upward.

Several techniques are available for the surface tension measurement of high temperature liquids: maximum bubble ring, ring, dipping cylinder, drop weight, pin, fiber elongation, capillary flow, pendant drop and sessile drop.<sup>19</sup> The sessile drop and pendant drop methods have emerged as the most practical for glass melts. Despite the simplicity of these techniques, there remain doubts whenever high accuracy and consistency are required.

Historically, the Bashforth and Adams or the Dorsey method were used and were based on identifying and measuring selected points on the drop to find the surface tension of glass melts. Both of these methods are based on numerical solutions of the differential equations which describe the balance of capillary and hydrostatic forces.<sup>20</sup> The tables developed in these methods were limited to drops of a certain size and shape range

placing constraints on their application. A serious source of error results in the method of data acquisition. The surface of the drop is reduced to a few select measurements at prescribed critical points so as to be compatible with the use of such tables. As such the description of the surface of the drop may be inaccurately described. In the case of measuring the interface at the triple point, accurately determining its position is challenging.

Digitized imaging and best fit technologies became available in the early 1980's and greatly improved the capabilities to accurately represent the surface shape. This technology enabled computation of many edge points rather than a few thereby enabling more accurate surface tension measurements. Rottenberg<sup>21</sup> suggests a method of calculation describing the pressure difference across a curved interface as described by the classic Laplace equation:

$$\gamma \left( \frac{1}{R_1} + \frac{1}{R_2} \right) = \Delta P \quad (2)$$

where  $\gamma$  is the interfacial tension,  $R_1$  and  $R_2$  represent the two principle radii of curvature and  $\Delta P$  is the pressure difference across the interface. With gravity being the only external force:

$$\Delta P = \Delta P_o + (\Delta\rho)gz \quad (3)$$

where  $\Delta P_o$  being the pressure difference at a select data plane and  $\Delta\rho$  is the difference in the densities of the two bulk phases (approximated to equal  $\rho$  (liquid) here for the case of a liquid gas interface),  $g$  is the gravitational acceleration and  $z$  is the vertical height as measured from the datum plane. Then with the origin placed at the apex, the  $x$  axis tangent to the curved interface and normal to the axis of symmetry as defined by the coordinate system in Figure 30:

$$\gamma \left( \frac{1}{R_1} + \frac{\sin\theta}{X} \right) = \frac{2\gamma}{R_o} + (\Delta\rho)gz \quad (4)$$

$R_1$  turns within the plane of the diagram,  $R_2$  is equal to  $x/\sin\theta$  and rotates in a plane perpendicular to the diagram,  $R_o$  is the radius of curvature at the origin of the  $x$ - $z$  coordinate system such that  $R_1=R_2=R_o$  at the origin.  $\theta$  is the turning angle measured between the tangent at the interface at point  $(x,z)$ .<sup>21,22</sup>

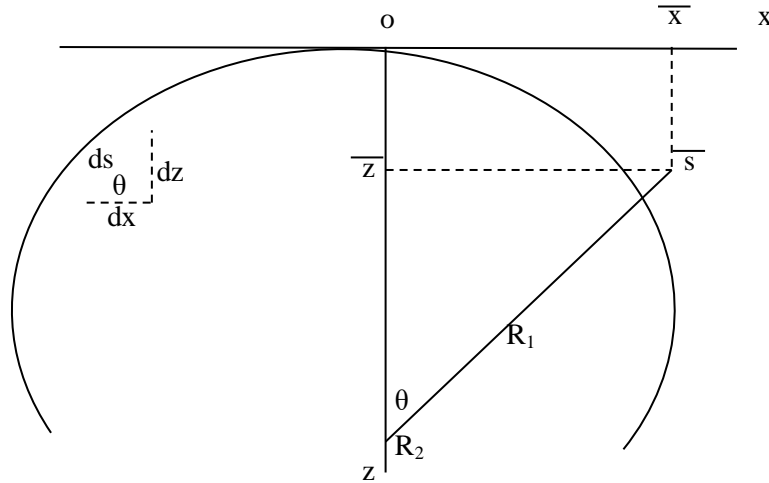


**Figure 30. Definition of coordinate system used in digitized software solver<sup>21</sup>.**

The measurements performed here utilized a digitized analyzer designed by Dr. Nicolas Leblond which is based on these measurements and calculation methods. The methods employed in these measurements are acknowledged to be highly subjective. User observation and input is required and a high level of variation was observed in the measurements. To improve the accuracy of the measurements it would be necessary to modify the arrangements of the test unit and employ a non-wetting substrate such as graphite to measure the drop shape. Though measurements of mass to 1/1000 g were taken before and after runs for each sample, no detectable change in mass was observed and the capability of the outlining software was insufficient to accurately calculate changes in volume. The primary function of this work was to identify and understand the phase developments between the 727XW glass composition and xenotime refractory. These measurements are made as a supplement to additional characterization work and to

improve understanding between this glass/refractory combination and compare to more well-known commercially available products.

Xenotime substrate samples were prepared from the original XB-1 material. A total of 20 pieces were cut to 25mm x 25mm x 6mm using an MK wet tile saw, model MK770EXP. The sample coupons were then hand ground with a Buhler Ecomet 300 grinding wheel. Samples were then ultrasonically washed for 30 min in a Branson 5510 cleaner using an Alconox/DI water cleaning solution. The supply of 727XW glass was limited to a small quantity of already crushed glass and several irregular sheets with lengths of no more than 8 inches and a thickness of 4 mm. Corning Incorporated's sessile drop unit requires cylindrical glass samples between 9mm and 12 mm in height and a diameter of 12 mm or less. To accommodate this, the irregular sheets were cleaned, stacked on one another and inserted into a Carbolite EWF1200 kiln to fuse the pieces together. These sample sheets were raw formed sheet, not chemically strengthened. The final fused sheet was then used to core drill glass cylinders of the appropriate height as specified by the test procedure. A firing schedule was developed to achieve a full fuse between the three sheets. This firing schedule is detailed in Table VII and the firing data is plotted against the schedule in Figure 31. The firing schedule was developed based on strain and anneal temperatures of 639 °C of 586 °C respectively.

**Table VII. Firing Schedule for Sheet Fusing**

<i>Rate (°C/h)</i>	<i>Target temp. (°C)</i>	<i>Hold time (min)</i>	<i>Duration (h)</i>	<i>Purpose</i>
150	450	15	3 hr.	Thermal shock
260	600	NA	2.5 hr.	Bubble squeeze
38	700	30	3 hr.	Push air out
NA	880	10	NA	Full fuse
NA	650	120	2 hr	Rapid cool
10	Room temp.	NA	15 hr.	Anneal

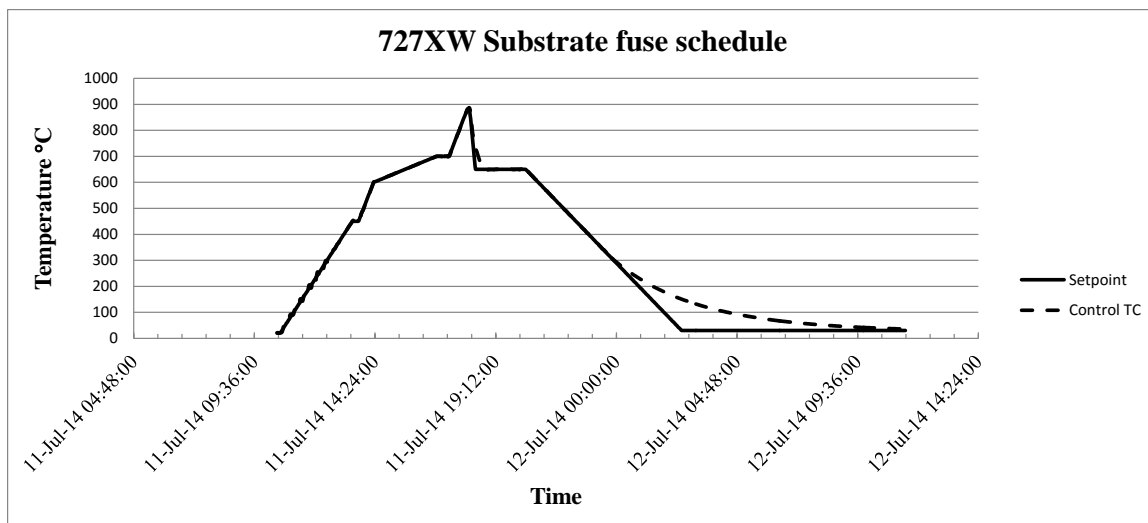


**Figure 31. Firing schedule set-point plotted with the actual control temperature for the glass sheet fusing procedure.**

The fused, annealed sheet was then used to produce core drill samples for use in the sessile drop experiments, (Figure 32). It was found during the first attempt that at the temperatures of interest, the glass overwhelmed the substrate. The glass cylinder diameter would need to be decreased in order to successfully perform the tests. Subsequently, a 9 mm diameter core drill was procured to enable fabrication of this smaller diameter. Additional glass cylinder samples were then core drilled with the 9mm core drill and used for the sessile drop tests.



**Figure 32. Core drilled, fused sheet.**

A Thermolyne 59300 tube furnace (Figure 33) was utilized to perform these experiments. The unit was an existing piece of equipment in the Corning AR laboratories under the direction of Dr. Nicolas LeBlond. The furnace utilizes a fused silica tube for sample containment with a water cooled seal on the far end of the tube.

During the execution of sample four, the fused silica tube fractured and terminated the experiment. Inspection of the tube revealed condensate on the surface and crystallization of the fused silica tube in the region of the sample. It is believed volatilization from the glass allowed glass species to contact the tube and subsequent devitrification of the fused silica caused it to fail during heat-up.



**Figure 33. Thermolyne 59300 tube furnace (a.) and data collection server (b.) used to perform the sessile drop tests in the Corning AR laboratories.**

This incident incited a level of doubt with respect to the accuracy of the ultimate results of this experimentation method. It became obvious that there were significant levels of volatilization from the glass taking place in the chamber on heating of the sample which would result in variations in density not accounted for in the sample thereby creating inaccuracy in results. Additionally, the surface chemistry of the glass may be altered causing false results of the interfacial energies with the substrate. With a lack of appropriate alternatives, this issue was noted and will be discussed in the results. At best, calculated values derived from these experiments provide a trend amongst the samples.

The broken vitreous silica tube was replaced with an alumina tube for subsequent experiments. The water-cooled seal has capabilities for purging the sample chamber with Ar or other gas but was not utilized for these experiments. The working end of the tube, the end where sample insertion took place, was controlled by the placement of a fused silica plate over the open end but had no provisions at the time for sealing.

Images were captured through a digital camera that was positioned at the working end of the tube and transmitted to the server. Imaging was captured and controlled through a National Instruments Vision Builder software user interface, (Figure 34). The images were captured on the server and later transferred to a laptop for post-processing.

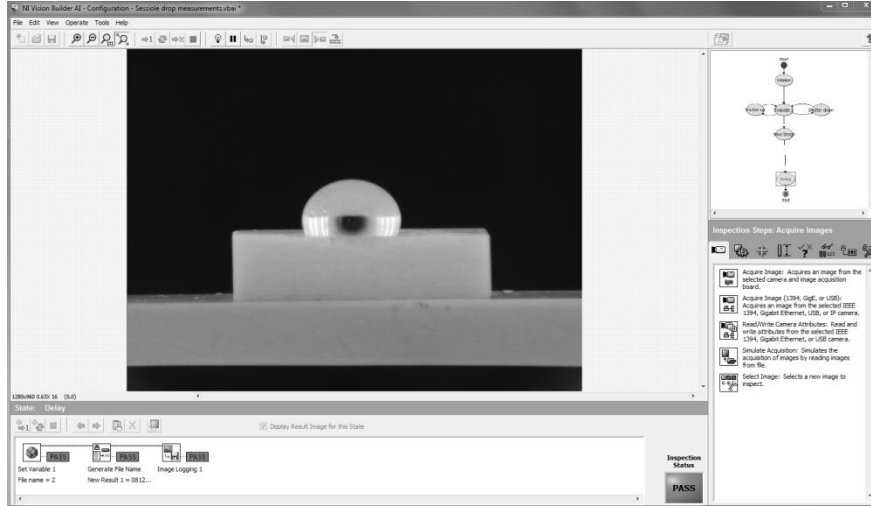


Figure 34. NI Vision builder user interface used to capture images and control the imaging system.

In all, seven sessile drop experiments were carried out on the xenotime substrate with 727XW glass and details as provided in Table VIII. For each experiment, the 727XW glass cylinder was centered on the xenotime substrate. The substrate was then placed on top of a zirconia sample support and inserted into the tube furnace to an insertion depth of 22". The zirconia support tray was sized for the system and is the point of contact between the sample and the furnace tube to set its elevation. A Vycor push rod was used to position the sample to the exact distance as indicated by a stop on the Vycor rod.

Table VIII. Seven Samples run During the Sessile Drop Tests

	<i>Sample 1</i>	<i>Sample 2</i>	<i>Sample 3</i>	<i>Sample 4</i>	<i>Sample 5</i>	<i>Sample 6</i>	<i>Sample 7</i>
<b>Target Temp. (°C)</b>	1250	1200	1250	1150	1150	1100	1050
<b>Diameter (mm)</b>	11	9	9	Tube Failure	9	9	9

The furnace was prepared for operation by turning on the water flow to the seal cap on the back end of the tube. A type S thermocouple was inserted and positioned on the bottom of the zircon sample tray, Figure 35. This thermocouple would be used later to fine tune the temperature of the sample within the furnace.

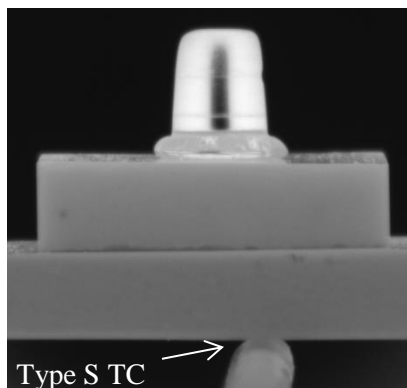


**Figure 35. Sessile drop sample arrangement during testing.**

A fused silica cover plate was installed over the open end of the tube where samples were inserted and held in position through a clamp and stand arrangement. The camera was positioned to predetermined positions on the floor to allow for accurate, repeated positioning between samples, setting the camera distance to the sample. The controller was then set to ramp the furnace to a set-point 30 °C below the target temperature at a ramp rate of 10 °C/min. At 700 °C the capture was initiated at a capture rate of one image every 10 min. The image quality was manually adjusted at this temperature to focus and correct the brightness of the image. Using the live image, a final adjustment of the level of the substrate was made by rotating the tube so as to level the substrate with a leveling line on the NI Vision Builder software package. The NI Vision builder software also utilized fine tune adjustments beyond the manual adjustments set by the user which were re-evaluated by the software every 10 min following the image capture. The system was allowed to run for a duration of 18 h at which time the capture was halted and the controller on the furnace set to ramp down to room temperature.

A second set of samples were prepared to enable a baseline comparison of 727XW and xenotime to a commercially available glass composition and two additional

commercially available refractories using the sessile drop method. A sample of soda lime silicate glass sample was acquired from World Kitchen and prepared similarly as detailed above for the 727XW glass to be utilized in the sessile drop apparatus.

Refractory samples were obtained of dense alumina (A1148) and fused zirconia (SCIMOS CZ). Both of these materials are commercially available glass contact materials currently utilized throughout the glass industry. The SCIMOS CZ sample was of particular interest for its wetting properties as it is well recognized for its excellent corrosion resistance properties when in contact with glass melts. Both the SCIMOS CZ and A1148 substrates were prepared in the same manner as the xenotime detailed earlier. Sessile drop tests were performed on these three refractories with both the soda lime silicate glass and the 727XW composition for a total of six tests (Table IX) at 950 °C.

**Table IX. Isothermal Sessile Drop Tests at 950 °C**

	<i>A1148</i>	<i>SCIMOS CZ</i>	<i>Xenotime</i>
<b>Soda Lime Glass</b>	<b>x</b>	<b>x</b>	<b>x</b>
<b>727XW</b>	<b>x</b>	<b>x</b>	<b>x</b>
<b>Glass</b>	<b>Substrate</b>		

There is a significant difference between the softening temperatures of the two glass compositions which required these tests to be performed at a relatively low temperature of 950 °C. It was found during the first sample attempted at 1100 °C that the soda lime silicate composition resulted in nearly full wetting on the xenotime and A1148 sample coupons. The test temperature was revised down to 950 °C in an effort to alleviate this condition. This was a concern as some uncertainty exists as to whether the 18 h time was sufficient for the 727XW samples to reach equilibrium due to their significantly higher viscosity at these lower temperatures. Throughout the testing it was noted that the 727XW samples required significantly longer time to slump than did the SLS glass samples. The SLS glass samples began to slump rapidly above 700 °C. The softening temperature of this particular composition is reported as 723 °C.

## **F. EPMA**

Electron probe microanalysis (EPMA) was utilized to aid in the characterization of phase developments in the 727XW/ xenotime reaction zone. Ideally only the x-rays

produced in the interaction volume on the EDS will reach the detector. However, this does not provide realistic data of the sample chemistry on this scale. As shown earlier, the size of the crystals structures shown in previous micrographs are significantly smaller than the SEM beam interaction volume and it is likely x-rays of species from other areas such as the glassy matrix are produced and are recorded on the detector as well. Utilization of the EPMA has the potential to significantly reduce the probe diameter. It also employs a WDS detector greatly improving the quantitative identification of elements in a small area. WDS is preferred when the highest energy resolution is needed and is essential in phase analysis studies where spectral changes may be subtle. Quantitatively characterizing the crystallites found in the glass and phases at the reaction interface without being convoluted by species in areas directly adjacent to it was the goal of utilizing this method. The advantage of employing EPMA is achieved by measuring the line intensities for each element in the sample and for the same elements in calibration standards of known composition allowing accurate determination of concentrations of the elements in the sampled area.

The gradient boat sample prepared and used during the SEM analysis which was subjected to a 72 h duration firing was chosen to be used in EPMA analysis. Qualitatively, this sample provided some of the more pronounced crystal developments of the three samples used in the SEM analysis.

The three sample pieces were removed from the epoxy mount previously used in the SEM analysis. These pieces were then re-polished and carbon coated in preparation for use in the EPMA. Only the low and high temperature pieces were utilized for EPMA as the areas of interest were in identification of phases. This corresponds to the upper and lower pieces from the original epoxy mount, Figure 16. The middle piece was not utilized during the EPMA procedure.

Both samples were characterized on a JEOL 8900 Superprobe utilizing five spectrometers. An accelerating potential of 15 kV was set with a 3.2 nA beam. The beam diameter was adjusted to 10  $\mu\text{m}$ . JEOL ZAF software was utilized for correction. Scan durations were set to 5 seconds on background and 10 seconds on peak. A large diameter spot was set-up to minimize volatilization of Na.

The five spectrometers were set-up to scan for P, Si, Al, Y, Sr, K, Ca, Na and Mg as shown in Table X.

**Table X. Nine Species Scanned for in the Samples on the JEOL Superprobe**

	<i>Spectrometer</i>				
	<b>1</b>	<b>2</b>	<b>3</b>	<b>4</b>	<b>5</b>
<b>Element</b>	P	Al	Y	K	Na
<b>Element</b>	Si		Sr	Ca	Mg

Three standards were used during the experiment and scanned a total of four times to calibrate and ensure accuracy. The elements and their corresponding standard are recorded in Table XI.

**Table XI. Nine Species Matched to Three Standards**

<i>Standard</i>	<i>Element</i>								
	<b>P</b>	<b>Y</b>	<b>Al</b>	<b>K</b>	<b>Na</b>	<b>Si</b>	<b>Mg</b>	<b>Ca</b>	<b>Sr</b>
<b>YPO<sub>4</sub></b>	X	X							
<b>Kakanui Hornblend</b>			X	X	X	X	X	X	
<b>716 ECI</b>									X

The first scan was performed on the low temperature sample corresponding to a temperature of 1150 °C. A point was selected in the center of the refractory to verify the refractory composition and to verify the accuracy of the set-up. Additional scans were conducted at the reaction interface focusing on identification of the species in those regions. A suitable crystal structure was identified in the glassy region which was large enough so as to minimize interaction with the surrounding region and scanned.

The high temperature sample was examined for the purpose of determining the composition of the cloudy regions and dendritic needles formed in the glass. As mentioned previously, locating these regions proved challenging. Ultimately a suitable region was identified however, due to the small size of features it was determined they were in fact too small so as to provide believable results.

## G. DSC-TGA

The possible existence of a hydrate phase as revealed by XRD measurements prompted an effort to better understand the expulsion of residual water during heating and identify phase changes taking place in the samples at elevated temperatures. Differential scanning calorimetry (DSC) coupled with thermogravimetric analysis (TGA) was utilized to investigate thermal and mass changes. DSC provides a method to analyze phase changes in a sample through measuring the difference in energy required to heat a sample with respect a reference. As the sample goes through transformations, the requirement for more or less heat to be transferred to the sample in order for it to maintain the same temperature as the reference is measured. TGA data was collected with the DSC data to reveal mass changes as a function of temperature.

A NETZSCH STA 449 F1 Jupiter thermal analyzer with auto-sampler was utilized for this work in the Corning Inc. FR laboratories. The unit is chilled with a Julabo F25 MA chiller to protect the equipment. Three samples were heated up to 1400 °C at a heating rate of 10 °C min<sup>-1</sup> in air. The unit was heated with a SiC heating element.

Xenotime powder processed for the powder XRD samples was utilized in these experiments with crushed 727 XW cullet. A total of three samples were prepared for this; 1) 727 XW glass, 2) xenotime (XB-1) and 3) a 1:1 mixture of 727 XW and xenotime powders. A Metler Toledo MX5 microbalance laboratory scale was used to weigh each sample. An alumina thimble was zeroed and 20 mg of sample weighed out and the top of the thimble was covered with a perforated top for venting. Samples were loaded into the auto-sampler and the heating sequence was programmed into the unit.

# RESULTS

## A. SEM/EDS

Using the SEM, samples were individually scanned at each of the prescribed temperatures to identify features and interesting anomalies relevant to the identification of phase developments. Micrographs and point spectrum data were collected from these samples for post processing. A sampling of micrographs were consolidated (Figure 36), in order to aid in the identification of any patterns within the samples. The development of reaction layers at the glass-refractory interface is evident in most of the micrographs but is particularly evident in the samples treated at 1050 °C.

In these micrographs, the xenotime base refractory has been positioned at the bottom and the glassy region at the top. A light grey interface directly adjacent to the glass is observable along the refractory boundary across most of this region. Moving away from the glass, a darker region is seen within the refractory before transitioning to a lighter shade of grey which is the unaltered base xenotime refractory. At slightly higher temperatures (1200-1250 °C), crystals are observed in the glassy region. As the temperature increases to the right towards 1450 °C, a more sharply defined boundary between the refractory and glass is observed. Through the course of this study, these boundary layers and crystals within the glassy region were the focus of characterization efforts.

Point spectra were obtained for each sample focusing on readily recognizable features such as the base xenotime refractory, the reaction layers and crystal development in the glassy matrix. Within each sample, the base refractory was identified as the lightest shade, furthest from the glass. Phases within the reaction layer vary in shades of grey between the base refractory and glass. The image in Figure 37 was taken from the sample subjected to 1250 °C for a period of 24 h.

The xenotime base refractory is located at the top of this image and is characterized by spectrum 119 and data supports the existence of species only associated with the base refractory,  $YPO_4$ . Examination of the image reveals distinct phase developments at the interface layer. These phases are represented by spectrum 115, 117

and 118. The region represented by spectrum 115 appears as a distinct layer developed at the interface of the glass and refractory boundary with varying degrees of penetration into the base xenotime. A line has been traced which indicates the limit at which species from the glass composition have diffused into the refractory. There also exist regions within this boundary layer, as represented by spectrums 117 and 118, which appear as dark masses within the boundary layer.

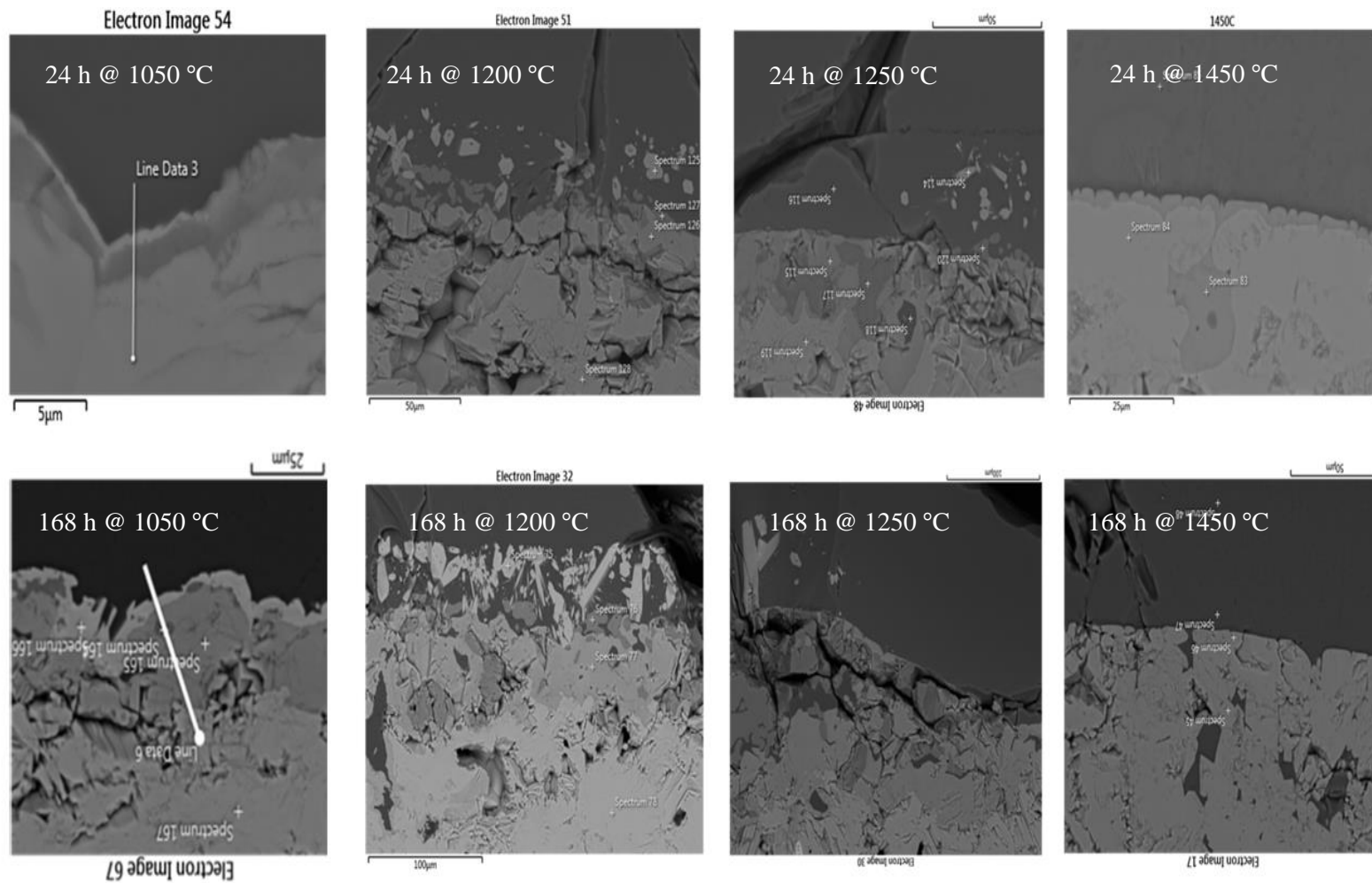


Figure 36. A sampling of micrographs are shown from the time/temperature matrix.

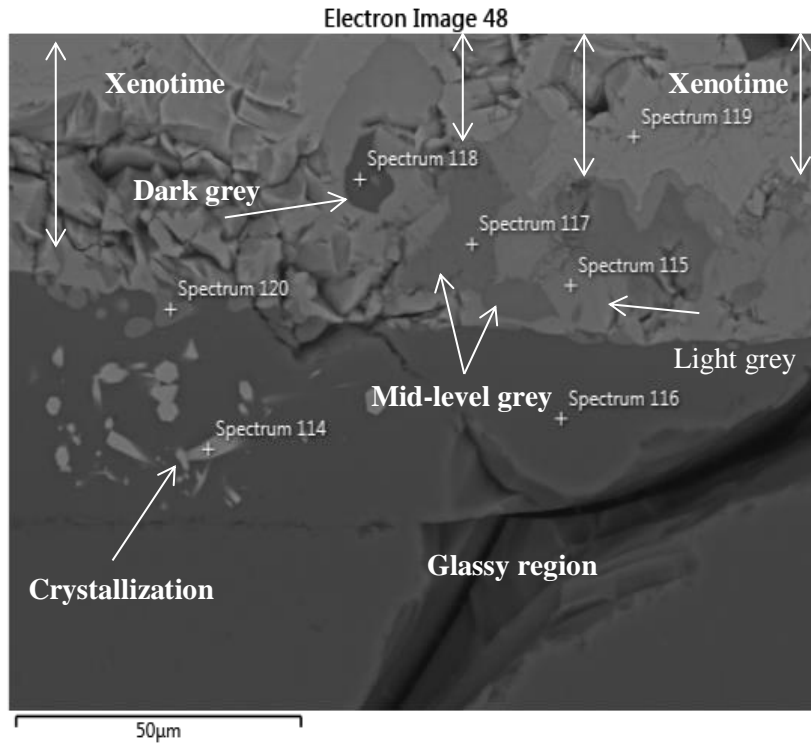


Figure 37. Micrograph displaying reaction layer.

Data from point spectrums 115 and 119, Figure 38, indicate the migration of the alkali and alkaline earth components Na, K and Ca from the glass to the refractory together with a trace concentration of Si.

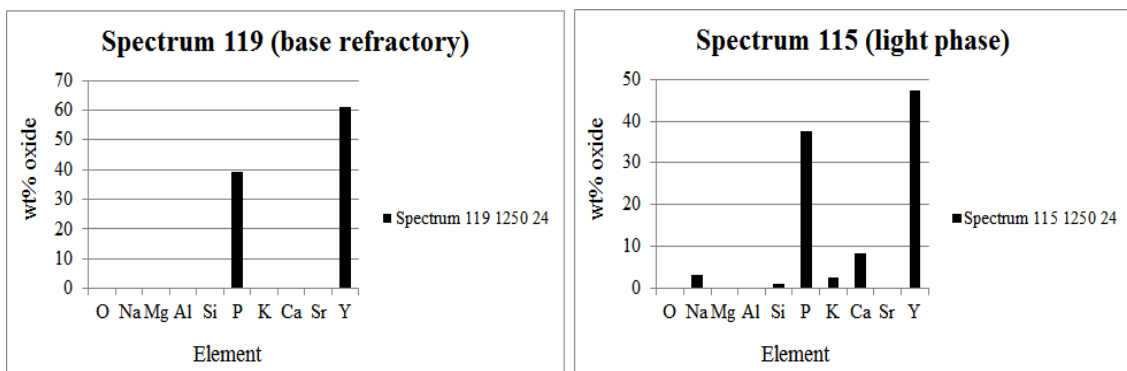


Figure 38. Point spectrum data of base refractory and light phase.

It is assumed that the two regions represented by spectrums 117 and 118 in Figure 39, identify new phase developments within this boundary layer. Spectrum 117 represents a slightly darker region within the boundary layer where Y concentrations have diminished to approximately 15 wt% oxide from 46 wt% oxide in spectrum 115 while Na, Mg, Si, K, Ca and Sr concentrations all have increased. Levels of P in spectrum 117 have remained unchanged at just slightly less than 40 wt% oxide. Spectral data from spectrum 118 indicates a rapid depletion of P while there has been a significant increase in the concentration of Si, Na, Ca and Sr. The concentration of Y becomes further depleted in this dark region. In consideration of this data, it is more likely this dark region is actually glass which has penetrated into the refractory rather than being a new phase development. The concentrations of Y and P are less likely depletion due to migration away from this region and more likely diffusion of these species into the glass.

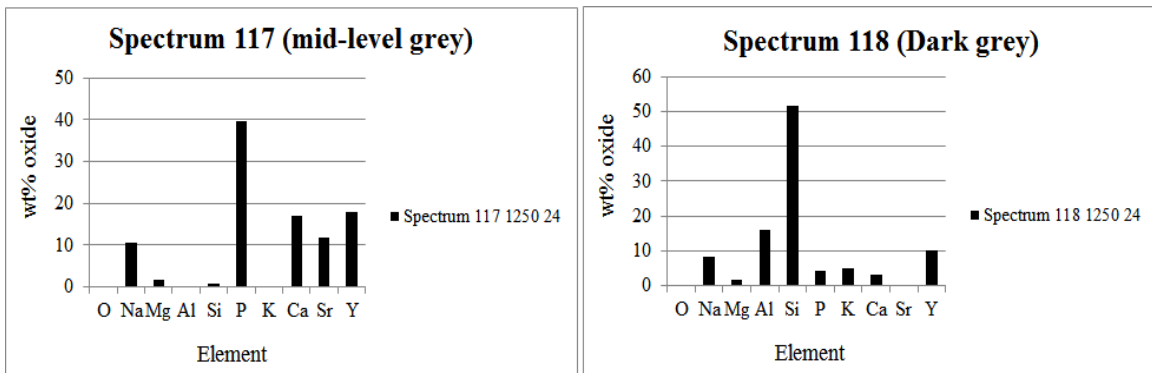
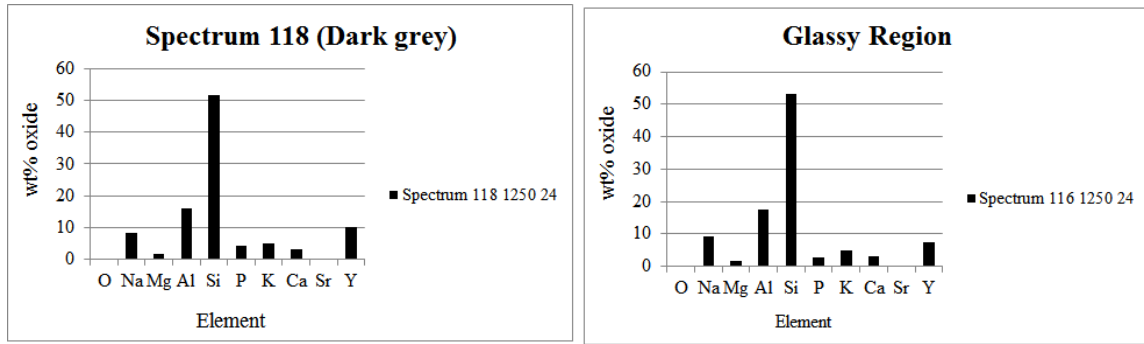


Figure 39. Point spectrum data of mid-level and dark grey phases.

Figure 40 compares this darker region found within the refractory to chemistry data taken from the glassy region outside of the refractory. It is apparent that the compositions of these two areas are very similar and likely the same. This suggests some level of penetration of the glassy phase into a pore or void within the refractory.



**Figure 40. Point spectrum data of dark grey and glassy phases.**

For all samples, the collected spectral data was broken down into individual data collected from the EDS based on relative appearance of each region. The spectral data from each sample was used to create a bar graph indicating the oxide and relative wt% oxide. Potential phases were identified and categorized as base refractory (lightest appearance), light grey, mid-level grey and dark grey. The bar chart for each spectrum point was broken out by category of appearance for each sample as shown by Figure 41 representing the 24 h sample run at 1250 °C. Additionally, regions of interest not clearly belonging in one of these four categories, were set aside for further investigation once a matrix was constructed. These were labeled “ROI”.

Similarities in these classifications were recognized as data obtained from each of the samples were inserted into these categories. Data from each temperature sample and time duration was combined into bar graphs for analysis and comparison. As an example, all spectrum identified as light grey that were run for the 24 h duration were combined into one bar graph as were those for the xenotime, mid-level grey and dark grey phases. The resulting plots revealed obvious similar phase developments among the samples of the same time duration at the different temperature assignments, Figure 42.

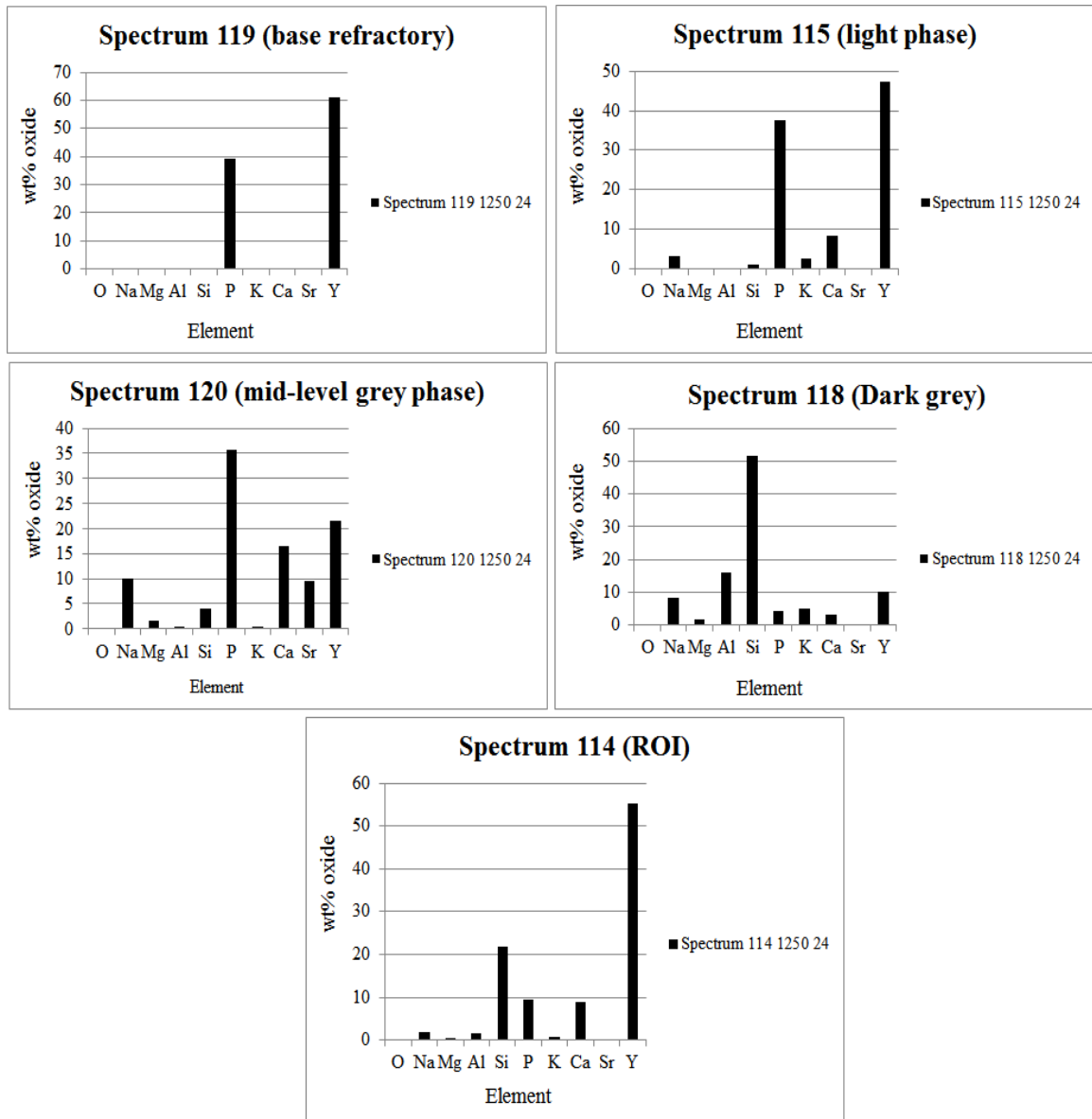


Figure 41. Point spectrum data for the five primary phases.

Data was compiled in the same manner for the 72 h and 168 h samples and laid out in a matrix format together with the 24 h data for comparison and may be found in the Appendix. Relative to the categorization, similarities between the data is observed from one temperature category to another and indicates similar phase developments throughout the samples regardless of time and temperature.

Both the light grey and the mid-level grey phases contain significant levels of P and Y. The light phase containing a higher wt% oxide of Y than the mid-level grey.

Both contain similar wt% oxide of P at approximately 35. Similarly, each contains both alkali and alkaline earth metals diffused from the glass. It is evident that the mid-level phases contain a higher concentration of these species than does the light grey phase.

The raw data collected during the point spectral characterization was converted from weight percent of the oxide to a molar percent through the conversion:

$$m_i = \frac{100 \times w_i \%}{M_i \sum_{j=1}^n \frac{w_j}{M_j}} \quad (5)$$

where  $w_i$  is the weight percent of the oxide,  $m_i$  is the molar percent of the oxide,  $M_i$  is the molar mass of the oxide and  $\sum_{j=1}^n \frac{w_j}{M_j}$  is the sum product of the weight percent of the oxide and atomic weight. This conversion provided a stoichiometric view of the data which was thought to have potential of providing additional clarity in the identification of phases within the reaction layer.

The resulting data was compiled in the same manner as was done for the raw oxide weight percent data resulting in a summary matrix which is compiled from molar data and may also be found in the Appendix. The data resulted in a similar matrix as the raw wt% data, showing clearly the xenotime phase together with the three other phases; light grey, mid-level grey and the glassy phase. It was somewhat easier to consolidate some of the outlying regions of interest identified in the original data when viewed from a molar percent perspective. This resulted in the elimination of the ROI category.

It is not surprising that in the molar percent data, both Y and P are reported at 50 mol% each for the xenotime sample as they are stoichiometrically equivalent in the base refractory. It is also evident that the molar percent of both Y and P remain similar in both the light grey phase and the mid-level grey phase with values ranging between 25 and 35 mol%. With respect to the molar data, these two species appear to behave similarly.

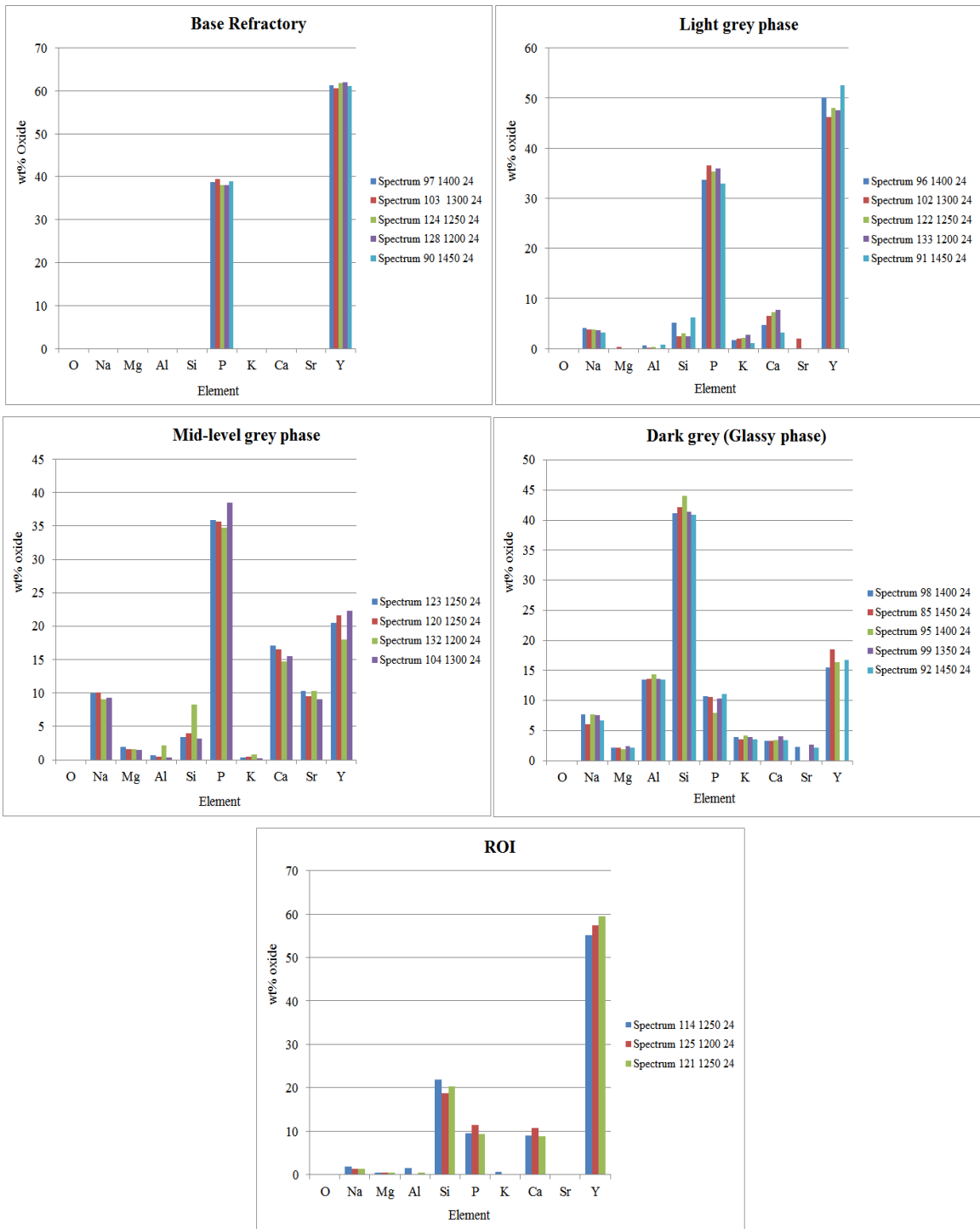
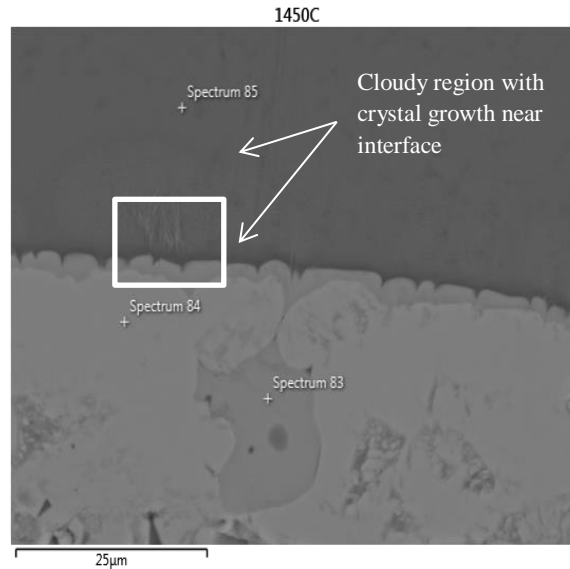


Figure 42. Point spectrum data compiled for all samples run at 24 h.

Several examples of crystal growth were observed during the characterization of the samples. Upon examination of all images, some of the most interesting observations

were made of the samples from the 24 h heating period at elevated temperature. In these samples it was noted that there appears to be development of concentrated areas of phase separation near the glass/refractory interface. Under low magnification, these areas presented themselves as cloudy, sack like features, Figure 43.



**Figure 43. Devitrification near reaction interface.**

The sample exhibited in Figure 43 was taken to higher magnification to allow further examination of crystal development in this region. Upon closer examination, it was revealed that these cloudy regions were in fact distinct regions of what appears to be either phase separation or sub-micron nucleation sites, Figure 44. Additionally, these higher levels of magnification also revealed the formation of distinct crystals which appear to be of dendritic character.

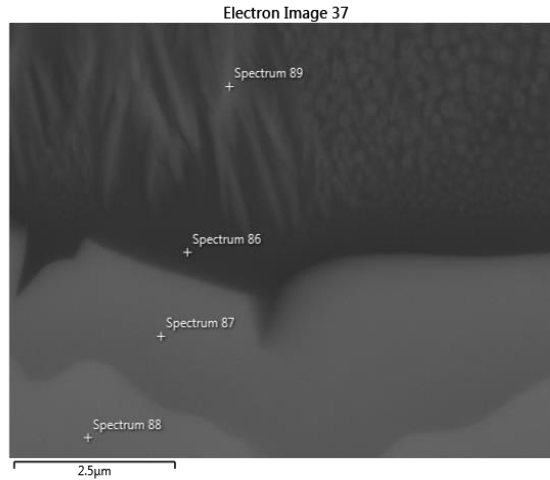
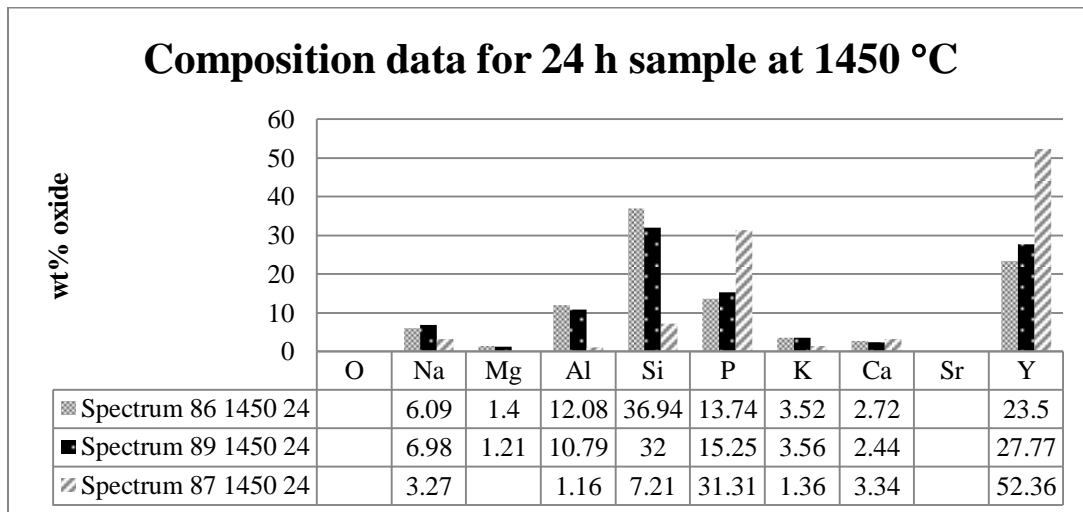


**Figure 44. High magnification of devitrification near interface.**

Oxide weight percentages for spectrums 86, 87 and 89 are tabulated to examine the differences between the regions, Table XII.

**Table XII. Point Spectrum Data from Region of Devitrification**



The species found in spectrum 87 are representative of the light grey phase at the interface boundary consisting of primarily Y and P with some Si and trace oxides detected. Spectrum 88, not tabulated, was revealed to be solely Y and P indicating it was the original base refractory  $YPO_4$ . Point spectrums 86 and 89 appear to be similar in composition however some uncertainty does exist due to the beam interaction volume

which was believed to be approximately 1  $\mu\text{m}$ . The scale shown on Figure 44 of 2.5  $\mu\text{m}$  would indicate potential for overlap with the amorphous region and crystal leaving some level of doubt as to the chemical composition of the new crystal formations. It is not known at this time whether the dissolution of the reaction layer reforms into these dendritic crystals from the glassy region.

Another example of this apparent phase separation and crystallization, similar to those observed in Figure 44, was identified in the sample obtained at 24 h and exposure to 1450  $^{\circ}\text{C}$  and is shown in Figure 45. Again, the apparent phase separation is readily identified and a crystal is observed extending from the refractory boundary.

What is interesting to consider here is the potential of yttrium aluminosilicate systems to exhibit phase separation and crystallization as mentioned earlier in the literature review. It has been suggested that higher levels of Si and lower levels of Y and  $\text{Al}_2\text{O}_3$  will depart from the glass forming region and lead to both phase separation and crystallization for this particular system. The numerous other species greatly complicates the situation here but data may suggest this is a verification of these claims.

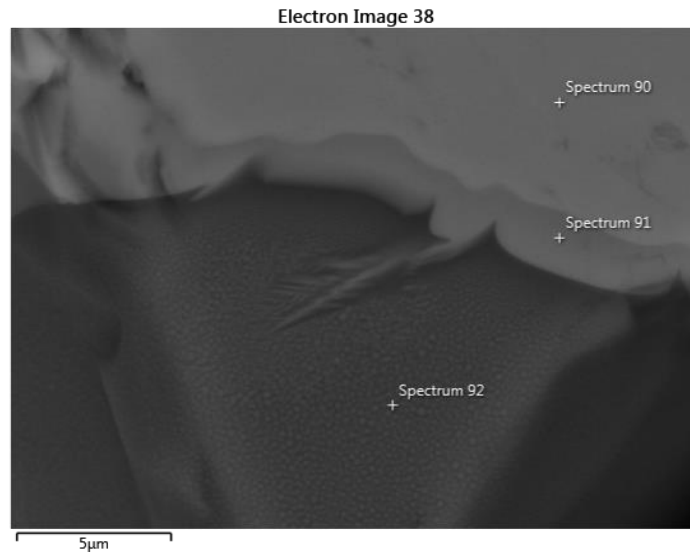
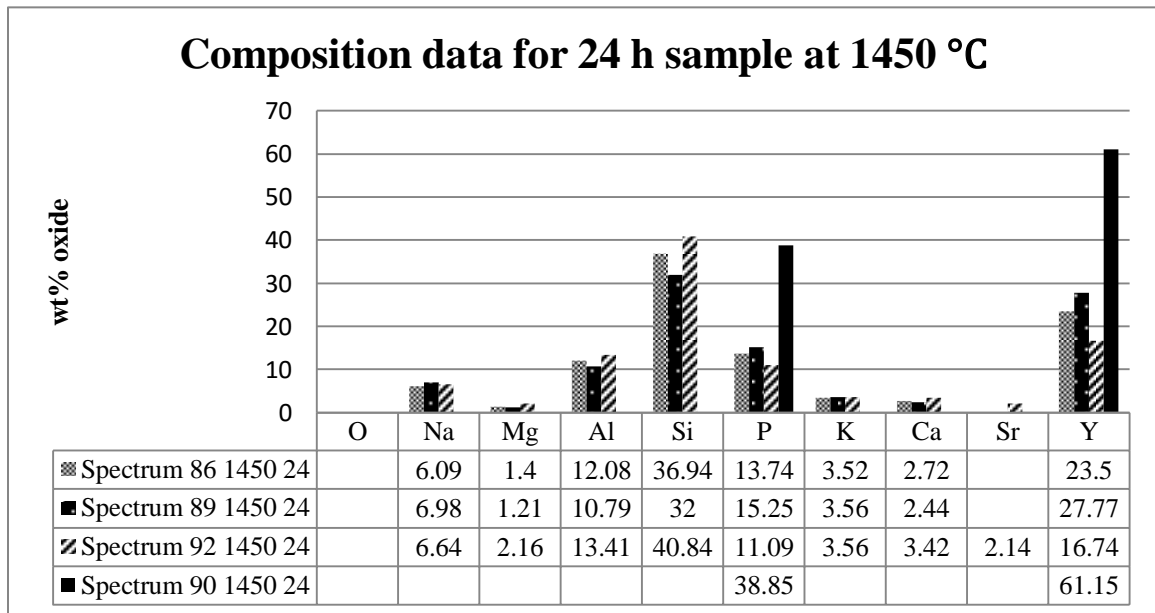


**Figure 45. Devitrification and sack development near interface.**

Table XIII includes composition data from spectrums 86 and 89 and combines it with the point spectral data from the second sample as point spectrum 92. It can be seen in Figure 45 that the region which appears as phase-separated extends greater than 20  $\mu\text{m}$

away from the refractory boundary but is concentrated to a region of triangular shape with its base on the refractory boundary and its top in the glassy region. Extending from the refractory boundary, a crystal was observed growing into the phase separated region. Point spectrum 92 was captured approximately 5  $\mu\text{m}$  away from the refractory boundary layer. This distance from the layer suggests it may lie sufficient distance into the glassy region to retain some of the Si from the glass. Spectrums 86 and 89 lay no more than 2.5  $\mu\text{m}$  from the refractory boundary and are likely to contain more of the refractory elements Y and P as the data shows. Point spectrum 90 is provided as a reference to the base refractory composition.

**Table XIII. Point Spectrum Data from Region of Devitrification**



Substantial work remains to be done in understanding the interaction of rare earth oxides with the aluminosilicate glass family. What has been conducted does not enable a clear guidance as to whether phase separation or possibly nucleation may be taking place in these regions. In his work, White references a glass forming region for rare earth oxides in an aluminosilicate glass composition which contains a substantial glass forming region.<sup>23</sup> It is noted that outside of these glass forming regions, the compositions do not melt completely or form two immiscible liquid phases at 1600 °C, Figure 46. Similarly, Shelby had indicated that glasses in the high silica region of glass formation of the

ternary system,  $Y_2O_3$ - $SiO_2$ - $Al_2O_3$ , were clearly phase separated.<sup>17</sup> In his work, TEM was used to characterize  $SiO_2$  rich droplets in a  $Y_2O_3$  and  $Al_2O_3$  rich matrix. Owing to the complexity and quantity of species involved in the reaction interface of the 727XW glass and xenotime, it is impossible at this time to define exactly the process and products taking place in these observations.

The interaction volume of the SEM did not allow for accurate quantification of the chemistry of these formations. Use of thin sections together with the TEM would greatly reduce this interaction volume and increase the capability to understand the composition of these features and their origin. During the course of this work, a TEM was not available for characterization, chemical mapping on the SEM and later, EMPA was utilized to build understanding of the chemical makeup in these regions.

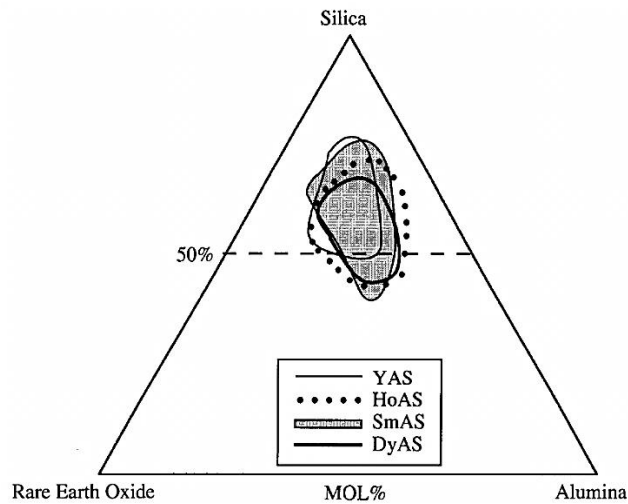


**Figure 46** Phase diagram of REO, alumina and silica.<sup>23</sup>

A sample was selected to further investigate using EDS mapping of the regions of apparent phase separation to aid in the identification of shifts in the chemical distribution. A region was identified within the 24 h sample at 1350 °C which had the appearance of several cloudy regions (Figure 47). Long duration chemical maps of this sample were performed on the SEM/EDS. This imagery provides for a qualitative depiction of the distribution of chemical species in the sample and suggests the dissolution of refractory

and migration of glass constituents to and from these regions of interest during the dissolution process.

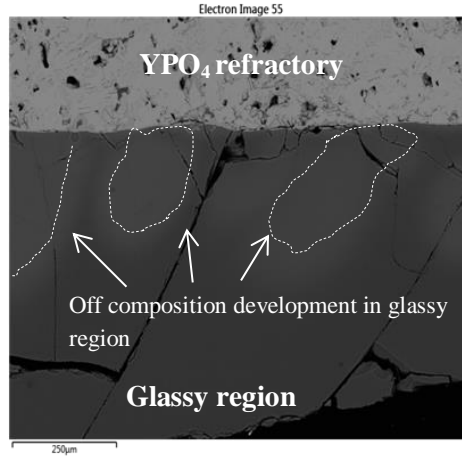


Figure 47. Cloudy regions observed near reaction interface.

With the xenotime composition of YPO<sub>4</sub>, the chemical concentration of both Y and P were examined and indicated the existence of elevated levels of both species in these regions. In Figure 48, the concentration of Y is identified in the cloudy regions. Concentrations of P proved to be less significant and not as easily recognizable on the printed image.

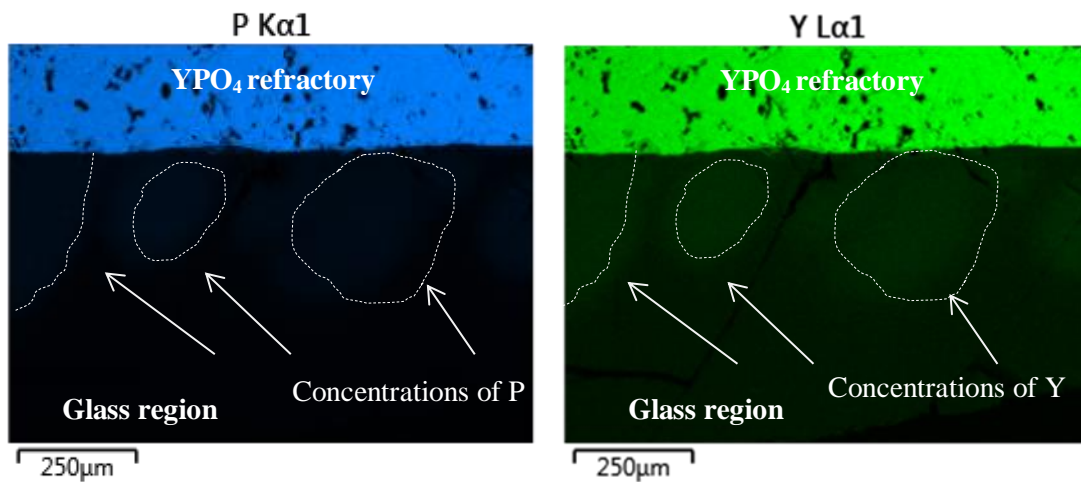


Figure 48. Elemental maps for Y and P.

It was found that species identified within the glass composition exhibited varied patterns of migration. Mg and Ca concentrations increased in these cloudy regions while Si, K and Al migrated away. Figure 49 shows the chemical maps for Mg and Ca and the elevated concentration levels for these elements in the region of interest. There also appears to be a significant concentration of Ca at the glass/refractory boundary.

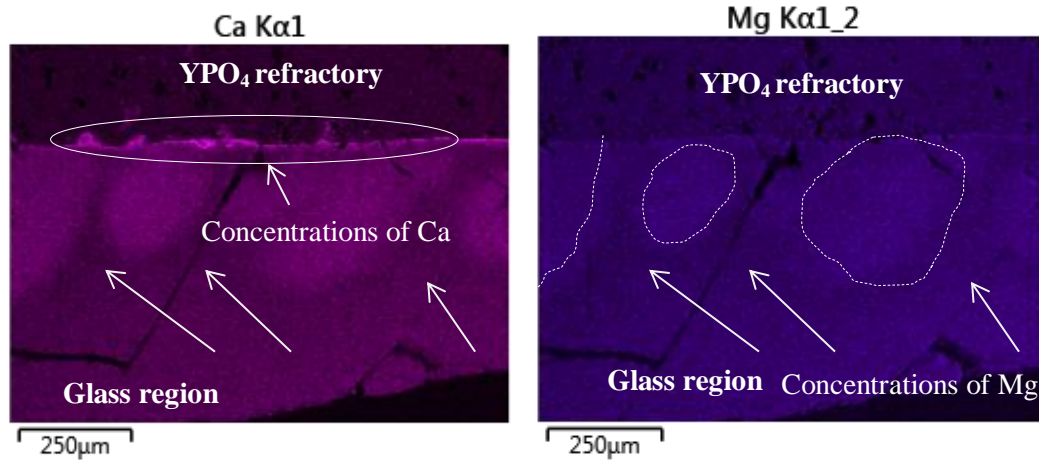


Figure 49. Elemental maps for Ca and Mg.

Elemental maps for Si, K and Al indicate depleted concentrations in these same regions demonstrating a migration of these species away from the concentrations of Y and P (Figure 50). Also observed are small concentrations for Si, K and Al within in the refractory, possibly as a result of glass penetration of the refractory. It is curious however, as was mentioned earlier, Si enrichment would have been expected for favoring phase separation as indicated by the Shelby and White phase diagrams which contradicts the apparent behavior.

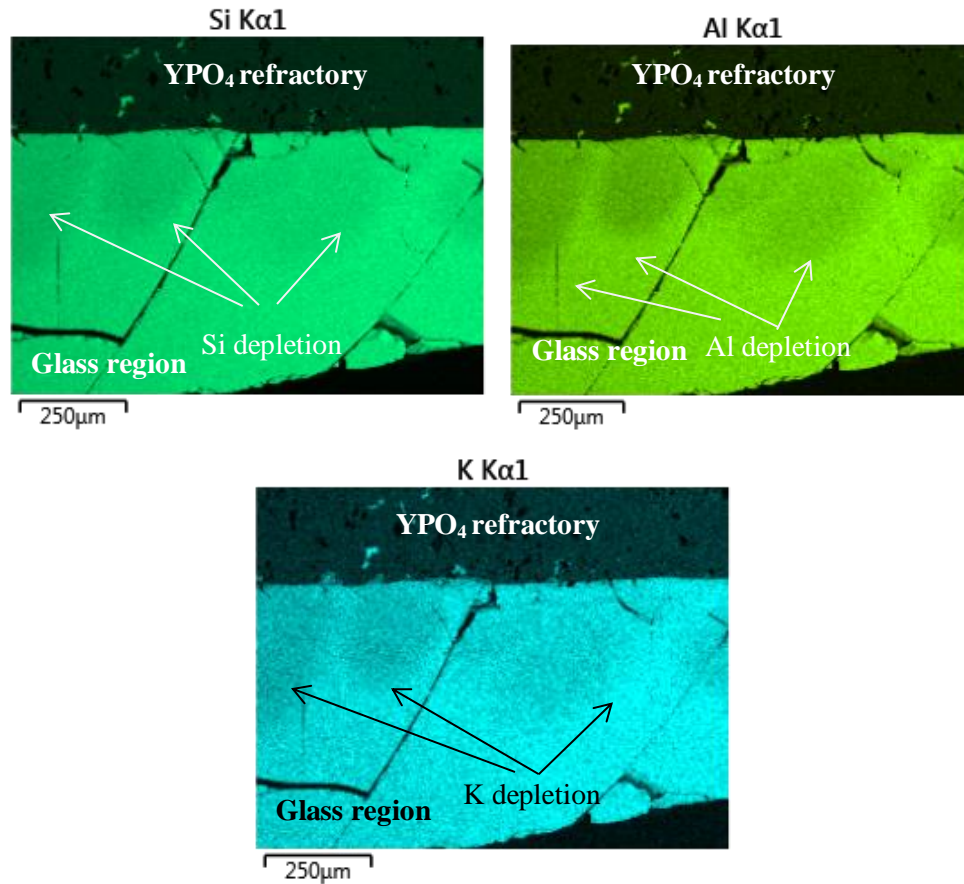
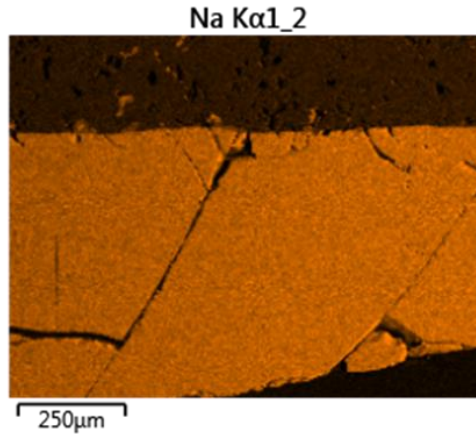


Figure 50. Elemental maps for Si, Al and K.

It is surprising that Na did not play an active role in this first sample. There were no discernable concentration alterations within the glass or cloudy regions and there was little evidence of migration into the refractory (Figure 51). It will be shown on a subsequent sample that Na took a much more active role suggesting a time and or temperature dependence on its activation.



**Figure 51. Elemental map for Na.**

It was initially believed that the migration of species to and from these regions of interest may have served as a precursor to crystal formation. Chemical mapping of a second sample was performed in an attempt to gain additional insight into any mechanisms that may have been taking place to cause crystal formation. This sample exhibited what was believed to be more advanced crystal development than the previous and was identified as the 72 h sample exposed to 1200 °C (Figure 52). Based on this data it was suspected these crystal developments were in fact not new developments rather remnants from the dissolution of a low temperature reaction layer formed on the base refractory. It will however be shown in the XRD and EPMA data that they are in fact new phases.

This particular sample image was interesting on first inspection as it demonstrated features of the reaction layer as well as the more advanced crystal development in the glass. In addition to the  $\text{YPO}_4$  base refractory located at the bottom of the image, chemical alterations to the boundary layer are also apparent. There is no appearance of the cloudy regions as observed in the previous sample, however there are mid-level grey nodules appearing near the interface within the glassy region and are labeled “mid-level grey phase” in the micrographs.

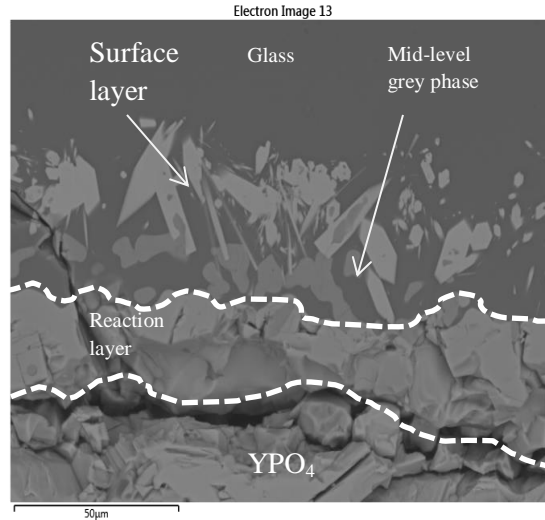


**Figure 52. Micrograph of chemical map region.**

Figure 53 shows the chemical mapping of both Y and P within the sample. Appreciable concentrations of both elements are found in the crystal structures located within the glass region. Presence of both elements is also demonstrated in the mid-level grey nodules near the reaction layer interface and a concentration gradient from the base refractory through the reaction layer is evident. Concentrations of Y in the crystallites within the glass appears to be higher than that of the nodule where the P concentrations appear to remain similar between both the nodule and the crystal. It will be shown later in line scan data that there exists a surface layer feature, especially in the low temperature samples, that possesses a high concentration of Y. This is likely the result of kinetic limitations as the lower mobility of Y into the glass at these temperatures causes a rate limiting step resulting in Y concentration increases at this interface.

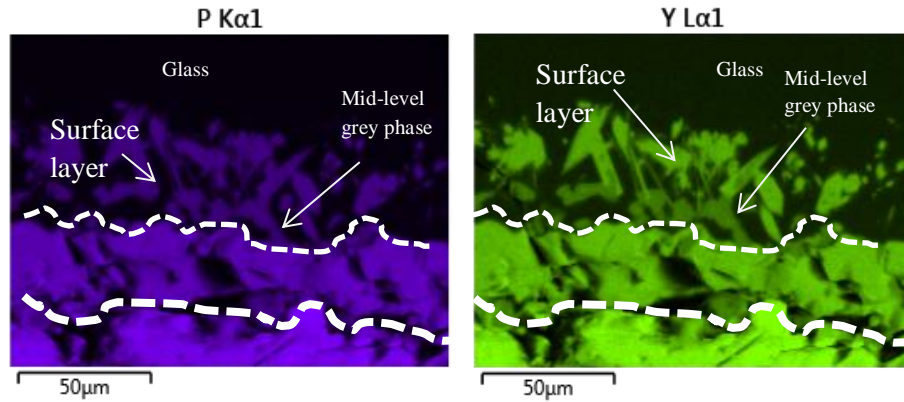


Figure 53. Elemental maps for P and Y.

Si has penetrated the reaction layer with low concentrations in this sample to a minimum depth of 50  $\mu\text{m}$  as indicated by the sample image (Figure 54). Si shows relatively high concentrations in the crystal developments within the glassy region though lower than that of the actual glass. This will later prove relevant in the final phase identification. Concentration levels within the nodules appear to be similar to those concentrations found in the reaction layer. Recall in the previous sample that Si concentrations in the cloudy regions also appeared depleted relative to Si concentrations found within the glass.

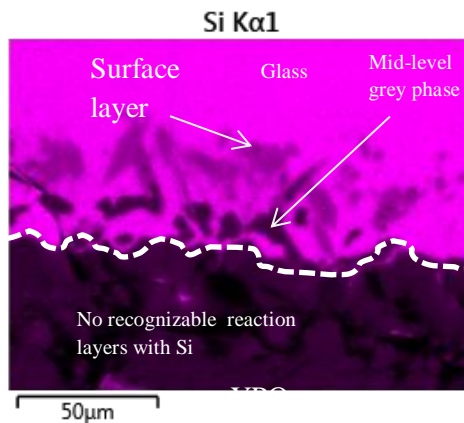
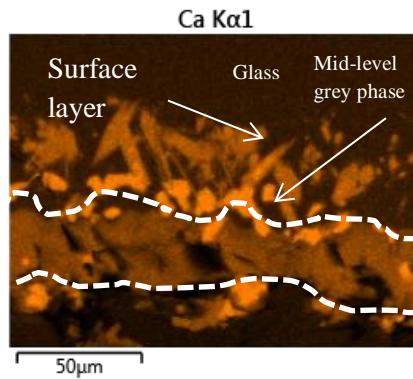


Figure 54. Elemental map for Si.

Relative to the glass, Ca concentrations are elevated in the crystal developments within the glassy region, the reaction layer and the mid-level grey nodules. This

concentration of Ca in the crystal developments will also prove relevant in the final phase identification. Several concentrated regions of Ca are observed within the reaction layer and may be related to the nodules located in the glassy region. Recall from the previous sample that Ca appeared to become concentrated at the glass/refractory boundary suggesting a high level of reactivity between it and the base  $\text{YPO}_4$  refractory. The diffusion of Ca at and into the reaction layer also suggests a high level of mobility. It is possible that the high mobility of Ca and its capability to help in maintaining a charge balance both contribute to its active participation in all levels of the reaction layer as observed in the mapping. This will be demonstrated in the line scan data later.



**Figure 55. Elemental map for Ca.**

Al, K and Na concentrations all appear depleted from the crystallized phase in the glassy region (Figure 56). Concentration levels of both Al and K appear depleted from within the mid-level grey nodules as well while the Na concentration in the mid-level nodules appear similar to the surrounding glass. For both K and Na, the development of a distinct phase boundary is evident, penetrating 25-30 μm into the  $\text{YPO}_4$  interface while Al does not appear to interact with the refractory. This would indicate a lower diffusivity of  $\text{Al}_2\text{O}_3$  relative to the other species, as would be suspected.

It was seen in the previous sample (Figure 44) that the Na chemical map did not reveal any discernible level of activity either in the formation of the cloudy regions or migrating into the refractory. The chemical maps shown here contradict this and show penetration well into the reaction layer.

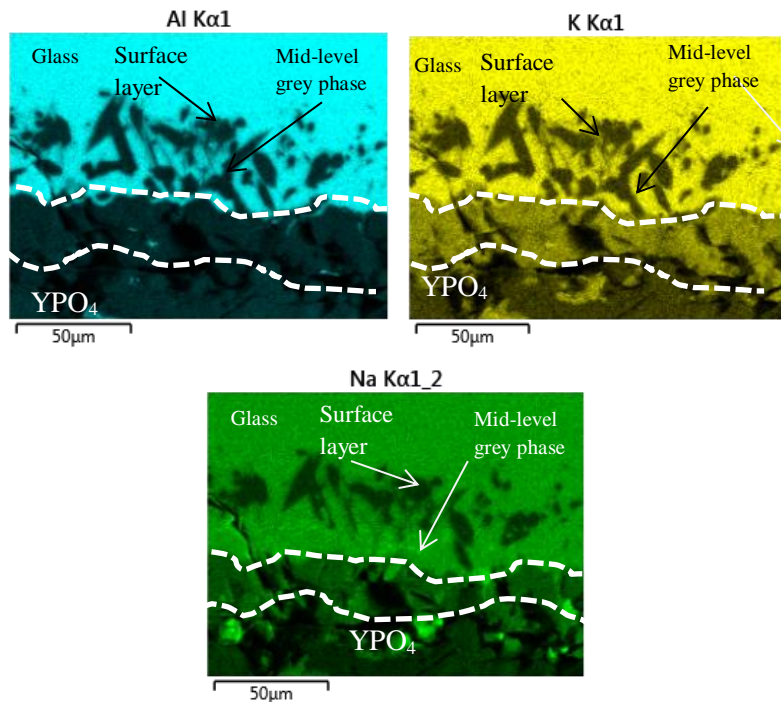
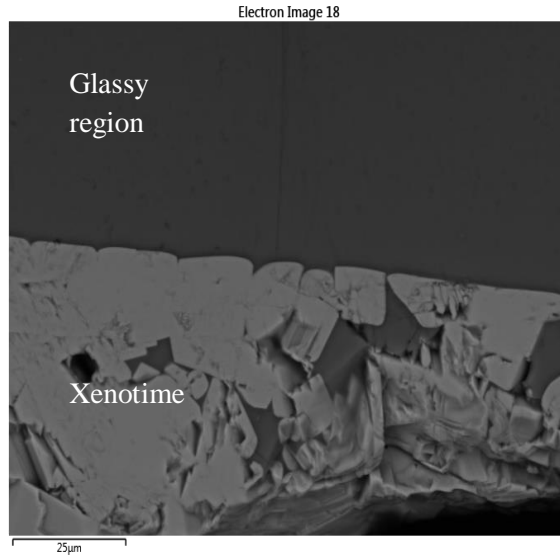


Figure 56. Elemental maps for Al, K and Na.

There appears to be a strong dependence on temperature and/or time in the development of these crystal formations within the glassy region. Chemical maps were made of the sample exposed to 1440 °C for a duration of 168 h (Figure 57). The sample appears unremarkable with no evidence of phase separation or crystal development. No boundary layers within the reaction layer are evident though this is likely attributable to the magnification and the base refractory not being captured in the image. It is also likely that the elevated temperature has improved the mobility of species diffusing away from the reaction layer resulting in a sharp boundary between the glass and refractory. The reaction interface between the glass and refractory is well-defined, indicating rapid dissolution of any products of reaction.



**Figure 57. Micrograph of chemical map region.**

Chemical maps for this sample (Figure 58) reveal a distinct boundary between the refractory and glass. There exist several areas near the surface where it is apparent glass has filled interior voids within the refractory. Despite the observance of crystal development in samples at the lower temperatures, no observable crystal formations nor cloudy, potentially phase separated regions, are apparent in these higher temperature samples. It is likely at these elevated temperatures that the viscosity of the glass is such that the products of the reaction are easily transported away from the surface and go into solution with the glass.

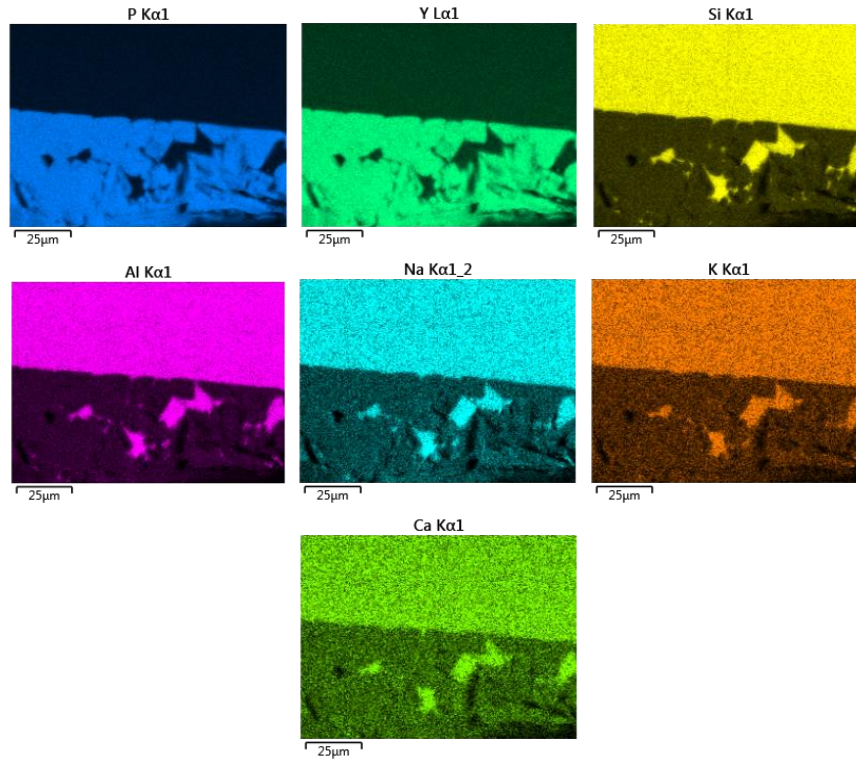


**Figure 58. Elemental maps for P, Y, Si, Al, Na, K, Ca.**

Samples exposed to 1050 °C for all three of the time durations exhibited development of distinct layers at the reaction boundary interface. Significant development of crystals in the glassy region however were not observed in lower temperature samples. Examination of micrographs for samples exposed to 1200 °C and 1250 °C all exhibited significant crystal development in the glassy regions. There appears to be less crystallization with increasing temperature beyond 1250 °C for all three time durations. However, as was shown earlier (Figure 43 and Figure 45), phase separation and crystallization was found at elevated temperatures revealing that there does appear to be evidence of crystal development at higher temperatures but, it is not supported that these higher temperature crystals are as a direct result of the Y enriched layer.

## B. Line Scans

A total of six line scans were performed to further develop an understanding of the migration of species and phase developments at and near the refractory/glass interface at both high and low temperatures as a function of the duration of exposure, Table XIV. (A suitable sample from the 24 h sample at 1150 °C was not available therefore, a scan from 1050 °C was substituted).

Table XIV. Line Scan Parameters

<i>Time (h)</i>	<i>Temperature (°C)</i>	<i>Temperature (°C)</i>
<b>24</b>	1050	1400
<b>72</b>	1150	1400
<b>168</b>	1150	1400

Line scans from the lower temperature samples demonstrated more pronounced reaction layer development than those from higher temperature samples. The sample area in Figure 59 exhibited obvious development of distinct layering within the reaction region. There are potentially five distinct regions represented in this image. At a distance between 0 and 2  $\mu\text{m}$ , the base xenotime refractory is well defined and clearly composed of Y and P and is represented as region 1. This region contains Y and P at 60 and 40 wt% oxide respectively. Additionally, there are three separate layers within the refractory, near the interface with the glass. The first of these regions is similar in appearance to the xenotime but defined by a fracture running parallel to the interface and is represented as region 2. This region appears to be one of transition where Y levels decrease rapidly between 2 to 3.6  $\mu\text{m}$ , decreasing from 60 to 26 wt% oxide while concentrations of Si, Sr and Ca are elevated as a result of their diffusion into the refractory. Concentrations of P remain unchanged through this region until the scan approaches 3.6  $\mu\text{m}$  where P concentrations begin to decrease continually before approaching 1 wt% oxide in the glassy region. Not surprisingly, this would suggest Y is more readily replaced by Ca and Sr than is P.

The dark grey region, region 3, represents an area of depleted Y, enriched Ca and strontium. Concentrations of P decrease through this region while Si increases. This

trend continues through regions 4 and 5. At approximately 4.5  $\mu\text{m}$ , it is observed that the concentration of Y reverses its downward trend and begins to increase while concentrations of Ca and Sr decrease. The tendency for Sr and Ca to behave similarly is not surprising as both species are divalent and will attempt to occupy similar structural positions. The rise in levels of Y peak in the region identified as region 4. It will be shown later that with respect to molar concentrations, both Ca and Y are enriched in this region as other species trend toward lower concentrations. This behavior of Ca and Y at this surface interface is indicative of the mechanism of uphill diffusion.<sup>24</sup>

This region appears as a thin surface layer directly in contact with the glassy region and is lightest in appearance on the micrograph. Within the wt% oxide data, this region is enriched with both Y and Si while P continues to decrease and all other constituents of the glass trend upward toward their nominal concentrations in the glass. The fifth region, at the extreme right of the image, is the glassy region. From 6  $\mu\text{m}$  to the extent of the scan, species making up the glass continue to trend toward their nominal glass compositional levels while concentrations of both Y and P continue to decrease but at a slower rate than observed in region 4.

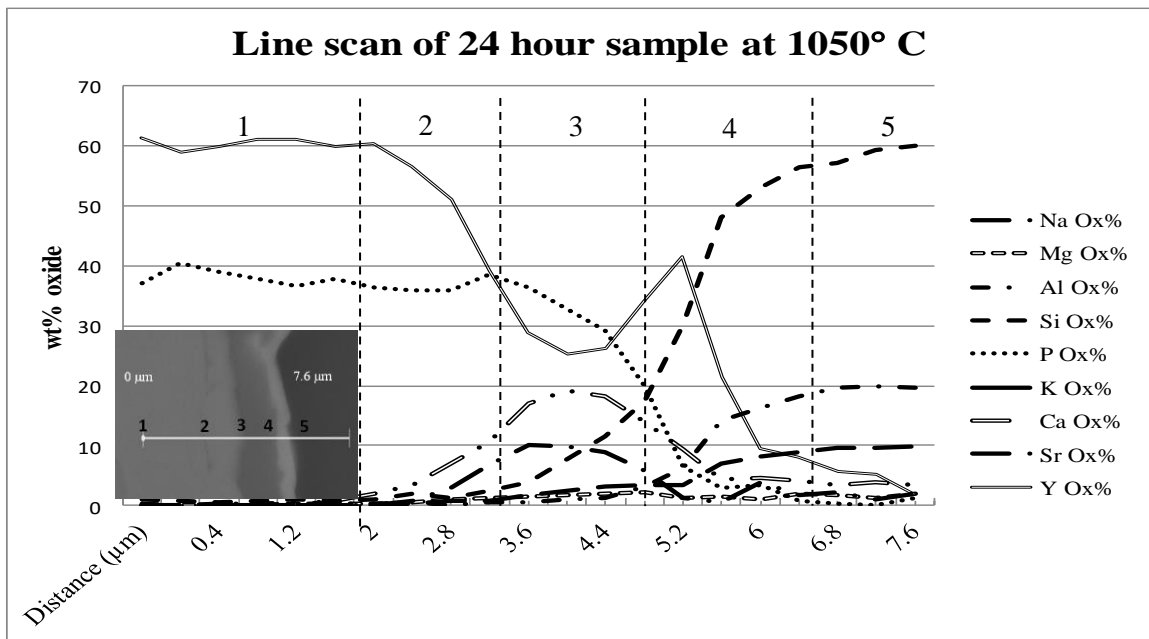


Figure 59. Line scan data for all elements with regions indicated.

Data for this plot was isolated to allow examination of only the five elements Y, P, Si, Ca and Sr (Figure 60). Si concentrations within the refractory begin to increase significantly at 3.2  $\mu\text{m}$ , as P begins to decrease. Between 3.2 and 2  $\mu\text{m}$  the concentration of Si remains constant at 1 % before approaching zero in the base refractory. Y concentrations increase in region 4, immediately adjacent to the glass region, between 4.8 and 5.2  $\mu\text{m}$  increasing from 26 % to 41 % before dropping off with depth into the glassy region. This spike also corresponds to a decrease in concentration for both Sr and Ca.

It is also noted within region 3 that there is a correlation between the depletion of P and the enrichment of Si suggesting a potential mechanism at work replacing P with Si. The similar structures make this swap possible. This region appears to be an area where alkali and alkaline earth species reach a maximum concentration. Ca appears to be dominant in this region.

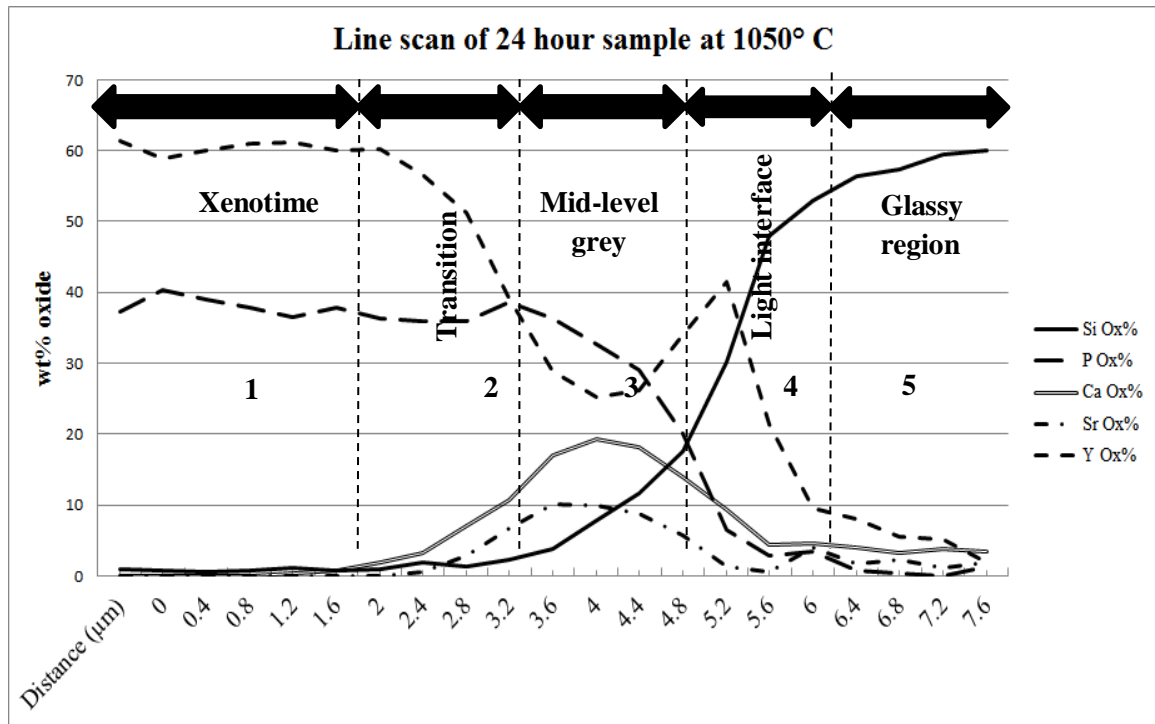


Figure 60. Line scan data for select elements.

In the glassy region 5, Y concentrations decrease slowly from 20 to 5 wt% oxide between 5.6 and 7.2  $\mu\text{m}$  while P remains at approximately 5 wt% oxide until 6  $\mu\text{m}$  where it then approaches concentration levels near zero.

All six of the line scans are consolidated in Figure 61 for side-by-side comparison with the low temperature samples on the left and high temperature samples on the right. The duration of exposure to heat increases from top to bottom with 24 h exposure at the top and 168 h on the bottom. The low temperature line scans on the left all exhibit the development of specific reaction layer boundary regions as described earlier. It is interesting to note the Y concentrations for the Y enriched region immediately adjacent to the glassy region vary between samples from 40 to 58 to 55 wt% oxide for the 24, 72 and 168 h samples respectively and it is not clear why this variation exists.

Diffusion of Si, Ca and Sr from the glass into the region of Y depletion is apparent within all samples. Concentrations of both Y and P extend well into the glassy region and beyond the scan region. For samples run at the higher temperatures, these concentrations remain near 10 wt% oxide well into the glassy region for the extent of the line scan, greater than 5  $\mu\text{m}$ . This is to be expected with the correlation of rate of dissolution and transport of reaction products at high temperatures being significantly increased. Y and P concentrations in those samples run at lower temperatures decrease rapidly and approach trace levels within 2  $\mu\text{m}$  of the interface.

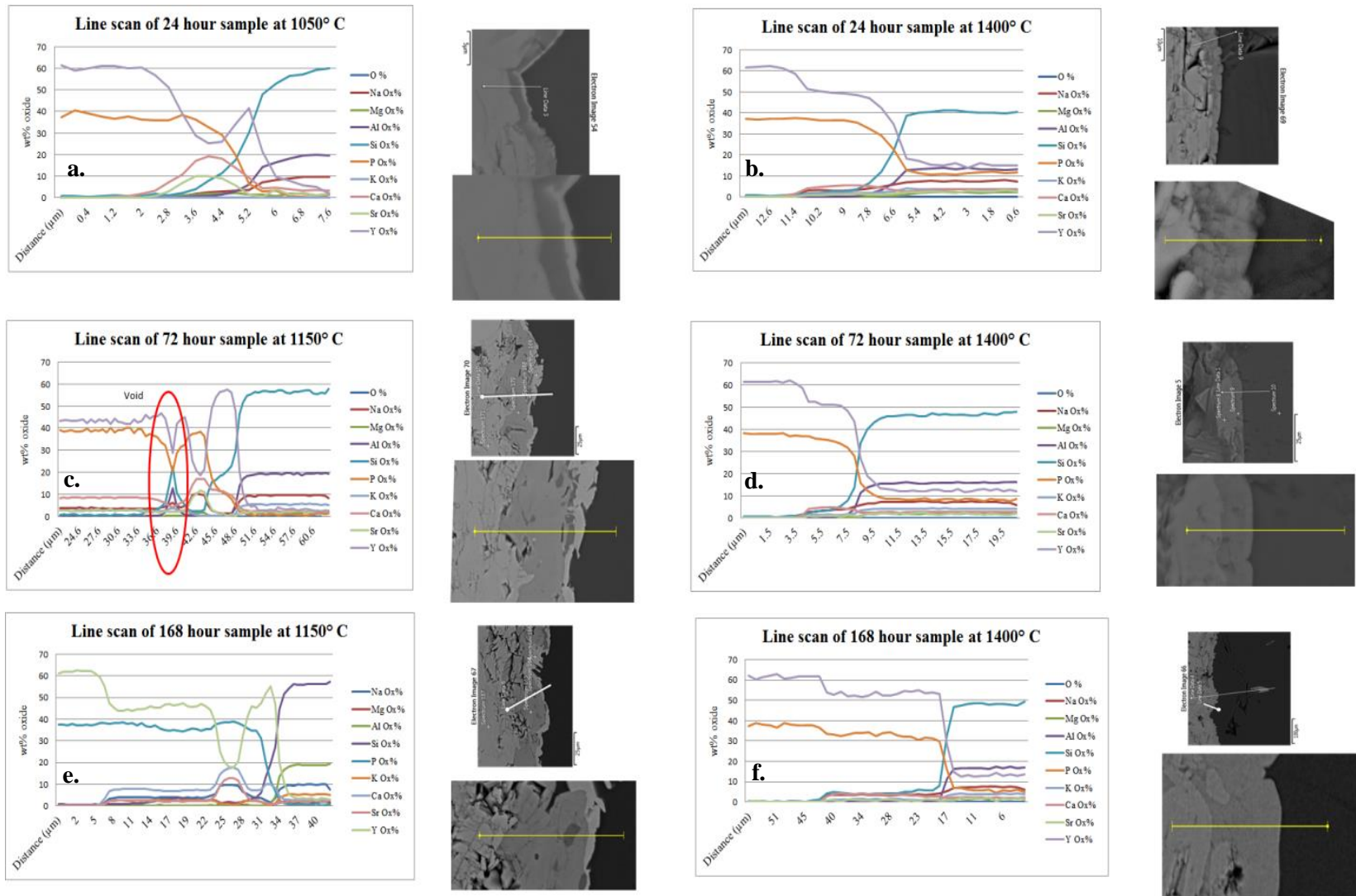


Figure 61 Full matrix of line scan plots in wt% oxide.

A qualitative comparison has been created (Table XV) to examine similarities between the crystallites and dark grey nodules found in the chemical mapping data and the results of the line scans. Of particular interest were the outermost two regions of the boundary layer, regions 3 and 4 and how they may compare to the nodules and crystallites.

Recalling the chemical mapping data, the dark grey nodules are Y depleted with P remaining near the concentration levels of the base refractory. Region 3 in the line scan data similarly demonstrates Y depletion while P concentrations begin to trend down. Concentrations of Si trended toward lower percentages in region 3 of the line scan which also is reflected in the chemical mapping data.

Comparing the crystallites found in the chemical mapping with region 4 of the line scans, the characteristically high concentration of Y with depleted levels of P is observed for both the crystallites and region 4. It is not surprising to note that concentrations of Si are high in the crystallites and region 4 while concentration levels decrease into region 3 and in the dark grey nodules. This does also serve as a marker of a diffusion gradient going from the glassy region which is Si rich to the xenotime base refractory.

**Table XV. Estimated Elemental Concentrations in Regions 3 and 4**

<i>A. Element</i>	<i>Chemical Map (Dark grey nodule)</i>	<i>Line scan (Region 3)</i>
Y	Low	38-25 %
P	High	38-19 %
Si	Low	20-2 %
Ca	Low	19-11 %

<i>B. Element</i>	<i>Chemical Map (Crystallite in glass)</i>	<i>Line scan (Region 4)</i>
Y	High	41-38 %
P	Low	19-5 %
Si	High	45-20 %
Ca	Low	14-5 %

Line scans b, d, e and f all clearly show a characteristic depletion of Y in the region within the refractory and nearest to the xenotime base material. The thickness of this layer appears to increase with the temperature and duration of exposure (Figure 62). Similarly, Si, Ca and Sr concentrations are enriched in each case within this region. There is little variation of concentrations of any of these species throughout this region indicating a steady state condition throughout the majority of this layer. This would suggest that higher temperatures and longer durations allow these species mobility and time to reach a condition of equilibrium.

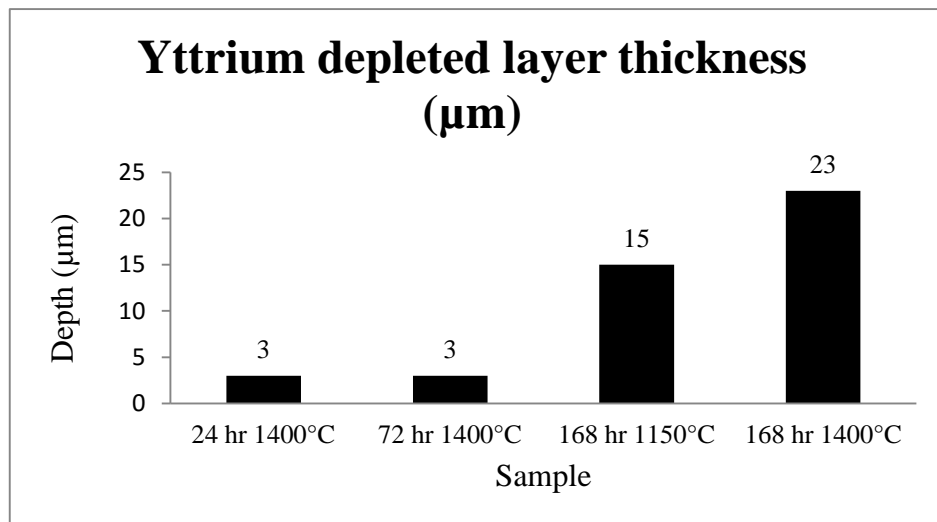


Figure 62. Plot of Y depleted layer thickness.

Spectral data from the line scan of the 168 h sample run at 1150 °C was taken at five positions as indicated on Figure 63 and compared to point spectrum data collected during the point spectrum scans obtained during the EDS characterization. The base xenotime material extends from 0 to 6 µm in the line scan. Data for comparison to the point spectrum data was taken at 5 µm and compared to several of the point spectrums obtained earlier.

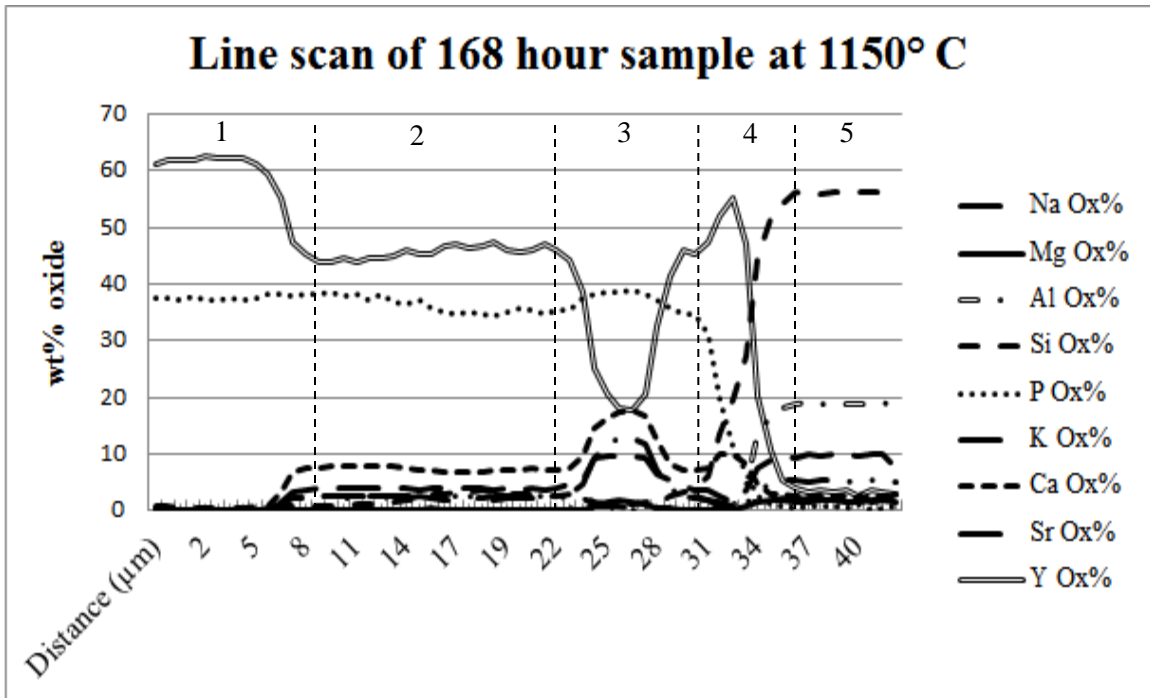
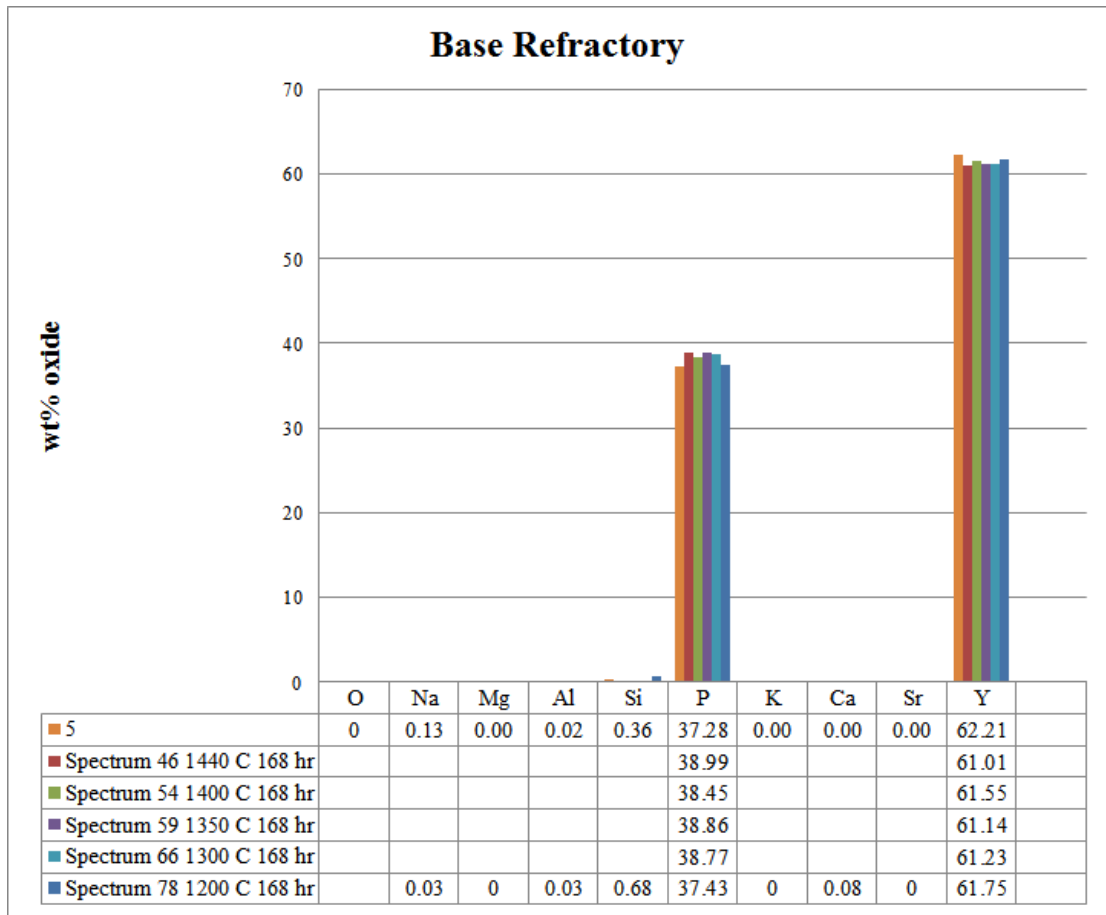


Figure 63. Line scan data is plotted.

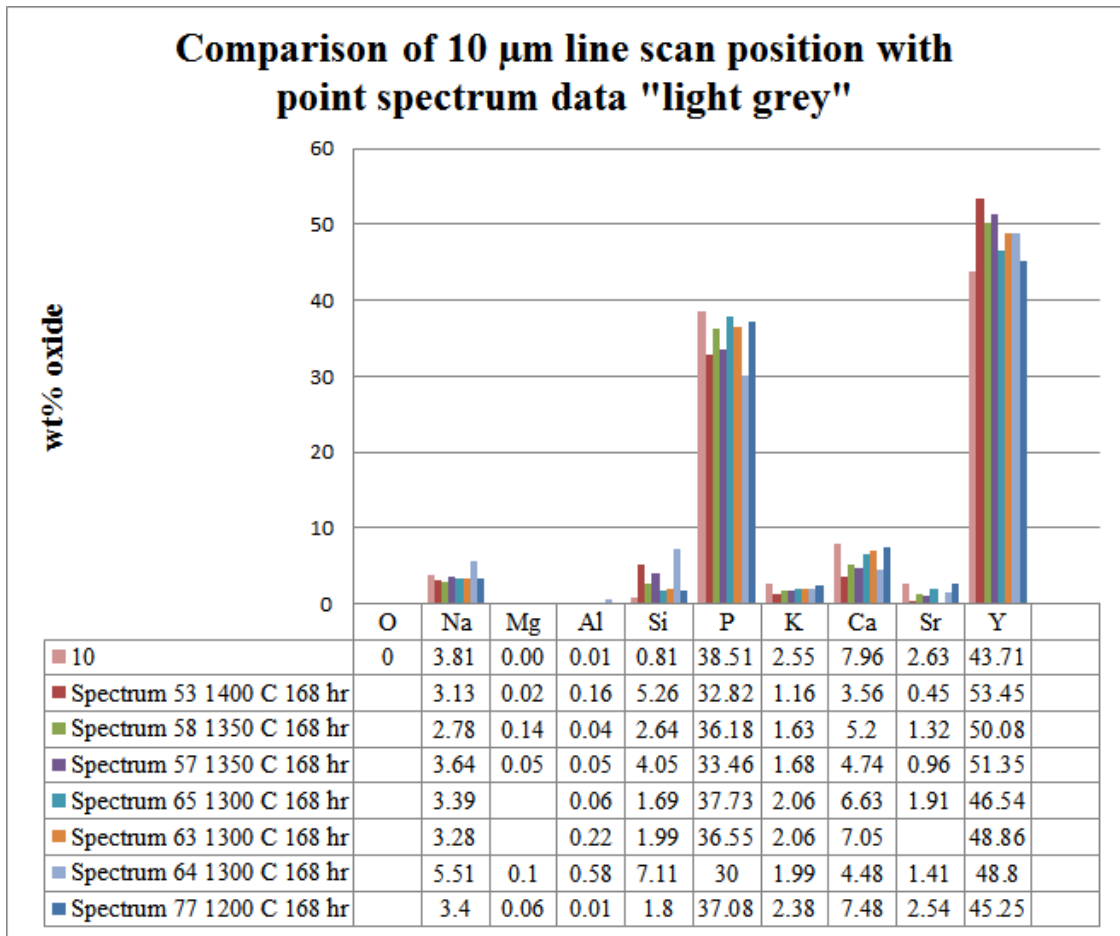
Comparison of the line scan data with the point spectrum data for the base refractory reveals nothing unexpected or remarkable (Table XVI) with concentrations of Y and P matching well to that of the base refractory. It is noted that the 5 µm position was chosen for its close proximity to the first indications of diffusion and even at this close proximity, no other species are detected indicating a very well defined boundary interface.

Table XVI. Line Scan Data at 5  $\mu\text{m}$  is Compared to Point Spectrum Data



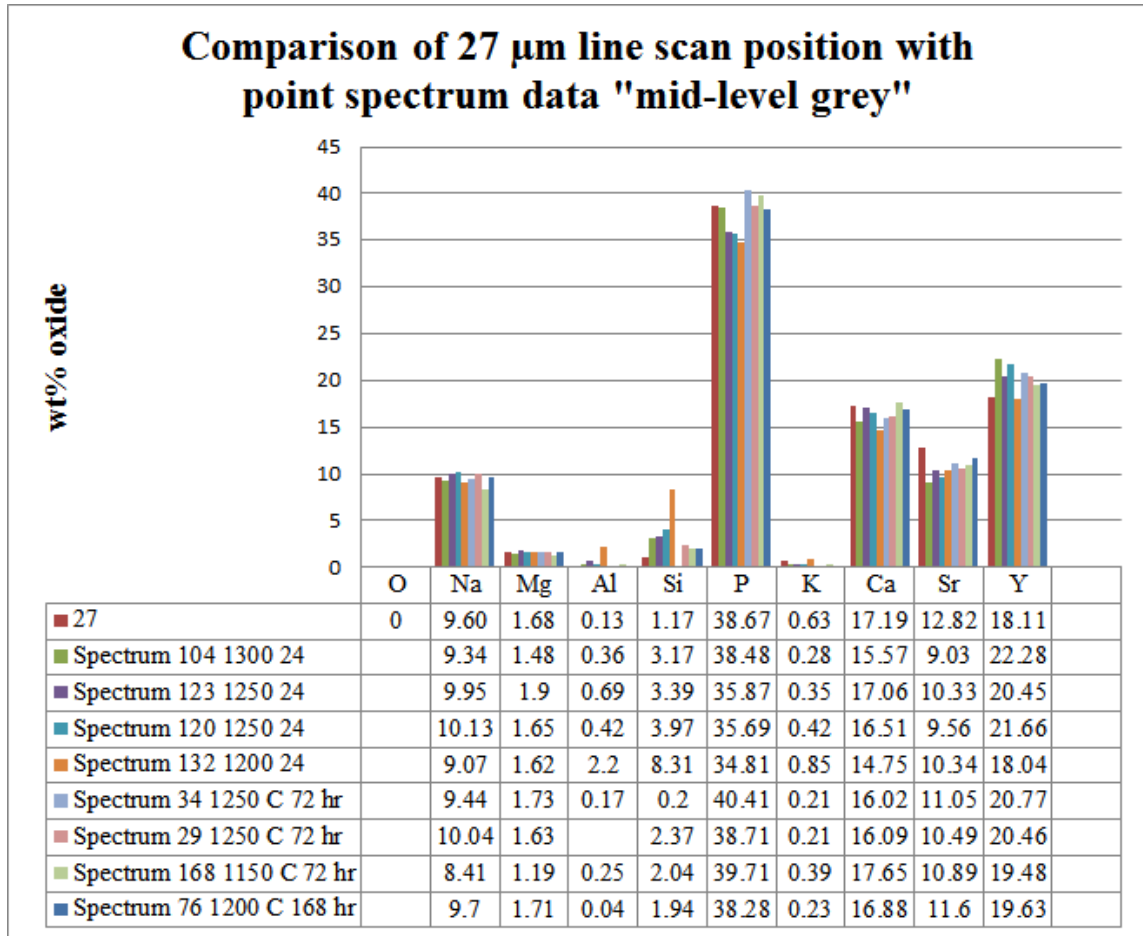
The Y depleted region was examined in a similar manner to the base refractory using data from the line scan taken from the 10  $\mu\text{m}$  position. Spectral data from this position matches well with the spectral data observed earlier and categorized as light grey (Table XVII). The data is consistent with a depletion of Y and enrichment of Sr, Ca, Na, P and Si. The data shown here represents a sampling of the point spectrum data collected and identified as “light grey”. This phase was found across samples at all temperatures and time, not only at 168 h.

Table XVII. Line Scan Data at 10  $\mu\text{m}$  is Compared to Point Spectrum Data



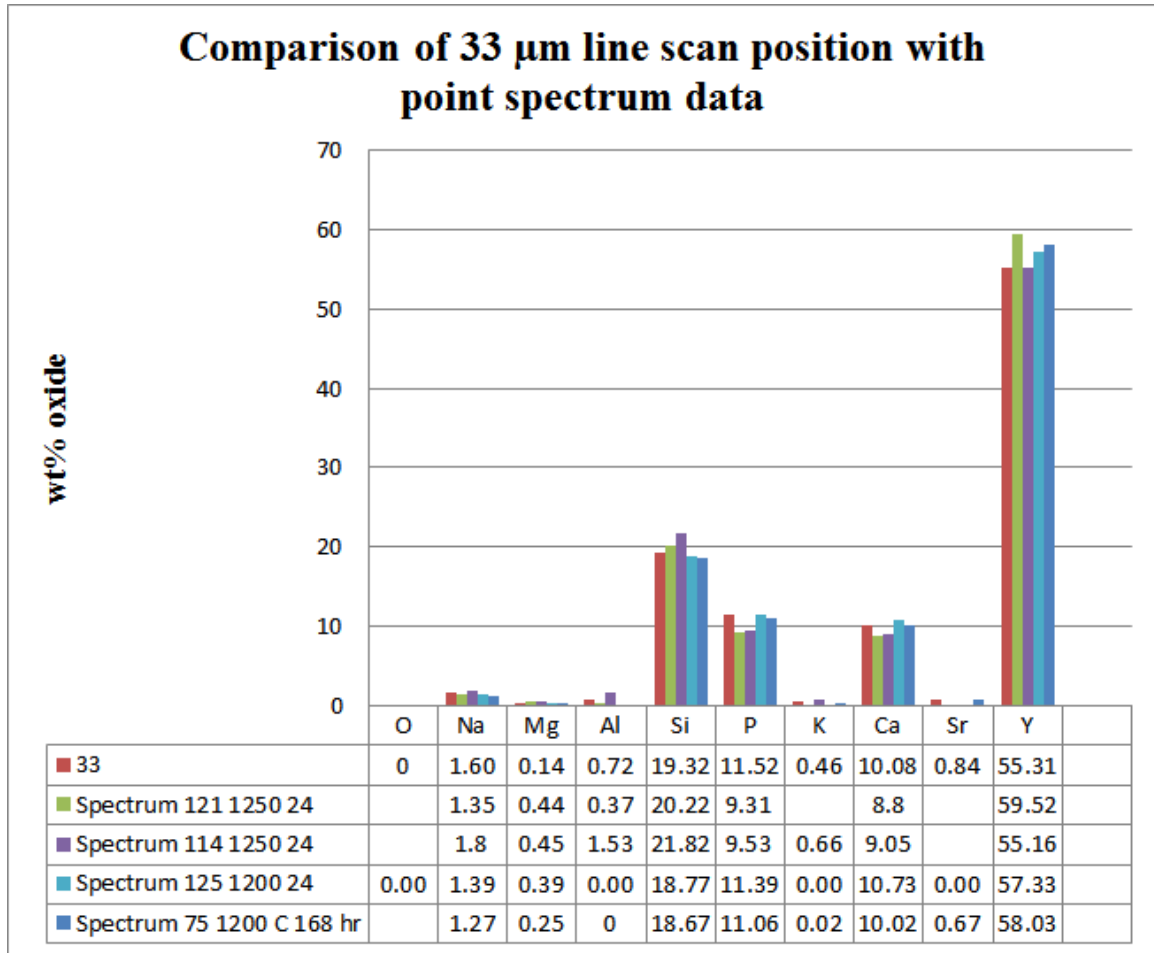
Similar to the light grey region, point spectrum data for the feature identified as “mid-level grey” was abundant throughout the sample population. The correlation between line scan data from the position at 27  $\mu\text{m}$  and other point spectrum data classified as mid-level grey is obvious (Table XVIII). The abundance of data for this phase indicating it is a major constituent to the reaction layer between the xenotime and 727XW glass.

Table XVIII. Line Scan Data at 27  $\mu\text{m}$  is Compared to Point Spectrum Data



The Y enriched layer immediately adjacent to the glassy region proved much less abundant than other regions. In all, only four point spectrum from the EDS data were found to correspond to data from the line scan taken at the 33- $\mu\text{m}$  position. Three of the four point spectrum were from the 24 h samples while the third was from the sample run at 1200  $^{\circ}\text{C}$  for 168 h. All four point spectrum data were taken from samples run at either 1200  $^{\circ}\text{C}$  or 1250  $^{\circ}\text{C}$  (Table XIX). The line scan was performed on a sample run at 1150  $^{\circ}\text{C}$ . This phase does not appear to be abundant within the sample set and is prevalent at lower temperature ranges, likely favoring going into solution at higher temperatures. Additionally, of the six line scans performed, this Y-enriched phase was only observed on the three lower temperature scans.

Table XIX. Line Scan Data at 33  $\mu\text{m}$  is Compared to Point Spectrum Data



The micrograph from which point spectrum 75 was taken reveals what appears to be the reaction layer observed in the previous line scan but in a state of partial dissolution into the glassy region, Figure 64. Boundaries for other reaction layers are readily observed in this image moving into the base refractory and away from the glassy region. Well defined crystals are observed in this outermost portion of the reaction layer in the glassy region.

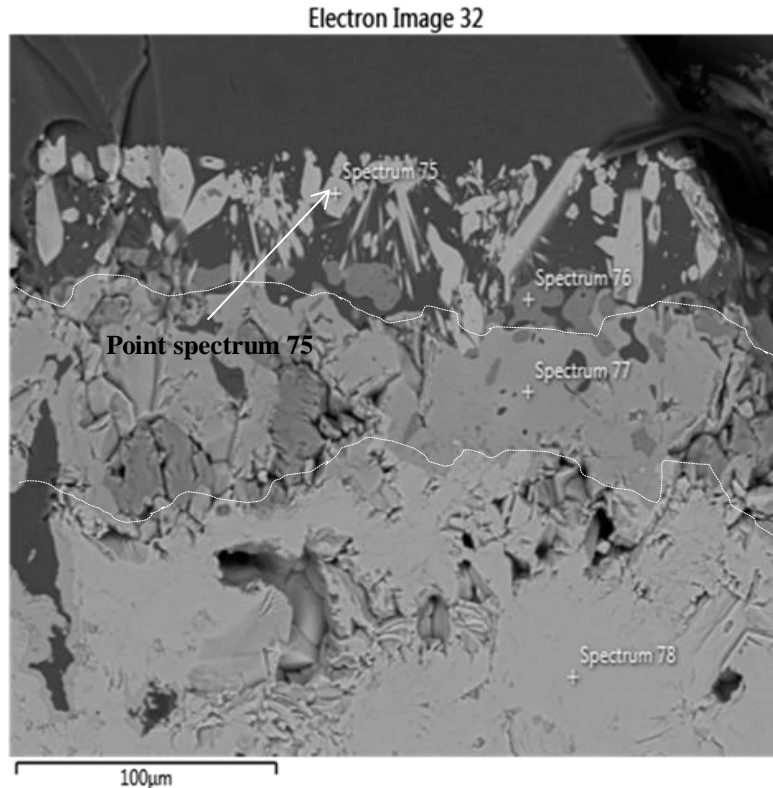


**Figure 64. Micrograph for point spectrum 75.**

Boundaries between different zones have been highlighted in the micrograph for clarity. Other point spectrum from this sample correspond to the base xenotime refractory, spectrum 78, the light grey phase, spectrum 77 and the mid-level grey phase, point spectrum 76. This would suggest the longer duration of 168 h was a factor in the dissolution of the Y-enriched phase for this and other samples. Furthermore, what on first inspection appear to be crystals growing in the glassy region may be remnants of the Y-enriched layer (recall region 4 from the line scans) as they enter the glassy region during dissolution. As such, this phase likely only exists below approximately 1250 °C. Evidence of intermixed regions of the mid-level grey phase with the lighter phase would also suggest some level of active migration of these regions towards the glassy region as the Y enriched layer goes into solution.

The ultimate goal of this work is to identify phases created during the dissolution process and as such, it is recognized that analysis of the data in a molar % basis may provide a clearer relationship between the species found through EDS and the phases

identified in the XRD characterization. As was done with the point spectrum EDS data, line scan data was converted from an wt% oxide basis to mol%. Data for these scans in mol% were compiled similarly as was done with the previous line scan plots presented as an wt% oxide basis (Figure 65).

The conversion to a mol% reveals a relationship not observed in the wt% oxide data relative to the initial drop in Y concentrations. It is observed in the molar % data that there is a coinciding decrease in P and Y going towards the glass interface but within the xenotime refractory. Recall from the wt% oxide data, only Y appeared to decrease in the region adjacent to the base material. This suggests both Y and P attempt to maintain a 1:1 molar ratio through region 2. Examining the plots from Figure 65a. through f. (in order of increasing time and temperature), the lower time and temperature sample (Figure 65 a.) shows a Y:P ratio of less than 1 through regions 2 through 4 while in the higher temperature, longer duration scan (Figure 65 f.) the 1:1 relation is maintained throughout the reaction layer. This suggests a stoichiometric relationship between Y and P throughout the reaction layer.

Similar behaviors of the alkali and alkaline earth species are evident in molar data as was seen in the wt% oxide data. As previously discussed, the diffusion of Ca into the xenotime base refractory increases significantly at the reaction layer. In terms of mol%, it is observed that Ca is the dominant species reaching a concentration of near 34 wt% oxide in the mid-level grey region, region 3. This behavior is apparent throughout the samples though the molar concentration appears to decrease with temperature and time until the 168 h sample at 1400 °C where it increases from its equilibrium concentration in the glass of about 4 to approximately 10 mol% where it remains through the depth of penetration. In this highest temperature sample, with the longest duration, there is no indication of a concentrated region at the boundary with the glass suggesting increased mobility due to the lower viscosity of the glass.

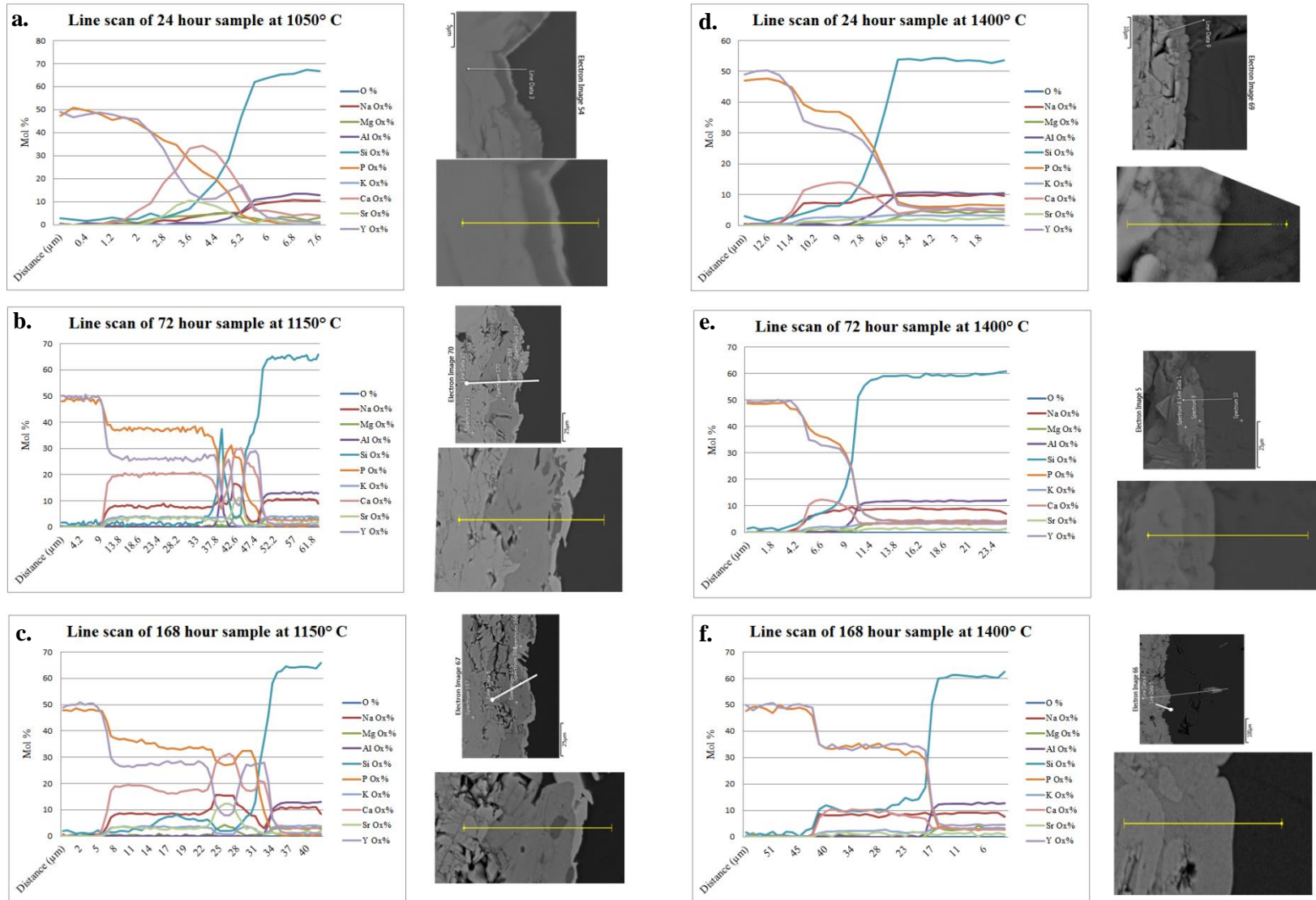


Figure 65. Matrix of line scans converted to mol %.

### C. Chemical Recalculation

Efforts were made to perform chemical recalculation to determine potential chemical formulas for the phases present in the samples. An excel spreadsheet was created which allowed for chemical recalculation of the formula by performing a parametric sweep of the number of oxygen atoms expected in the formula. EDS data for the wt% oxide were chosen and input into the spreadsheet Table XX. From this, the mole units of each oxide were calculated and then the corresponding number of oxygen units calculated based on the mole units. Oxygen units are then normalized to a user selected number of oxygen for the formula. The calculated atomic unit for the cation is then calculated based on the normalized oxygen unit to the number of cations.

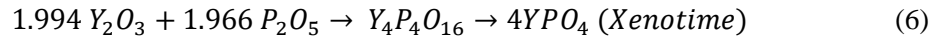
Table XX. Chemical Recalculation for Sampled Data

Sample: **1150C 72 hr linescan** Oxygens per formula =  
 Oxy = **8**

<i>Oxide</i>	<i>GFW (formula weight)</i>	<i>Wt. %</i>	<i>Mole Units (mol#)</i>	<i>Oxygen Units (O#)</i>	<i>Normalized Ox. Units</i>	<i>Atomic Units</i>	<i>Element</i>
SiO2	60.084	0.53	0.00883	0.01765	0.06497	<b>0.03248</b>	<b>Si</b>
TiO2	79.866	0.00	0.00000	0.00000	0.00000	<b>0</b>	<b>Ti</b>
Al2O3	101.961	0.19	0.00182	0.00547	0.02015	<b>0.01343</b>	<b>Al</b>
Cr2O3	151.9902	0.00	0.00000	0.00000	0.00000	<b>0</b>	<b>Cr</b>
Fe2O3	159.688	0.00	0.00000	0.00000	0.00000	<b>0</b>	<b>Fe+3</b>
FeO	71.844	0.00	0.00000	0.00000	0.00000	<b>0</b>	<b>Fe+2</b>
MnO	70.937	0.00	0.00000	0.00000	0.00000	<b>0</b>	<b>Mn</b>
MgO	40.304	0.00	0.00000	0.00000	0.00000	<b>0</b>	<b>Mg</b>
CaO	56.077	0.00	0.00000	0.00000	0.00000	<b>0</b>	<b>Ca</b>
Na2O	61.979	0.03	0.00050	0.00050	0.00186	<b>0.00093</b>	<b>Na</b>
K2O	94.196	0.19	0.00199	0.00199	0.00734	<b>0.00367</b>	<b>K</b>
H2O	18.015	0.00	0.00000	0.00000	0.00000	<b>0</b>	<b>H</b>
P2O5	141.94	37.91	0.26707	1.33537	4.91521	<b>1.96608</b>	<b>P</b>
SrO	103.62	0.00	0.00000	0.00000	0.00000	<b>0</b>	<b>Sr</b>
Y2O3	225.82	61.16	0.27082	0.81245	2.99047	<b>1.99365</b>	<b>Y</b>
<b>Totals</b>		<b>100.00</b>	<b>0.55104</b>	<b>2.17345</b>	<b>8.000</b>	<b>4.010</b>	

The sample shown in Table XX was deliberately taken from a position easily identified as the base refractory and used as an initial test of the software capability. The expected formula therefore was known to be YPO<sub>4</sub>. The resultant atomic units with 8

oxygen's present for the given weight percent resulted in values of 1.996 and 1.994 for  $P_2O_5$  and  $Y_2O_3$  respectively. Therefore:



Efforts to perform similar chemical recalculations throughout the sampled data proved unsuccessful in its capability to aid in the identification of the phases present in the samples and this effort was abandoned. It is likely that the significant number of alkali and alkaline earth ions present in the solution contributed to the issue with this method. Na, Mg, K Ca and Sr all were present throughout the reaction layer and had potential for swapping and misidentification.

A long duration scan was performed on the SEM to gain improved chemistry data to be used in the identification of the phases developed at the glass/refractory boundary. The sample used for this was chosen at the time specifically for the large crystal in the glassy region identified by spectrum 135 in Figure 66.

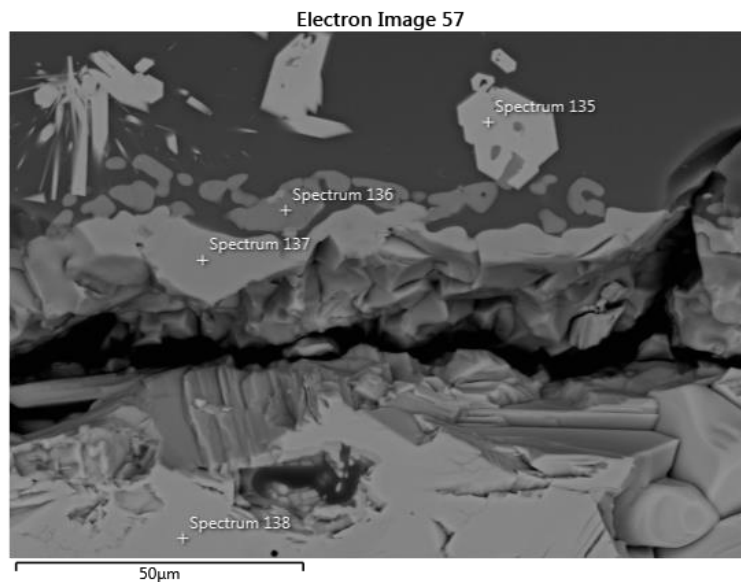
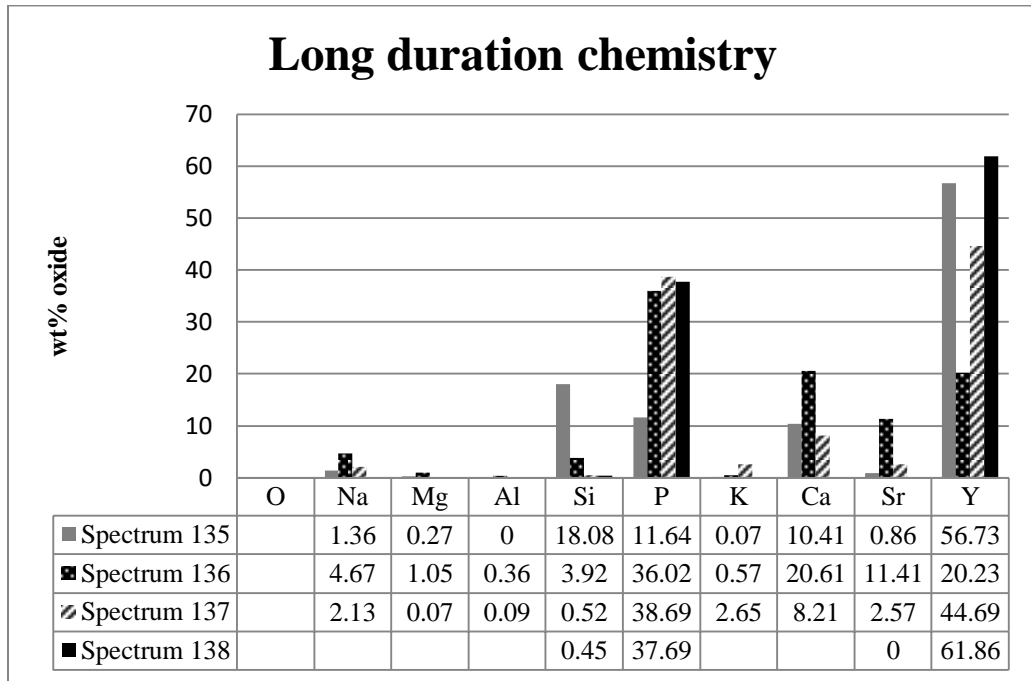


**Figure 66. Micrograph from long duration spectral scan.**

Data for these scans is plotted in Table XXI and shows clearly the xenotime layer represented by spectrum 138. Spectrum 137 could not be matched to any particular result previously identified and spectrum 136 was likely not accurate due to what was suspected to be a large interaction volume from the scan. Spectrum 135 showed some promise of being able to identify a better chemistry due to its large size.

Table XXI. Long Duration Chemical Data



An attempt was made to utilize proprietary software owned by Corning Inc. for performing chemical recalculation of the phases found in the sample. Though based on the same principles as the manual excel method described previously, it was thought that the integration of this software with the EDS data may provide more accurate results. Attempts were made for all four data points. The only calculation with any level of confidence appeared to be for point spectrum 135, though even this data should be viewed with some level of skepticism. The number of oxygen atoms were adjusted for each sample to try to achieve charge balance of the sample data, (Table XXII). The resultant data calculated by the program suggested a formula of; Na(.08) Mg(.12) Ca(3.35) Sr(.15) Si(5.43) Y(9) P(2.96) O(36).

There is some level of confidence in this suggestion. However, due to the complexity and number of ions playing a role in the balance of the formula it is believed the interaction volume of the beam is likely to have overlapped with other regions leading to the inclusion of species which may not have been a component of this particular phase. Ultimately the results of this effort remain inconclusive.

**Table XXII. Commercial Chemical Recalculation Software**

Spectrum 135	Line Type	Apparent Concentration	k Ratio	Wt%	Wt% Sigma	Oxide	Oxide %	Oxide % Sigma	Number of Ions	Standard Label
<b>O</b>				31.92					36	
<b>Na</b>	K series	7.18	0.0303	1.01	0.01	Na2O	1.36	0.01	0.79	Albite
<b>Mg</b>	K series	1.04	0.00689	0.16	0.01	MgO	0.27	0.01	0.12	MgO
<b>Al</b>	K series	0	0	0	0	Al2O3	0	0	0	Al2O3
<b>Si</b>	K series	67.72	0.53665	8.45	0.02	SiO2	18.08	0.04	5.43	SiO2
<b>P</b>	K series	54.96	0.30743	5.08	0.02	P2O5	11.64	0.05	2.96	GaP
<b>K</b>	K series	0.39	0.0033	0.06	0.01	K2O	0.07	0.01	0.03	KBr
<b>Ca</b>	K series	53.65	0.47939	7.44	0.01	CaO	10.41	0.02	3.35	Wollastonite
<b>Sr</b>	L series	5.42	0.04768	0.73	0.04	SrO	0.86	0.04	0.15	SrF2
<b>Y</b>	L series	274.61	2.74608	44.67	0.05	Y2O3	56.73	0.06	9.07	Y
<b>Sb</b>	L series	2.58	0.02577	0.46	0.03	Sb2O3	0.55	0.04	0.07	Sb
<b>Ba</b>	L series	0.07	0.00063	0.01	0.02	BaO	0.01	0.02	0	BaF2
<b>Total</b>				100			100		21.97	(Cation sum)

## D. Powder XRD and HTXRD

Room temperature XRD was performed on a total of seven samples. Six samples were melts that combined powdered xenotime with 727XW glass and the seventh was pulverized xenotime created from a sample of XB-1. Of the melts, two were prepared from XB-1, two from FC-01 and two from P7 as detailed in the experimental procedure section C. All of the melts prepared at the lower temperature (1150 °C) exhibited several crystalline phases while the higher temperature (1400 °C) showed higher amorphous behavior and fewer phases. Findings are tabulated in Table XXIII.

Xenotime (YPO<sub>4</sub>) was observed in all but one sample, the FC-01 sample taken to 1400 °C for 24 h which exhibited a fully amorphous structure. It is not surprising that all of the lower temperature melts exhibited a higher degree of crystalline phases than did the high temperature samples. In addition to xenotime, all three low temperature melts were found to have calcium potassium phosphate, Ca<sub>10</sub>K(PO<sub>4</sub>)<sub>7</sub>, yttrium phosphate hydrate, YPO<sub>4</sub>·8H<sub>2</sub>O and xenotime, YPO<sub>4</sub>. The P7 and XB-1 samples also were found to have calcium yttrium oxide silicate Ca<sub>4</sub>Y<sub>6</sub>O(SiO<sub>4</sub>)<sub>6</sub> in the low temperature samples.

Calcium yttrium oxide silicate was also identified in the high temperature sample for the XB-1 melt.

The calcium potassium phosphate,  $\text{Ca}_{10}\text{K}(\text{PO}_4)_7$ , has similarities to an apatite ( $\text{Ca}_{10}(\text{PO}_4)_6(\text{X})_2$  ( $\text{X}=\text{OH}, \text{F}, \text{Cl}, \text{Br}$ ). Wolf and London have shown the direct link between apatite dissolution and monazite crystallization.<sup>25</sup> It has been suggested that if apatite contained abundant Y then presumably xenotime would crystallize during the dissolution of apatite rather than monazite. The direct correlation to the dissolution of xenotime in the current experiment presented here is not clear, it is however worth noting.

**Table XXIII. Phases Identified in XRD Samples**

Phase	Sample					
	P7 @1150° C for 72 h	FC01 @1150° C for 72 h	XB-1@1150° C for 72 h	P7 @1400° C for 24 h	FC01 @1400° C for 24 h	XB-1 @1400° C for 24 h
$\text{Y}(\text{PO}_4)$	X	X	X	X		X
$\text{YPO}_4 \cdot 8\text{H}_2\text{O}$	X	X	X	X		X
$\text{Ca}_{10}\text{K}(\text{PO}_4)_7$	X	X	X			
$\text{Ca}_4\text{Y}_6\text{O}(\text{SiO}_4)_6$	X		X			X
$\text{Ba}_4\text{Y}_4\text{O}_9$			X			

Sampled data was analyzed using Jade software together with the PDF-4<sup>+</sup> powder diffractions database. Search criteria was primarily by chemistry, identifying all of the possible elements. To achieve a baseline, the pure xenotime sample was indexed first and then subsequent samples (Figure 68, Figure 69, Figure 70, Figure 71, Figure 72 and Figure 73). The xenotime sample taken from XB-1 and prepared for powder diffraction at room temperature showed three characteristic strong peaks at 25.849° two-theta with  $d=3.4439\text{Å}$ , 34.998° two-theta with  $d=2.5618$  and 51.766° two-theta with  $d=1.7646$ , Figure 67.

The low temperature FC-01 sample (Figure 70) exhibited a stronger amorphous structure than the other samples suggesting the FC-01 powder advanced through the dissolution process more readily than the others, possibly due to a smaller particle size. As would be expected, the xenotime phase was found throughout the samples except for the FC-01 sample at 24 h duration and 1400 °C where only an amorphous phase was detected, Figure 71.

The powder XRD samples from the lower temperature samples run for 72 h all exhibited more significant phase development than the samples created at the higher temperature and a shorter duration. This was not surprising as this behavior was also present in the lower temperature gradient boat samples used in the SEM analysis and logically, there is a higher propensity for dissolution of crystal phases at the elevated temperatures. Additionally, the longer duration may be necessary to allow for crystal development. The hydrated  $\text{YPO}_4$  was believed to have formed as a result of the room temperature diffraction method. In the presence of humidity, phosphates show a strong affinity to water. Characteristic of this  $\text{YPO}_4 \cdot 0.8\text{H}_2\text{O}$  is a peak at 14.984 two-theta.

It was suspected the samples being exposed to ambient air were allowed to acquire water resulting in the phase change. Only the fully amorphous sample of FC-01 at 1400 °C did not exhibit this phase, which supports the position that this was ambient water being introduced to the sample upon cooling during the sample preparation, not that it was formed during the melt. Under the assumption that the hydrate forms in ambient conditions, the only phases that developed in the samples at elevated temperatures would therefore be calcium potassium phosphate,  $\text{Ca}_{10}\text{K}(\text{PO}_4)_7$  and calcium yttrium oxide silicate  $\text{Ca}_4\text{Y}_6\text{O}(\text{SiO}_4)_6$ . The base refractory  $\text{YPO}_4$  was also indexed however was not a new phase development.

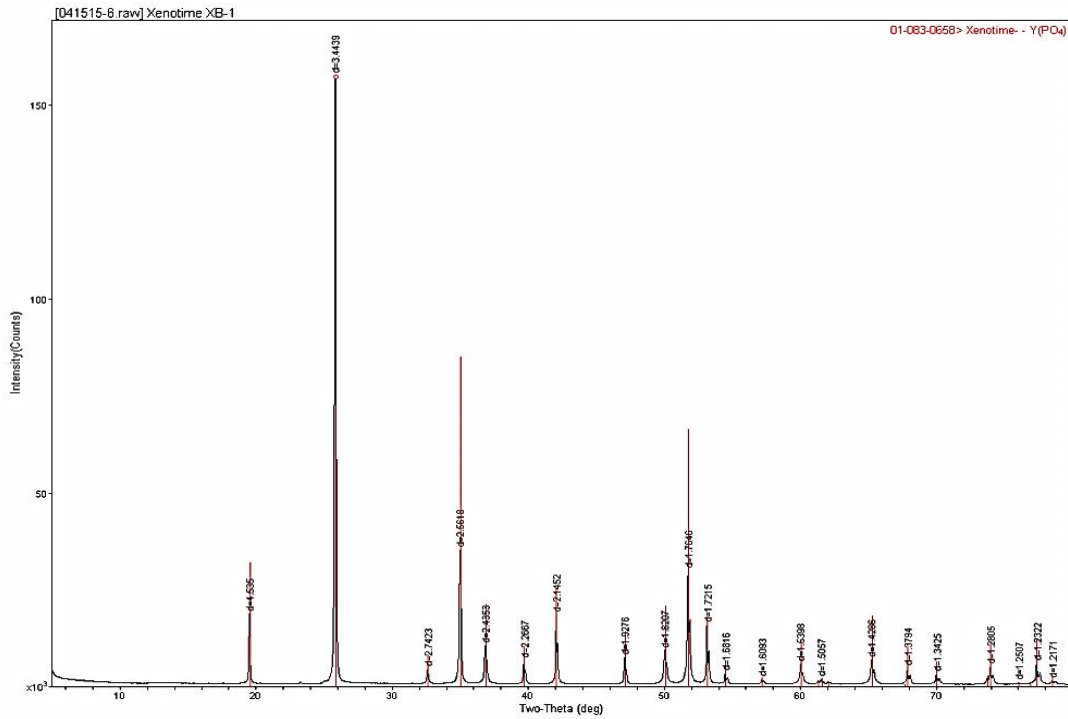


Figure 67. Room temperature powder XRD trace with phase ID.

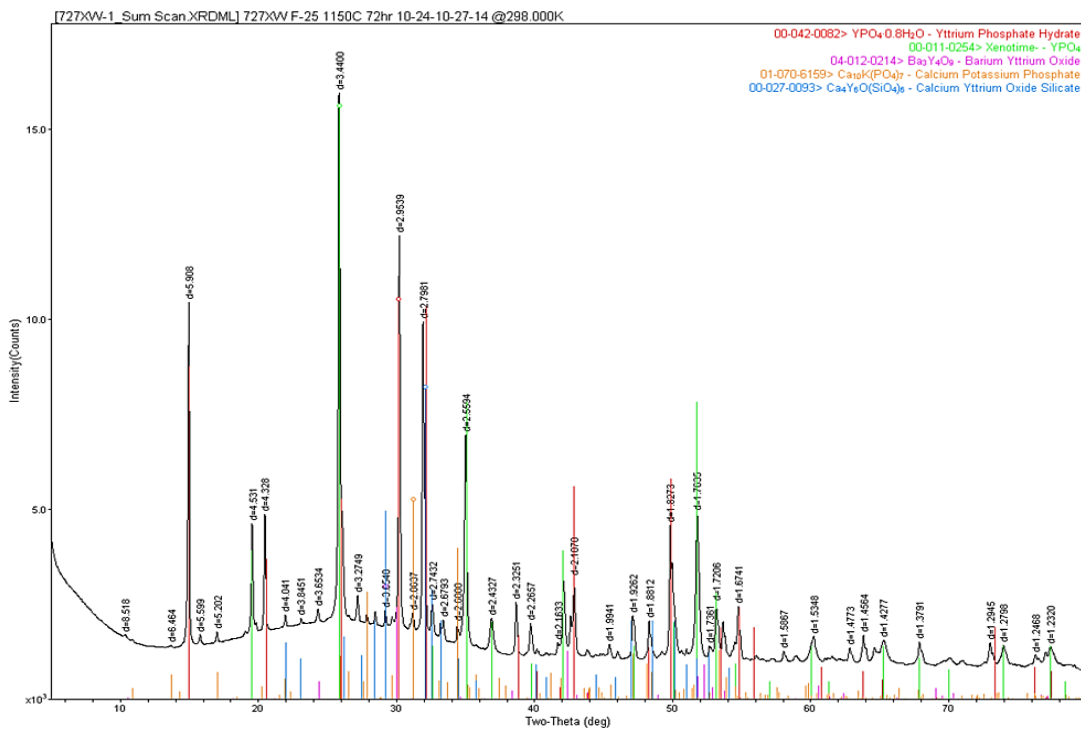


Figure 68. Powder XRD trace with phase ID.

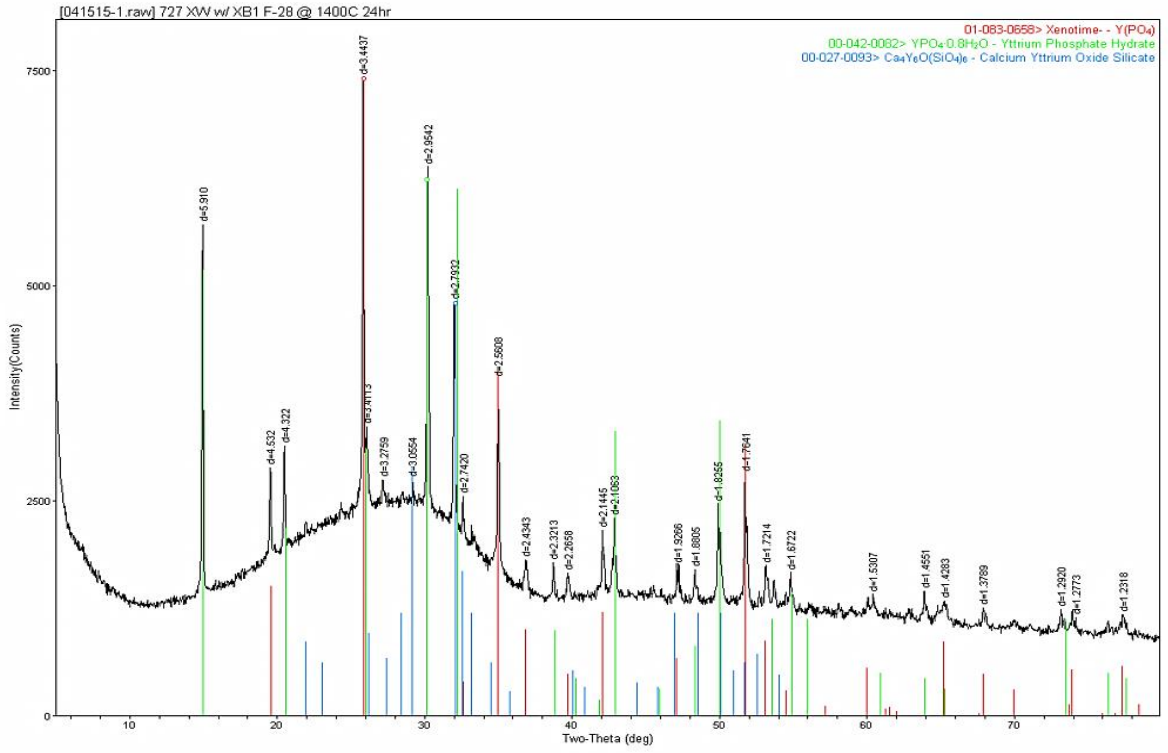


Figure 69. Powder XRD trace with phase ID.

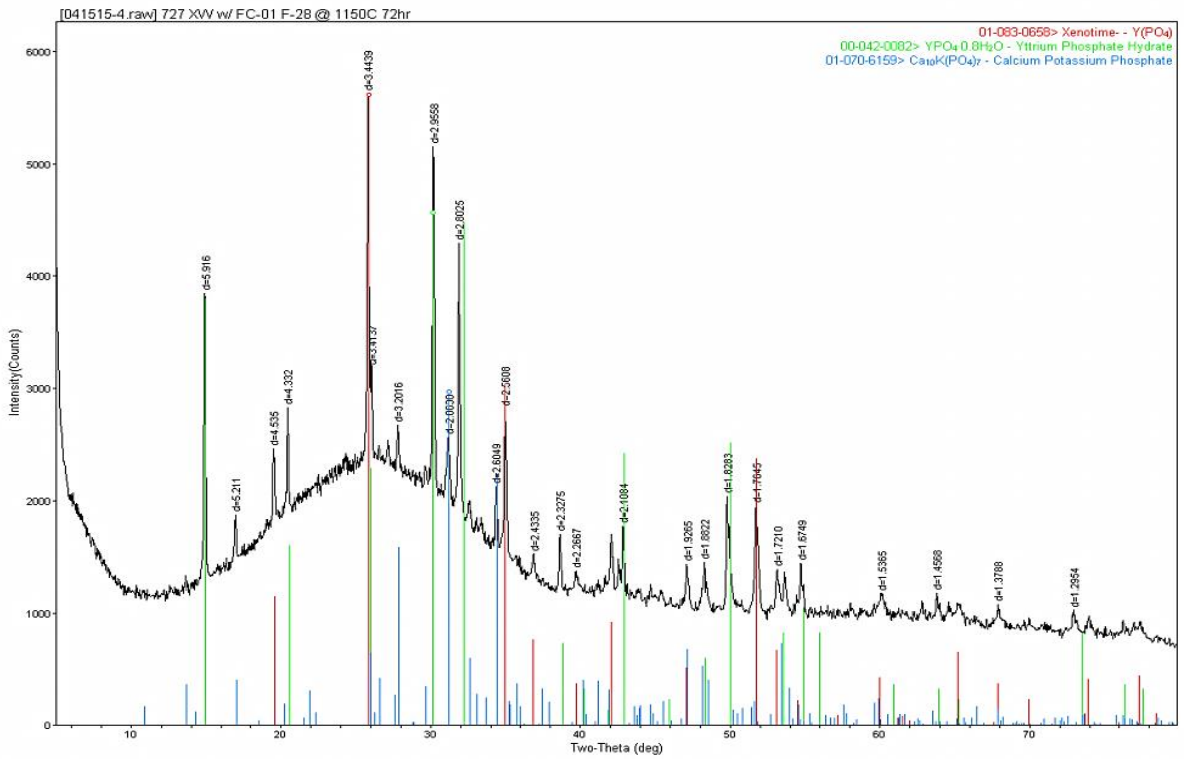


Figure 70. Powder XRD trace with phase ID.

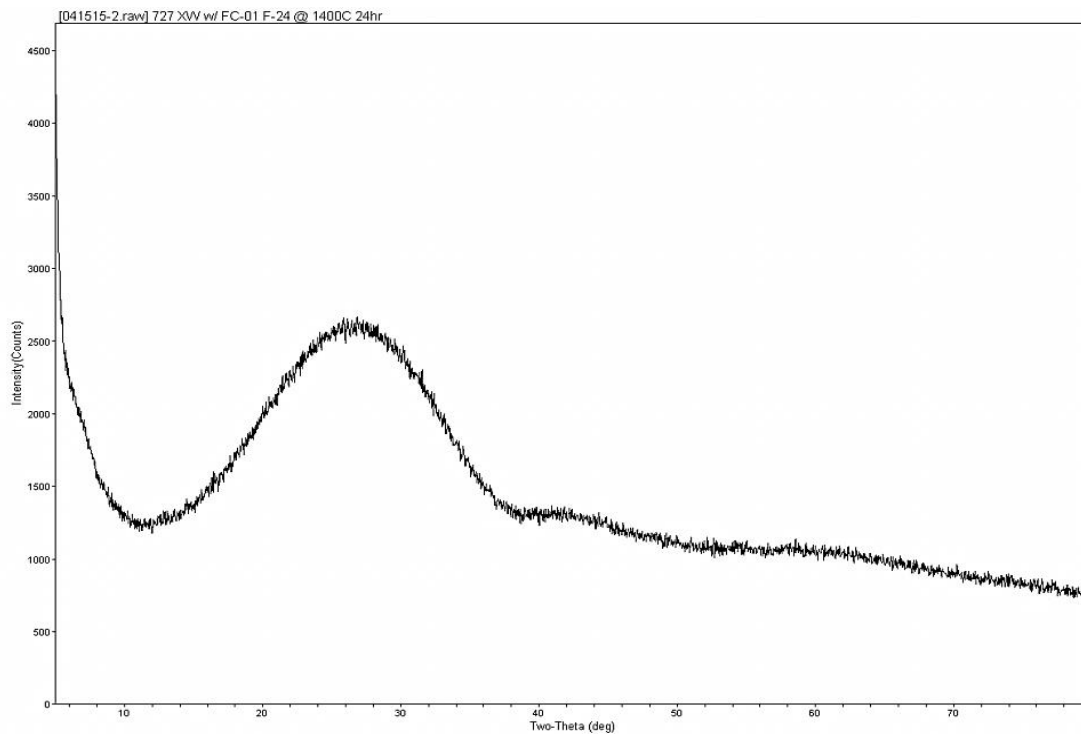


Figure 71. Powder XRD trace with phase ID.

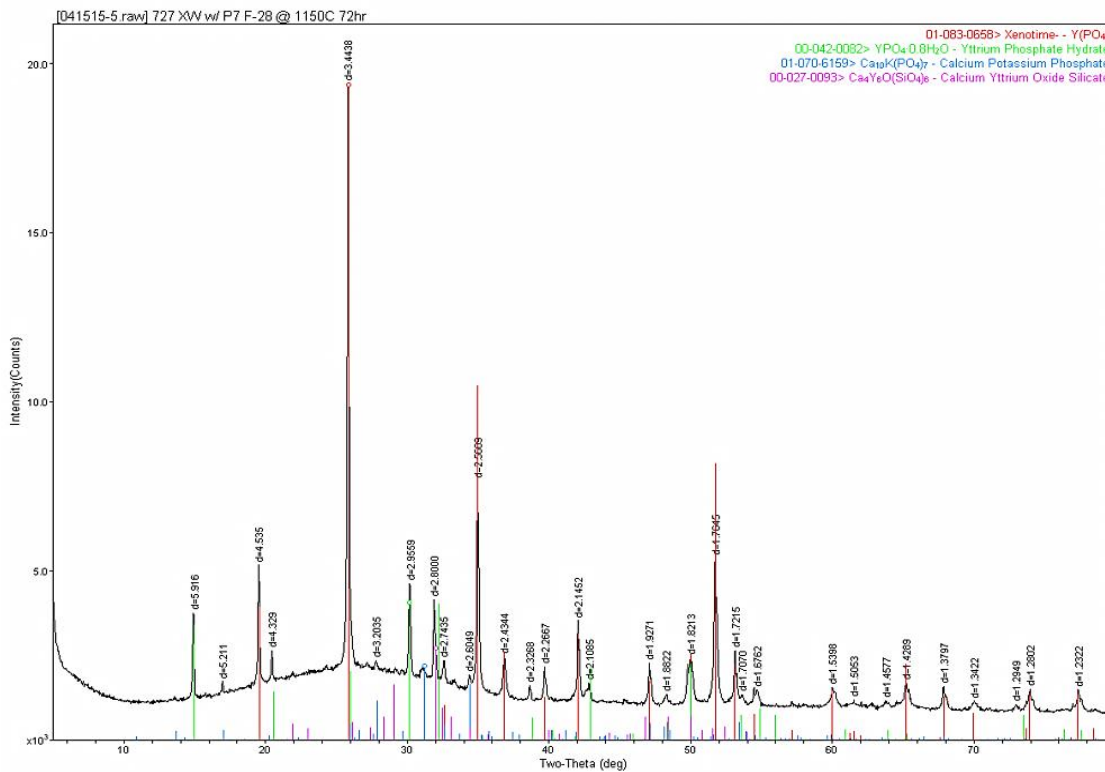


Figure 72. Powder XRD trace with phase ID.

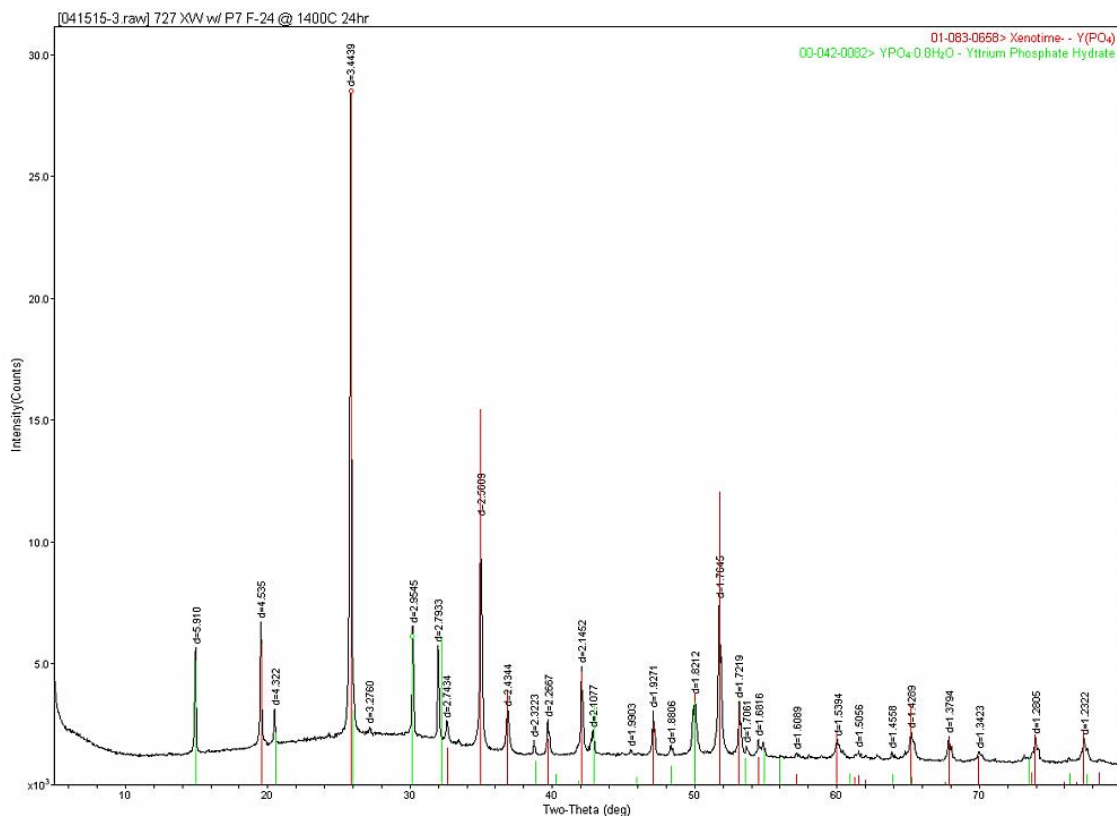


Figure 73. Powder XRD trace with phase ID.

The six samples are compiled in Figure 74 to allow for direct comparison to the others. It is readily apparent that the FC-01 sample exhibited a greater amorphous structure than the others indicating the samples refractory material was easier to melt. The FC-01 samples exhibited the most refractory behavior of the three while the XB-1 samples fell in between the previous two.

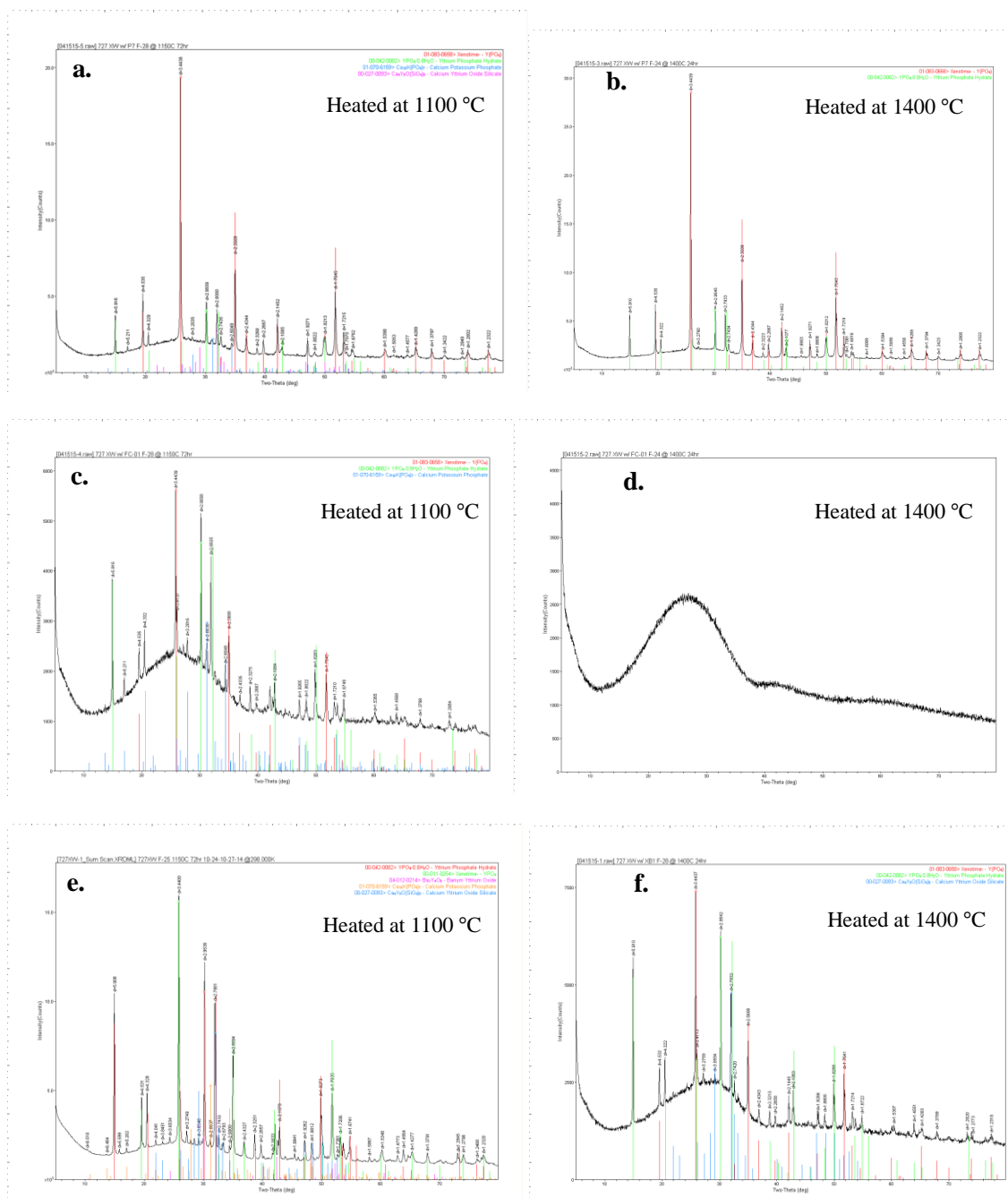


Figure 74. Matrix of XRD traces. P-7 (a, b), FC-01 (c, d), XB-1 (e, f).

The HTXRD sample scans show the strong xenotime peak development as did the previous room temperature scans. When comparing the data from the room temperature scans the peaks are shifted due to the different radiation source, cobalt versus copper.

The HTXRD scans utilized a cobalt radiation source while the low temperature scans were made with copper. The primary xenotime peak for the scans performed in the high temperature apparatus with Co radiation is identified at  $25.91^\circ$  two-theta while the Cu radiation source used on the room temperature scans placed this peak at  $29.922^\circ$  two-theta.

HTXRD scans were extracted and indexed for the data acquired at 1000, 1100, 1200 and 1300 °C as well as the starting and ending room temperature scans. No conclusive identification of phases other than the original xenotime phase were made. Examination of the sequence of scans with increasing temperature did reveal some phase development at higher temperatures; first at  $17^\circ$  two-theta and then at approximately  $36^\circ$  two-theta. Shown in Figure 75 are overlays for the 1100 °C and 1300 °C scans indicating these phase developments.

Comparison was made to the earlier room temperature scans to identify any correlation to these peaks found on the high temperature scans. Results were not definitive but data suggests both sets of these peaks to be associated with the yttrium phosphate hydrate that was identified previously with room temperature peaks identified at  $20.484^\circ$  and  $41.719^\circ$  two-theta. When considering the  $4^\circ$  peak shift for the two different radiation sources, it is plausible these may be the same phase. However, the presence of a hydrate at temperatures in this range would be somewhat remarkable.

Significant work surrounding the synthesis, characterization and thermal behavior of rare earth phosphates was conducted by Lucas et al. , which investigate amongst other things, the hydrated forms of rare earth compounds and their structures.<sup>26</sup> The majority of work focused around lower temperature transformations from the monoclinic hydrated form  $YPO_4 \cdot H_2O$  of churchite type to the anhydrous tetragonal phase  $YPO_4$ . The authors efforts in this previous work revealed the disappearance of the hydrated phase after 2h at 300 °C.

Though no HTXRD was performed in this cited work, it is mentioned of a weight loss occurring in the range of 1100-1300 °C during TGA/DTA experiments. This observance was attributed to the presence of an intermediate yttrium polytrioxophosphate phase formed from  $H_3PO_4$  adsorbed on the surface. Again, the possibility of the formation of a hydrated phase at the suggested temperatures between

1100 and 1300 °C seems unlikely. Nevertheless, there is an obvious development taking place in the HTXRD data which would warrant future work to conclusively identify it.

No positive identification of either the calcium yttrium oxide silicate nor the calcium potassium phosphate was made as a result of the HTXRD scans either at elevated temperature or at room temperature following the high temperature scans. Further, the powder XRD sample prepared from the products resulting from the high temperature scan did not reveal these phases either. This may suggest additional time is required for formation as dwell times during the scan were significantly shorter than the soak times for the powder XRD samples.

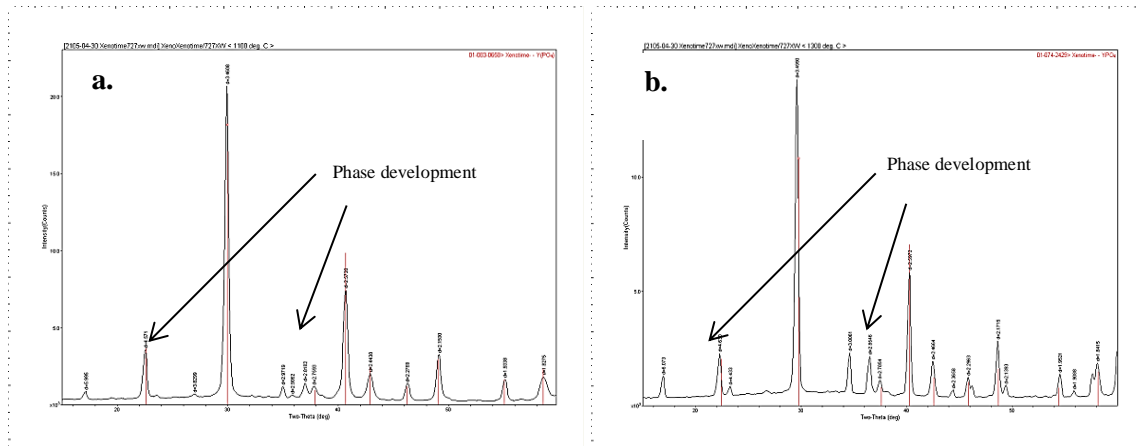


**Figure 75. HTXRD trace with phase development.**

A 3-D overlay was plotted for the HTXRD scans including a room temperature scan prior to heating and a second room temperature scan after the sample had cooled to ambient temperatures. Data from these high temperature scans confirm the development of a phase at about 17° two-theta starting at 1050 °C which continues through the upper range of the scan but begins to fade out at higher temperatures. The strongest peak for this phase appears at 1200 °C. Another set of peaks develops at approximately 36° two-theta as was shown on the individual overlays.

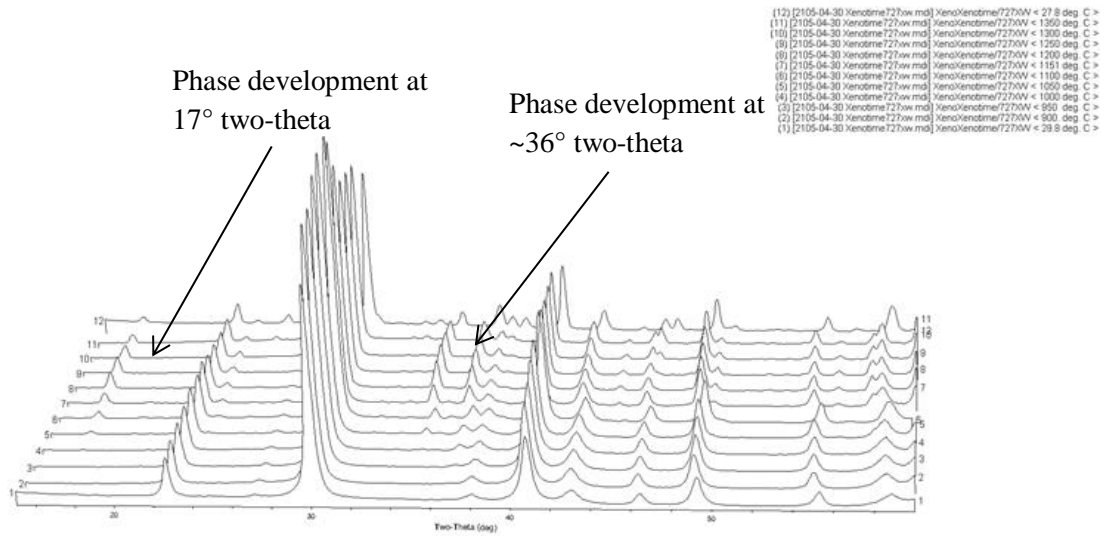
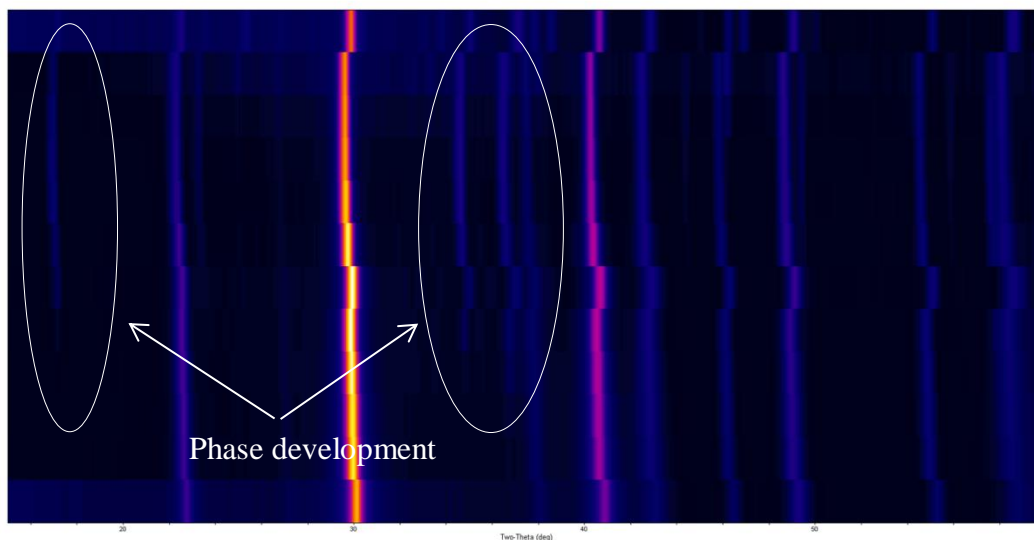


Figure 76. 3-D plot of HTXRD scans.

Results are also presented in a 2-D overlay (Figure 77) for comparison and similarly reveal the phase developments at 17° two-theta and approximately 36° two-theta. As mentioned earlier, a shift due to a slumping of the surface is noted at approximately 1200 °C as well as at the final room temperature scan at the very top. It is not definitively known the reason for the shift but it is suggested some components of the sample liquefied at this temperature or perhaps the sample was somehow physically displaced for the final room temperature scan.



**Figure 77. HTXRD scans are plotted in a 2-D overlay.**

Following the high temperature scan, the sample was removed from the unit and pulverized to perform a room temperature scan on the reaction products. This was performed on a Bruker D8 advanced XRD with Cu radiation source and the results indexed on Jade (Figure 78). Due to the change in radiation source, the peaks are shifted from the HTXRD scans. As was expected, xenotime remained the dominant phase with three strong peaks. The yttrium phosphate hydrate ( $\text{YPO}_4 \cdot 0.8\text{H}_2\text{O}$ ) with a strong peak at  $30.312^\circ$  two-theta in addition to the hydrate suspected to form in ambient conditions, yttrium oxide silicate ( $\text{Y}_{4.67}(\text{SiO}_4)_3\text{O}$ ) and sodium yttrium oxide silicate ( $\text{Na}_{0.5}\text{Y}_{4.5}(\text{SiO}_4)_3\text{O}$ ) were found which were not identified in the earlier powder XRD samples. Ca played an important role in the previous scans but is not found as a contributor to any indexed phases in this scan. Similarly, there is no evidence of phosphate compounds outside of the xenotime of yttrium phosphate hydrate as was determined in the previous samples.

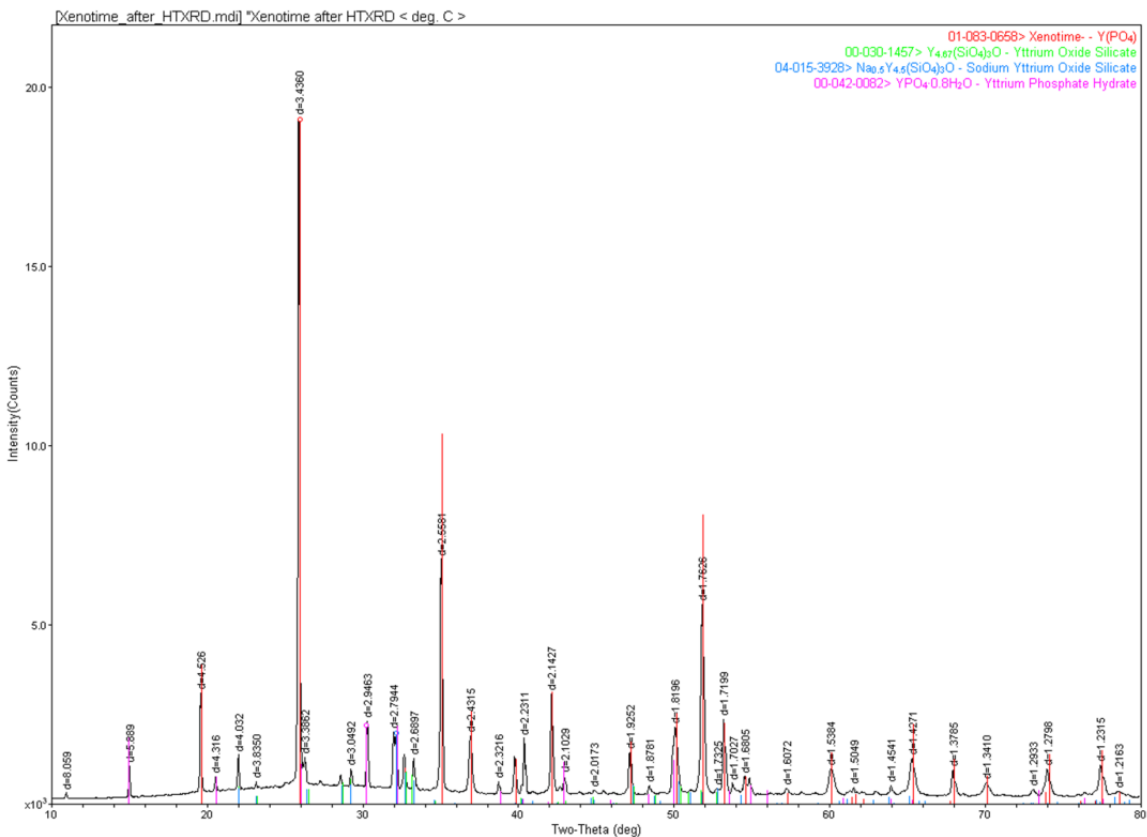


Figure 78. Room temperature scan of HTXRD sample.

Identification of the hydrate in both the RTXRD and possibly in the HTXRD methods proved perplexing. Its potential presence in both room temperature and high temperature scans points more directly to its formation through chemically bonded water in the glass. Similar developments of hydrated REE phosphates have been reported and show similar diffraction peak developments to the work done here.<sup>27</sup> It is just as likely however that humidity was the cause in both tests as it was not positively indexed during the high temperature scans, only in the subsequent room temperature scan of the high temperature components.

Recalling the data from the room temperature XRD scans, the calcium potassium phosphate, Ca<sub>10</sub>K(PO<sub>4</sub>)<sub>7</sub> and calcium yttrium oxide silicate Ca<sub>4</sub>Y<sub>6</sub>O(SiO<sub>4</sub>)<sub>6</sub> phases were identified in the samples subjected to the test temperatures for 72 h while they were not detected in the samples subjected to test temperatures for 24 h. The HTXRD data is collected from scans performed on the sample as it was heated in a period of less than 24

h. This suggests the formation of these phases may be as a function of time and the HTXRD experiment did not allow sufficient time to allow for the phase developments.

During the assessment of the powder XRD room temperature sample which was comprised of the constituents from the HTXRD sample; the identification of two previously unidentified samples was surprising. In addition to the hydrate which was observed in the previous samples, yttrium oxide silicate  $Y_{4.57}(SiO_4)_3O$  and sodium yttrium oxide silicate  $Na_{0.5}Y_{4.5}(SiO_4)_3O$  were both positively identified. It is hypothesized that the difference in heating and cooling rates with the different experimental set-ups between samples prepared for RTXRD and HTXRD are potential causes for these new phases. Again, there are apparent correlations between the different phase developments and the time/temperature to which they are subjected. It is not surprising however that both of these phases were identified. The formation of yttrium silicates has been previously recorded.<sup>3</sup>

### E. Sessile Drop

Images were captured at 10 min intervals over the period of 18 h for the sessile drop tests to allow the glass adequate time to slump and achieve an equilibrium condition (Figure 79). The final image of the sequence was utilized from each sample for post processing analysis.

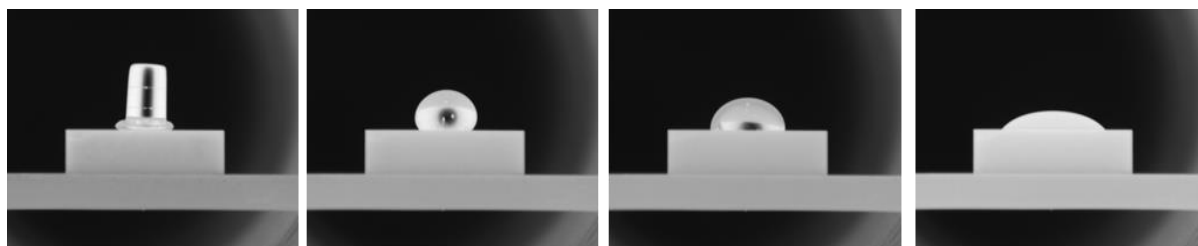
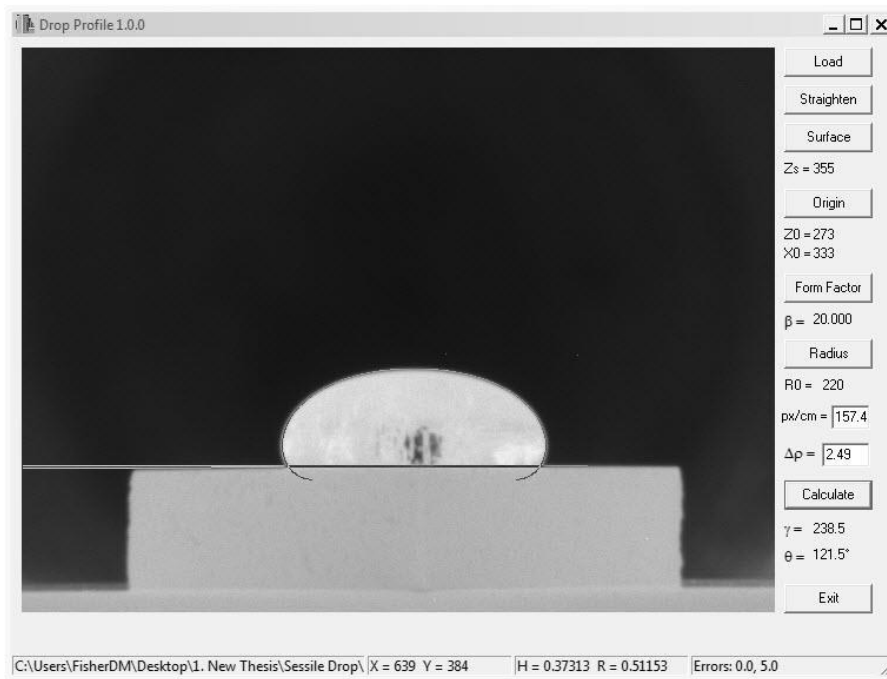


Figure 79. Sessile drop slumping.

Post processing of the sessile drop imagery was performed through an analysis software developed by Dr. Nicolas LeBlond for surface tension measurements through sessile drop tests, Figure 80. The image of interest is loaded into the software and

straightened manually through integrated straightening adjustments. The surface of the substrate is identified at the interface of the refractory and glass drop contact point. The apex of the drop is initially located and aligned with the drop shape outline curve manually. This position was further optimized throughout the shape fitting to achieve a best fit with the actual drop. Adjustments are made visually by adjusting both the form factor  $\beta$  and the radius,  $R_0$  to match the shape outline with the drop shape.



**Figure 80. User interface of the Sessile drop image analysis software.**

The user must enter the pixel/cm distance which is calculated by determining the number of pixels in the y direction that make up the substrate which is known to be 6.35 mm and then converted to a pixels per inch value. Density is added manually from known density measurements. The interfacial tension and contact angle are then calculated for the sample.

The method used is subjective and as such prone to error. Each sample was processed five times and the values of contact angle and interfacial tension averaged in an effort to minimize this subjective error. As a result, the acquired values are being treated as indications of general trends and not absolute values. Though prepared in the same

manner, the surface of the xenotime substrates used was imperfect and likely contained variations from sample to sample which would add error to the results. Dust, porosity and alterations in grain structure all are likely to contribute to these errors.

The as measured contact angle decreases with increased temperature from 41° at 1050 °C to 15.1° at 1250 °C (Figure 81). The sample at 1150 °C does not follow this trend. Values are plotted with an error of two standard deviations. This sample was interrogated and it was found the angle of inclination of the camera likely perturbed the measurement as it was not properly aligned in a horizontal fashion causing a view angle from above rather than perpendicular to the sample interface. The trend indicates a higher degree of wetting associated with the higher temperature samples. This trend supports the increased reactivity of the glass with the refractory with increased temperature as was observed in the SEM samples.

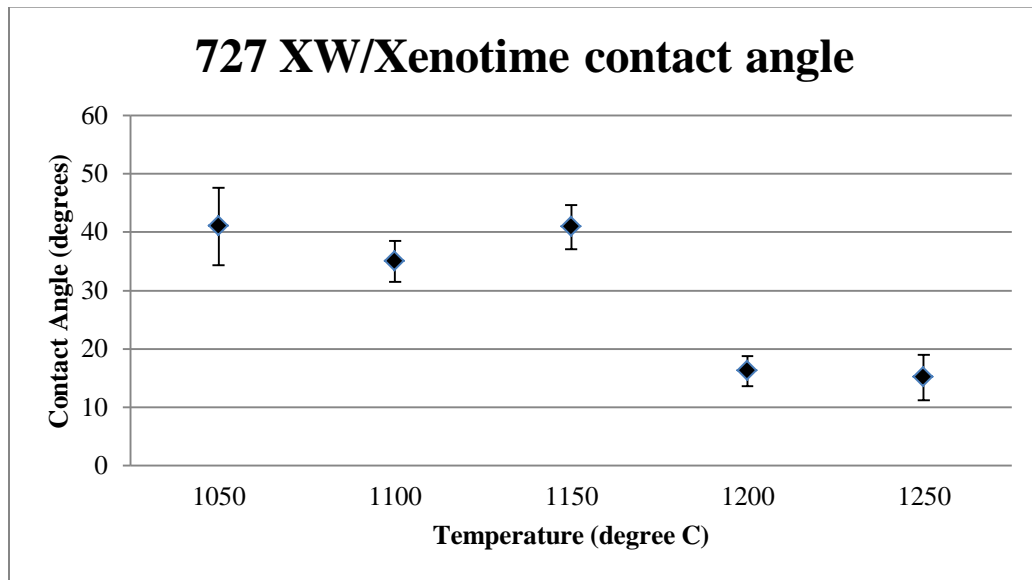


**Figure 81.** Contact angles as measured during the sessile drop experiments for the 727XW glass with xenotime substrate.

Some of the more interesting results were observed in the samples taken of the SLS and 727XW glass compositions with the three refractory compositions (xenotime, A1148 and SCIMOS CZ). As was mentioned in the procedure section, it was necessary to utilize a temperature substantially colder than the previous experiments due to the low

softening temperature of the SLS glass composition. The viscosity of the 727XW composition was therefore significantly higher at this temperature as compared to the SLS viscosity. The contact angle for all three of the 727XW refractory combinations are substantially higher than for the SLS refractory combinations with one exception. Both for the 727XW composition and the SLS composition, the wetting angle for the samples run with the SCIMOS CZ refractory are highest when compared to the A1148 and xenotime samples (Figure 82). The SLS/SCIMOS CZ combination was comparable to the contact angle found on the three 727XW/refractory combinations. Error bars indicate two standard deviations in the data.

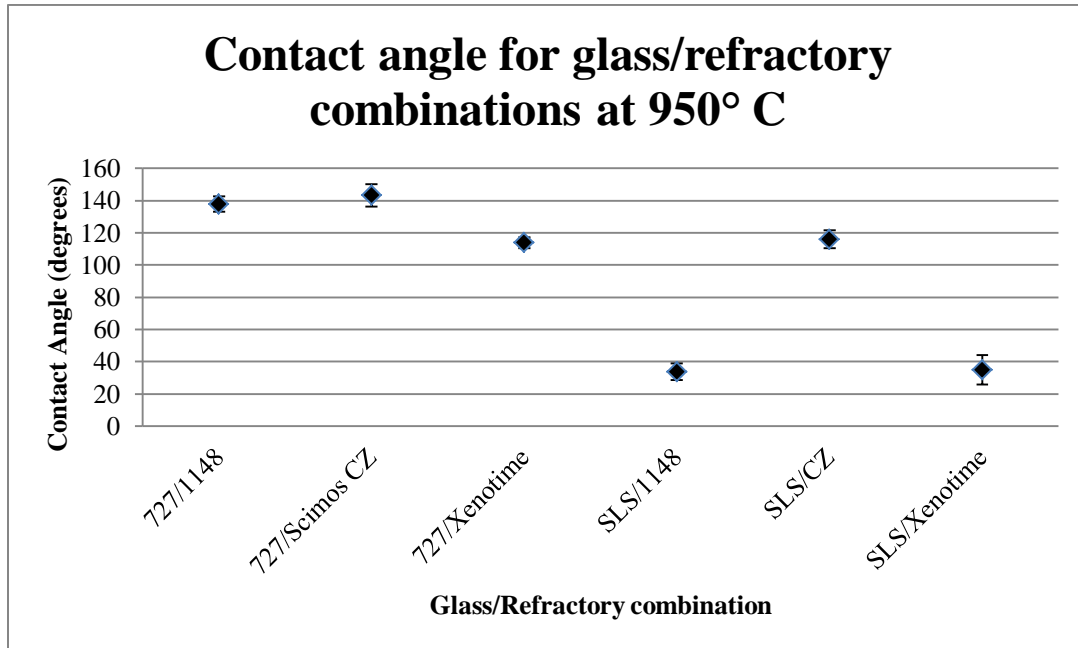
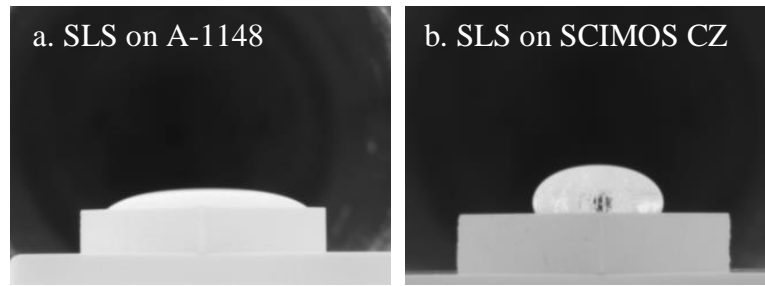


Figure 82. Contact angles as measured for SLS and 727XW glass compositions with xenotime, A1148 and SCIMOS CZ glass contact refractory.

The high corrosion resistance of fused zirconia glass contact is well known of which SCIMOS CZ is one of the foremost brands. The non-wetting behavior of this glass contact with both glass compositions is a strong indicator of its low reactivity to both of these glass compositions, Figure 83.



**Figure 83. Sessile drop tests showed remarkably different wetting behavior between the A-1148 (a.) and SCIMOS CZ (b.) refractories with the SLS glass composition.**

The calculated interfacial tension for the 727XW samples on xenotime refractory exhibited an increasing trend with temperature. The three samples run at lower temperatures are reported near 400 mN/m while there appears to be an inflection between 1150 and 1200 °C followed by a significant increase in the calculated values (Figure 84). It is likely surface volatilization may be the cause of this inflection. It was mentioned previously that volatilization was observed resulting in the devitrification and subsequent failure of a fused silica tube during the test conducted on sample 4 of the 727XW with xenotime sample series. This sample was run at 1150 °C and was the first indication of volatilization for these samples, adding credibility to this claim of glass species volatilization as the reason of this inflection. Volatilization of alkalis in the glass likely resulted in an alteration in the chemistry of the surface of the droplet thereby resulting in this behavior and result.

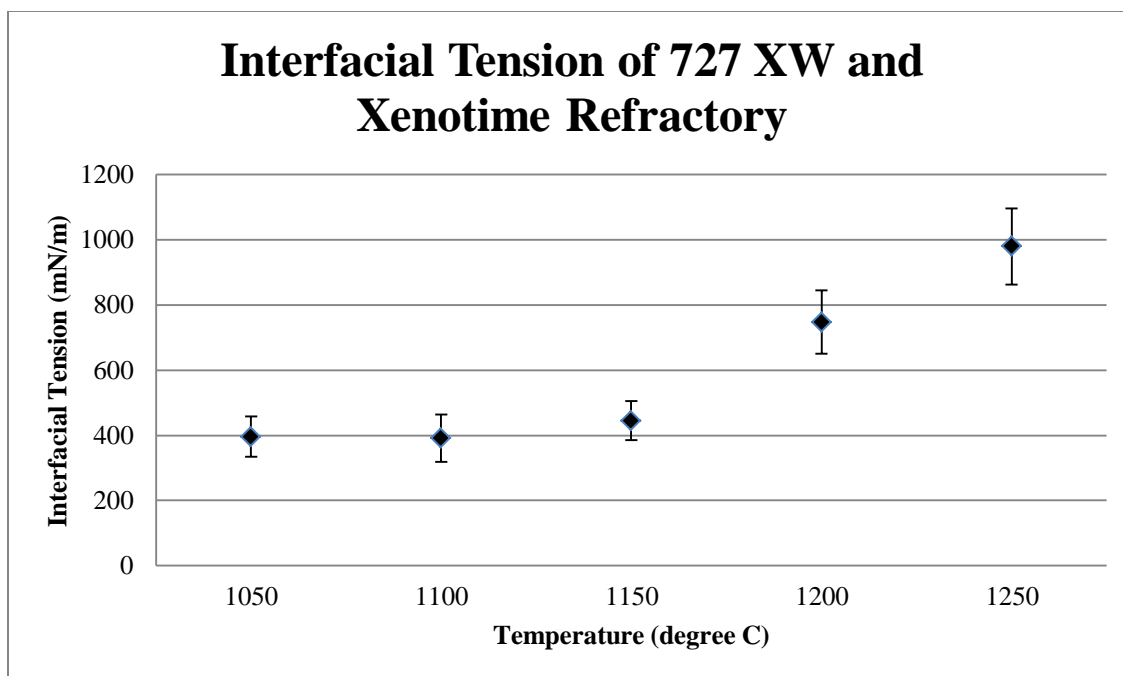


**Figure 84. Calculated interfacial tension for the 727XW on xenotime samples at varied temperature.**

The calculated surface tension for the samples run at 950 °C for the SLS glass and 727XW glass compositions with the three refractories reflect a similar trend to what was observed in the contact angle measurements for these samples. The 727XW samples were centered around 400 mN/m for each of the three refractory types as was the SLS glass sample on SCIMOS CZ. The two SLS glass samples on A 1148 alumina and on xenotime both were substantially higher than the previous four samples. This data is presented in Figure 85 with error bars indicating two standard deviations in the data.

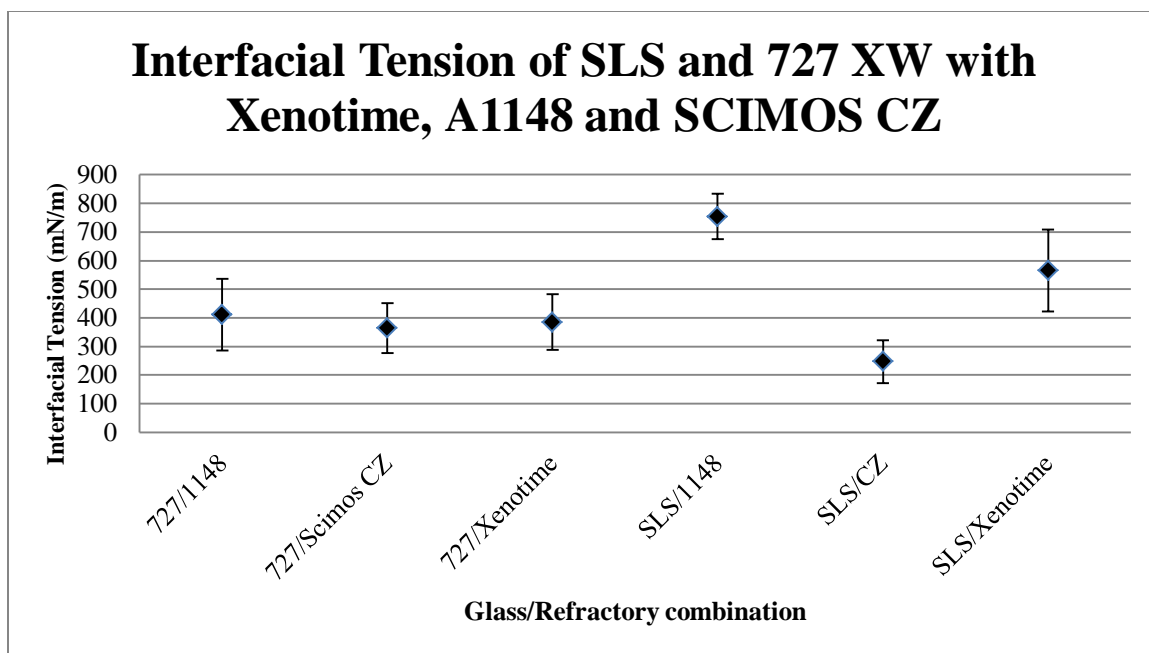


Figure 85. Calculated interfacial tension measurements for the SLS and 727XW glass compositions on xenotime, A-1148 and SCIMOS CZ refractory.

It is worth mentioning that the time-lapse images for each of the samples were observed rapidly in sequence. The sample of SLS glass on SCIMOS CZ exhibited an interesting behavior not observed in the others where obvious reaction was taking place between the glass and the refractory. Blisters were observed coming from the interface of the glass and refractory. SCIMOS CZ is known for producing initial blisters when in contact with glass. Graphite used in the fabrication process of the refractory causes carbon to migrate into the surface of the refractory and upon heating up and contact with glass, the carbon combines with oxygen to form CO<sub>2</sub> blisters. It is believed this is the same process being observed in these frames and would decay as the carbon is depleted from the refractory.

## F. EPMA

EPMA as an analytical technique was not included as part of the original experimental plan for this work. Throughout the course of the investigation, results from the EDS and powder XRD work provided a basis for wanting to pursue EPMA analysis. The data from these two characterizations provided a level of uncertainty which it was

hoped, EPMA could help resolve. Phases were identified in powder XRD with a good level of certainty but this method does not provide any level of detail with respect to positioning within the sample zones. The EDS data also provided some level of uncertainty as to which phase was present owing to the significant concentration gradient. Furthermore, point spectrum data of the crystal phases identified in the glassy regions appeared to include high levels of species from the glass suggesting the spatial resolution of the SEM was not adequate to provide accurate results.

Four distinct regions were interrogated through EPMA; 1) A crystal in the glassy region, 2) a mid-level grey nodule at the reaction interface with the glass, 3) the light grey phase at the reaction interface and 4) a dark grey region within the base refractory (Figure 86). One of the primary interests in this characterization was to identify the chemistry of the light crystals in the glassy matrix (1) in an effort to determine whether they are remnants of the surface layer going into solution with the glass. EPMA analysis revealed very high Si, Ca and Y concentrations with some P and traces of Na, Mg and Sr (Figure 87). This chemistry is significantly different than any collected through the EDS measurements.

Region 2 is characterized by high levels of P, Ca and Na with Mg, Si, Sr and Y. Comparison to the EDS data reveals very similar chemistry to what was observed during those measurements. Data for region 4 reveals it to likely be the same phase as region 2. The data shows a small concentration of Si likely as a result to its proximity to the glassy region and likelihood of some diffusion of the Si ion from the glass, into the base refractory.

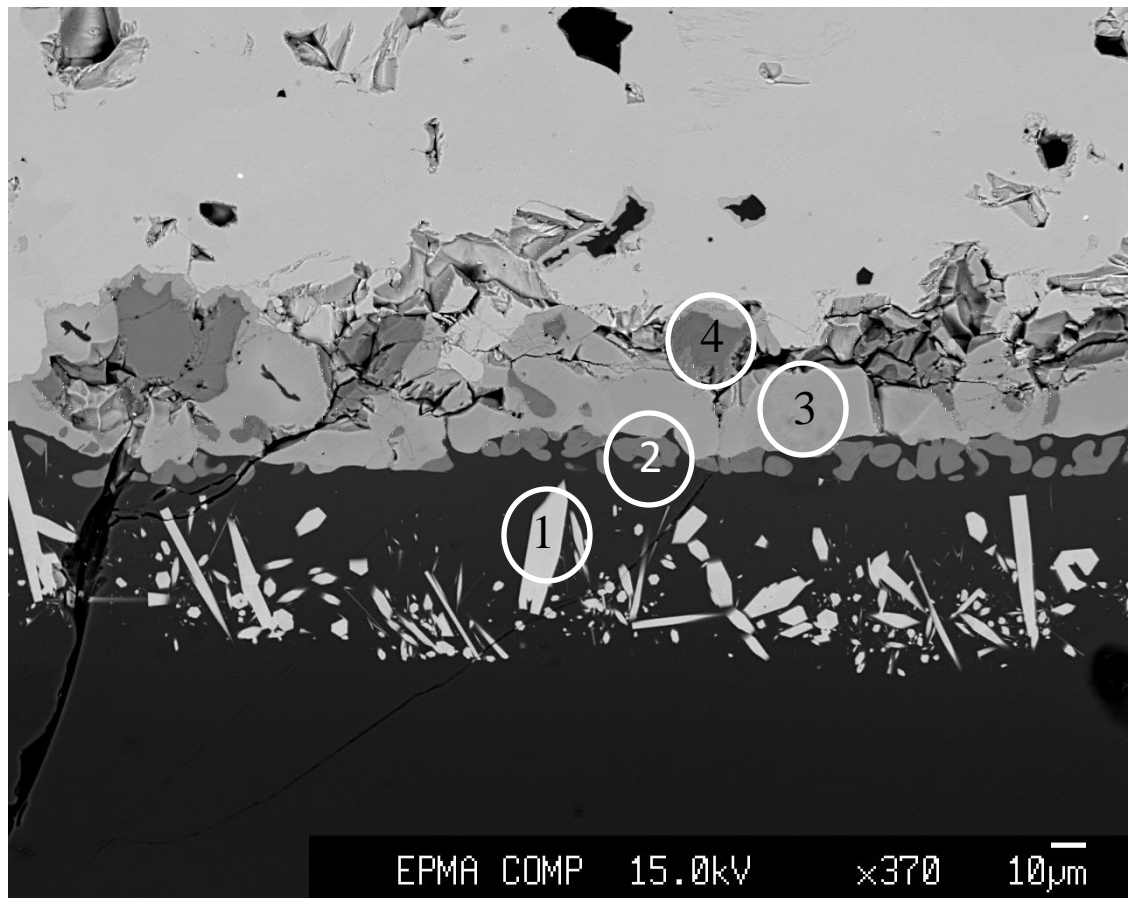


Figure 86. EPMA micrograph showing four regions of interest.

Region 3 represents a major phase which can be found nearly continuous along the glass/refractory interface. It was believed this may be the same phase as the crystal formations found in the glass however data collected through EPMA reveals they contain similar concentrations of Y, Ca, Sr and Na. There exists however, a high concentration of P with a low concentration of Si in region 3 while region 1 (crystal in glass) exhibits high concentrations of Si with low levels of P.

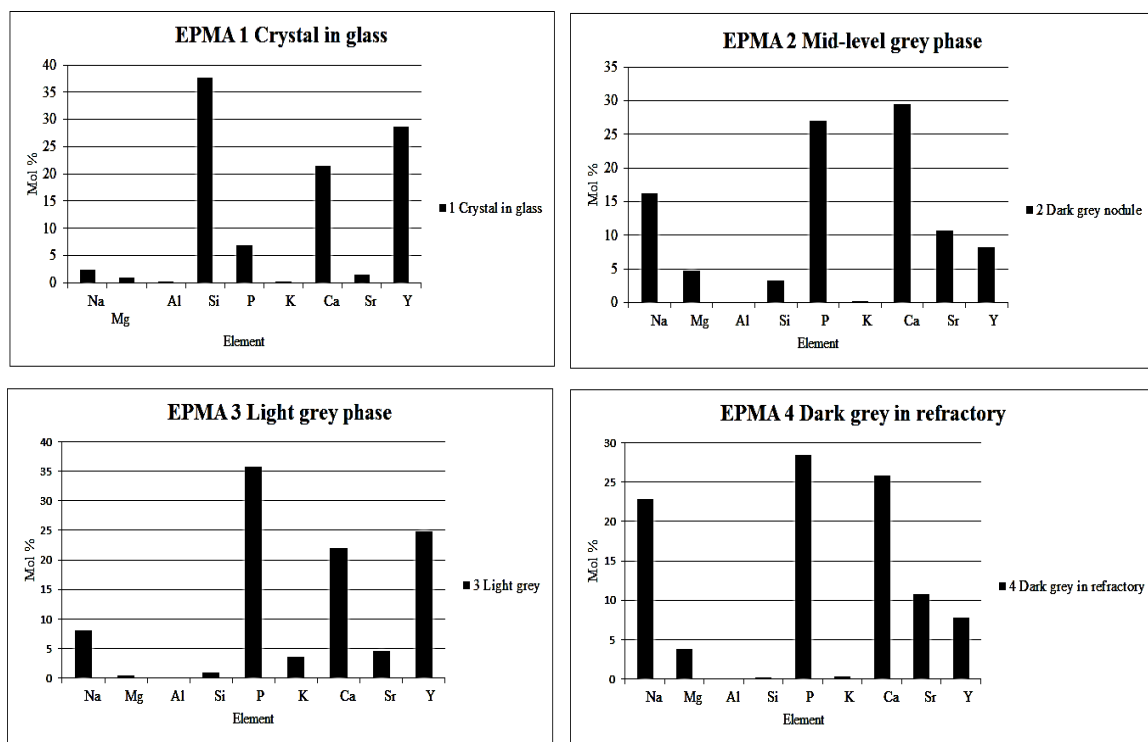


Figure 87. Data from EPMA characterization corresponding to scan locations indicated in Figure 86.

### G. DSC-TGA

Results obtained from the first DSC-TGA sample containing only xenotime refractory powder are shown in Figure 88. The major loss in mass is observed until approximately 500 °C. A mass loss of 1.5 to 2 wt% takes place below 200° C which accompanies the first endothermic peak observed at 128 °C. This first region is associated with the adsorbed surface water on the sample as a result from storage in air. The mass of this water would be associated with the surface area and amount of powder used in the sample. An additional three peaks are observed on the DSC curve at 306 °C, 386.6 °C and 448.6 °C. This region is accompanied by a substantial mass loss of 5-6 wt% and is believed to be due to the de-hydration of the rhabdophane phase (hexagonal  $REPO_4 \cdot nH_2O$ ). There is no indication of significant mass loss or phase change from DSC data detected above 500 °C. The upward slope of the DSC curve following 500 °C is attributed to equipment and the likelihood of the sample heating up faster than the reference.

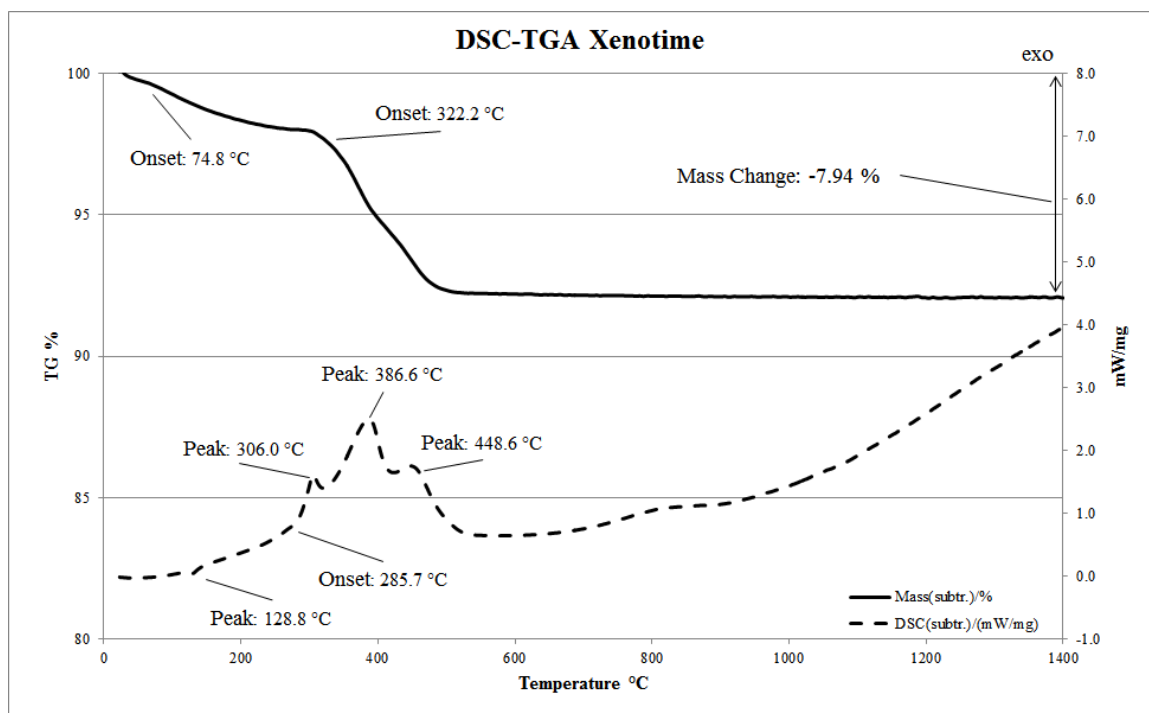


Figure 88. DSC-TGA data recorded on xenotime sample from ambient to 1400 °C.

DSC-TGA results from the second sample containing 727XW glass are shown in Figure 89. The glass transition temperature is extrapolated from the data to be 843.6 °C. The endotherm at 685 °C is not understood. At approximately 1339 °C there is another endotherm followed by an exothermic peak. The reason for this behavior in the base glass is unknown.

The third sample combined equal weights of 727XW and xenotime and DSC-TGA results and are shown in Figure 90. Similarities between data recorded for the first sample (Figure 88) are obvious. Observed are the initial loss in mass attributed to adsorbed water followed by the dehydration of the rabdophane phase. The DSC curve shows a similar occurrence of three exothermic peaks below 500 °C as observed in the xenotime sample. The magnitude of both the mass loss and energy transfer is reduced due to the lower mass of xenotime in the sample. An exothermic peak is observed at 1161.2 °C indicating phase changes taking place in this region. This coincides well with the active crystallization witnessed in the SEM samples earlier in this temperature region. It is not possible however to separate the individual phase developments from this data.

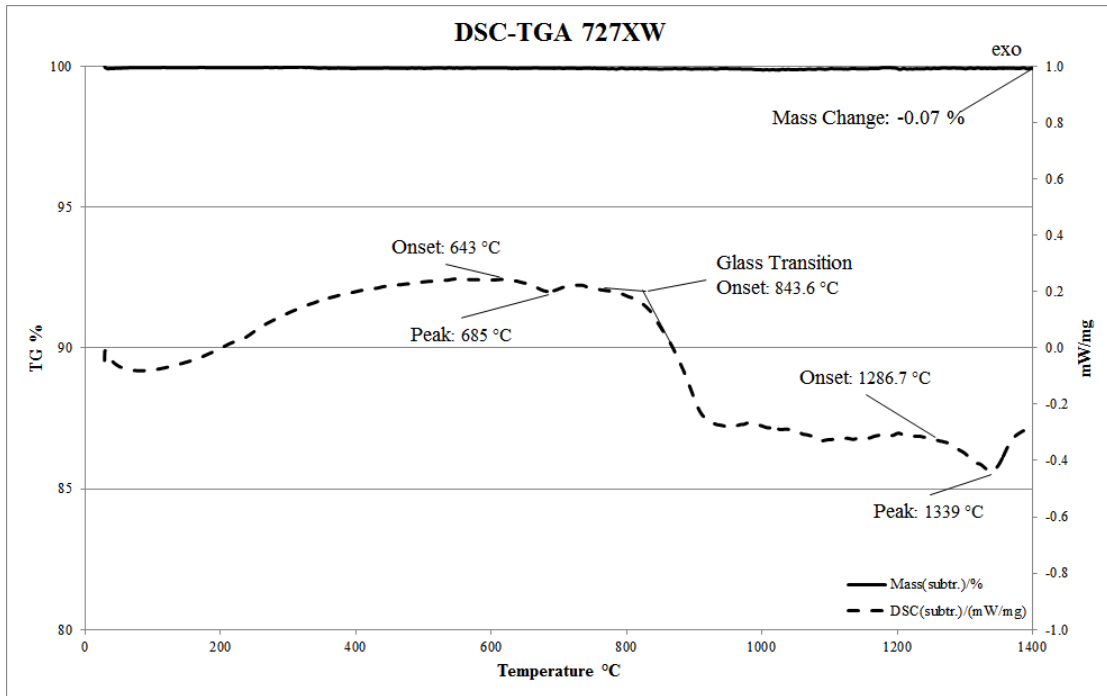


Figure 89. DSC-TGA data recorded on 727XW sample from ambient to 1400 °C.

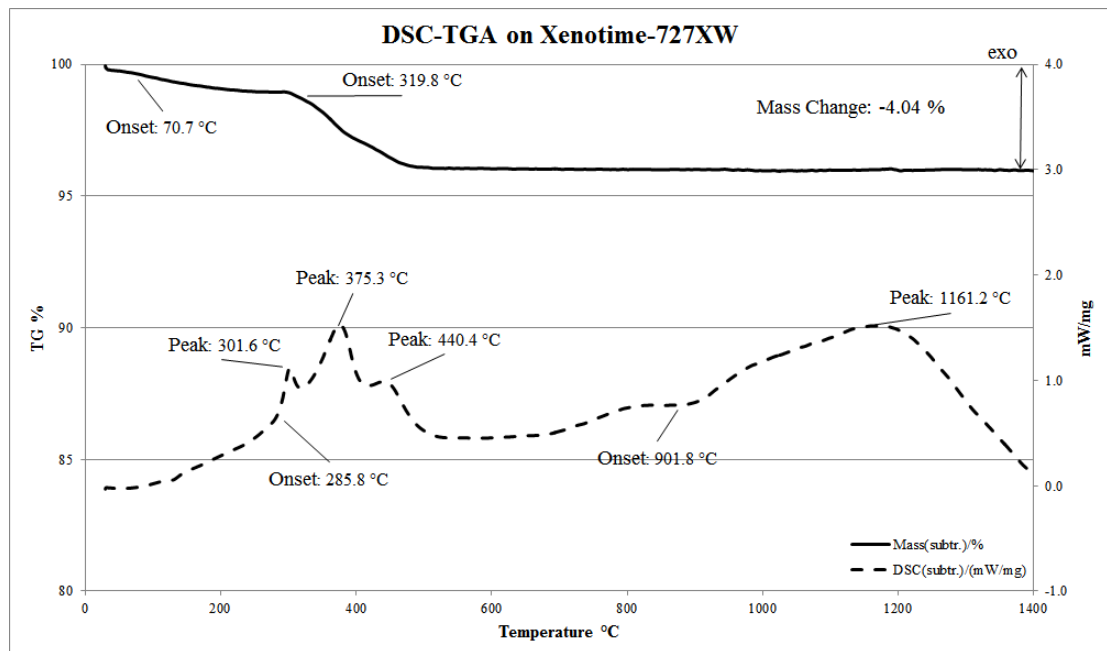


Figure 90. DSC-TGA data recorded on 727XW with xenotime sample from ambient to 1400 °C

## DISCUSSION

Refractory materials used in the glass manufacturing industry must not only be resistant to high temperatures but must also be resistant to corrosion by glass melts. Corrosion by liquid oxides is one of the most severe modes of degradation and limits the lifetime of refractory materials use when in contact with a glass melt. The corrosion process involves phenomena of dissolution and may result in the precipitation of new phases. Development of an understanding of the microstructure of the corroded refractory provides essential information in understanding the applicability of a particular refractory to a process. However, the interpretation of these observations presents significant difficulties.

The phase developments observed through the course of this work represent a complex series of steps which are still not fully understood. In trying to ascertain what phases have formed, it is useful to consider the steps involved in the dissolution process. In understanding the reactions taking place at an interface it is necessary to consider three steps which must take place in order for a reaction to proceed.<sup>28,29,30,31</sup> First, it is necessary for there to be the transport of reaction materials to the reaction interface. Second, there needs to be conditions favorable for a chemical reaction to take place at the interface. Third, there needs to be capability to facilitate transport of the reaction products away from the interface. This third condition of transport away from the reaction surface may not absolutely be necessary in all conditions. The overall rate at which the reaction may takes place is limited by the slowest of these steps.

The dissolution of a solute into a solvent is driven by the reduction of the free energy of the system. In the situation between the 727XW glass and the xenotime refractory, the driving force for dissolution is simply the difference between the concentration of the refractory and the unsaturated glass. Pecoraro suggests a simple model for the dissolution of a pure refractory "A" dissolving into a glass melt "A-B" at temperature  $T_1$ . The difference in free energy is represented by points B and L, Figure 91. This leads to difficulty in the interpretation of refractory corrosion in terms of any activation energy as the driving force for diffusion changes with temperature as shown.<sup>32</sup>

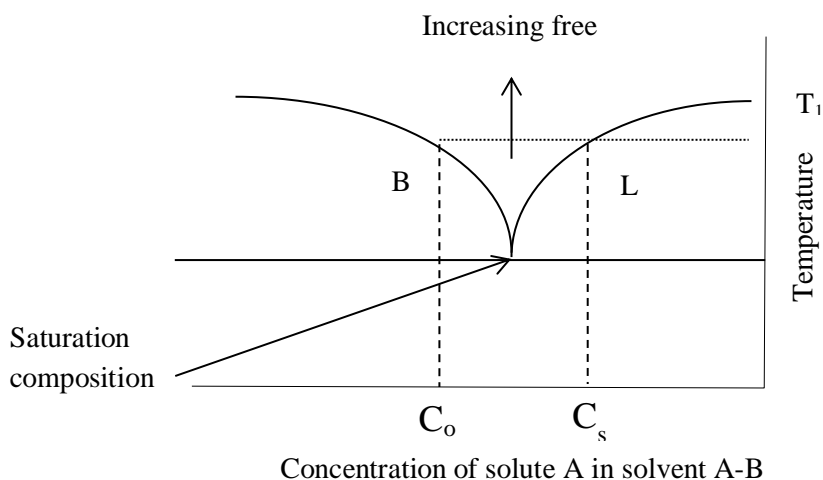


Figure 91. A binary phase diagram of Glass A-B. Refractory is component A.

At the saturation composition, the free energy of the solute equals the free energy of the solution as represented by the liquidus curve for the binary phase diagram. The liquidus temperature determines the amount of solid that can be dissolved into the liquid at a given temperature. As temperature increases, the thermodynamic driving force increases as the difference in free energy increases.<sup>33</sup> Hence, as the glass/refractory system comes under higher temperature, there is a driving force dependent on the reduction of free energy for the system to dissolve and lower its free energy.

We have already discussed the steps necessary for an interfacial reaction to take place. Specific to glass/refractory interface reactions, three additional considerations can be made:<sup>34</sup>

- 1) The solubility of the oxide in the melt.
- 2) The mobility of the reacting species in the melt (ex:  $\text{Na}_2\text{O}$  and  $\text{K}_2\text{O}$ ).
- 3) The mobility of the dissolved oxides in the melt (ex:  $\text{Al}_2\text{O}_3$ ).

The alkali and alkaline earth species will be less strongly bonded to oxygen than aluminum and as such will become the reactive species interacting in the dissolution process with the refractory.

For a glass-refractory reaction layer at lower temperatures, there may be sufficient driving force for ion diffusion to take place to position species at the interface. If however the temperature is insufficiently high so as to limit the glass viscosity and thereby the kinetics of transport of the products of the reaction away from the surface, then the area may become supersaturated and slow the process. Similarly, if mobility of species is limited to the reaction boundary, the reaction may be lacking sufficient quantities even if the glass is at a viscosity sufficient to transport the products away from the interface. Once the reaction has been initiated, material transport phenomena dictate the overall rate in high temperature systems such as a glass and refractory system.

In a glass-refractory reaction layer, the diffusion rate (material transfer) away from the interface may fall into three categories:

- 1) Molecular diffusion
- 2) Natural convection
- 3) Forced convection

If we consider the reaction layer thickness alone, it is obvious that the thickness of this layer would be dependent on the hydrodynamic conditions of the fluid directly adjacent to it. A highly viscous liquid would lead to thicker boundary layers resulting in inhibited material transport while lower viscosities and increased fluid velocities would permit more rapid material transport and result in thinner reaction layers. The dissolution of refractory into glasses generally is associated with higher viscosities and lower velocity therefore thicker reaction layers. In the samples presented here, evidence is presented that suggest these mechanisms at work. It has been shown that a Y rich phase develops on the refractory boundary adjacent to the glass and that as temperatures are increased, this reaction layer begins to dissolve until at the highest temperatures, it appears to go directly into solution with no evidence of the Y enriched layer remaining. Furthermore, the remaining reaction layer is Y depleted and has a greater thickness suggesting the transport of Y to the reaction has become the limiting factor in the reaction. It has been shown that for stationary specimens such as those used in this analysis, it would be expected that in the absence of forced or convective fluid flow

produced by hydrostatic instabilities, the initial rate of transport would be governed by molecular diffusion.<sup>35</sup>

For the 727XW glass composition coupled with the xenotime refractory there are a host of ions ( $\text{Ca}^{2+}$ ,  $\text{K}^+$ ,  $\text{Na}^+$ ,  $\text{Sr}^{2+}$ ,  $\text{Mg}^{2+}$ ,  $\text{Al}^{3+}$ ,  $\text{Si}^{4+}$ ,  $\text{Y}^{3+}$ ,  $\text{P}^{3-}$ ,  $\text{O}^{2-}$ ) diffusing independently of one another or perhaps as complex ions or molecular groups. This high level of complexity makes identification of compositions through the boundary layer extremely complex. Concentration changes through the reaction layer are significant (Si from 54 mol% to 1.8 mol%, Y and P from 50 mol% to 5 mol%) across only a few microns. Effective diffusion coefficients cannot be interpreted in terms of tracer diffusion values without having a thorough knowledge of the relative mobility of the species and how that varies with temperature. To determine these values however would significantly exceed the scope of this work.

Previous work has shown that compared to P, Y diffuses at a faster rate.<sup>36</sup> The Y enriched layer seen in many of the SEM samples would indicate that the higher diffusion rate of Y together with the reduced kinetics of the glass melt at lower temperatures results in a saturation of Y in this region. At elevated temperatures, the rate of transport of the Y away from the interface is increased with improved mobility and this layer eventually goes into solution as the rate limiting factor becomes the quantity of diffusing species from the refractory.

Examining the interface region specific to Sr, Mg, Na, Ca, and K a curious series of depletion and then enrichment is seen. It appears as though a phenomenon of uphill diffusion is taking place for these species in this region.<sup>24</sup> It is suggested that the reason for this odd behavior is the difference in the activity coefficients of these elements in the glass that is enriched with Y and P. A driving force for cations to move into the Y and P enriched glass is provided by an activity gradient established by the dissolving crystals. The concentration of Y at the interface with the glass is indicative of a lower diffusion rate in comparison to P at lower temperature samples. As was seen in the plots of the molar concentrations of Y and P, the two concentrations are equal to one another at high temperatures through the reaction layer. This is confirmation that the two dissolve stoichiometrically into the glass in the absence of limitations of transport away from the reaction interface.

The rapid depletion of Al at the interface is indicative of its slower rate of diffusion. The diffusion coefficient of  $\text{Al}^{3+}$  increases by more than one order of magnitude at high temperatures.<sup>37</sup> In comparison to the alkali and alkaline earth species from the glass, Al concentrations drop dramatically at the reaction layer and there is no evidence of migration into the refractory substrate (Figure 92). As previously mentioned, the Al is more strongly bonded to O in the glass structure than the alkali and alkaline earth species therefore this observation is understood.

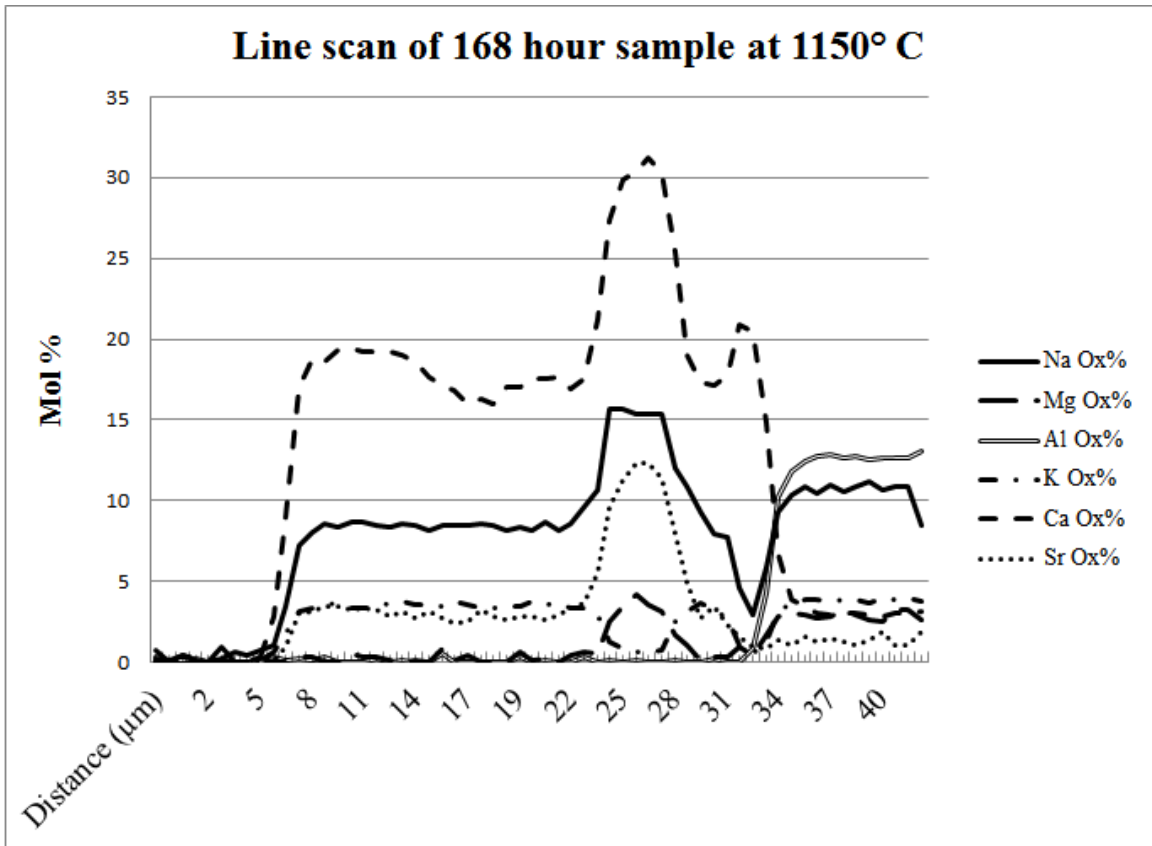


Figure 92. Line scan data plotted relative to alkaline and alkali earth species.

Often a refractory and glass may contain similar species which may contribute to the dissolution process. Such is the case with a zircon ( $\text{ZrSiO}_4$ ) isopipe, which is a compound of zirconia with silica. This refractory and the glass have silica in common. Xenotime however has no species in common as the glass contains neither P nor Y.  $\text{Y}_2\text{O}_3$  however can form compounds with nearly all of the oxides contained in the glass and it has been found to produce two refractory phases  $\text{Y}_2\text{Si}_2\text{O}_7$  and  $\text{Y}_2\text{SiO}_5$ .  $\text{P}_2\text{O}_5$  can

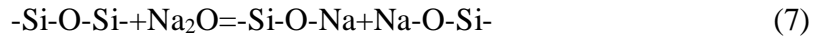
react with Ca to form compounds such as whitlockite ( $\text{Ca}_3\text{P}_2\text{O}_8$ ). Chemically, rare earth metal phosphates exhibit a tendency of forming highly complex compounds with high P contents.

High temperature data is sparse relative to the substitution of  $\text{Y}^{3+}$  with  $\text{Ca}^{2+}$ . It has been found that there is reported data confirming the substitution of  $\text{Ca}^{2+}$  with  $\text{RE}^{3+}$  by the mechanism  $3\text{Ca}^{2+} \rightarrow 2\text{RE}^{3+} + \text{vacancy}$  in the application of irradiation therapy.<sup>38, 39</sup> Treatment of live cancer with radioactive ( $^{90}\text{Y}$ ) yttria aluminosilicate (YAS) glass microspheres has been the preferred method of treatment. Extensive work has been performed in superconducting thin films to understand the effect of the substitution of the  $\text{Y}^{3+}$  ion with  $\text{Ca}^{2+}$  which has similar ionic radius but a lower valence state.<sup>40</sup>

In their hydrated form,  $(\text{MPO}_4 \cdot n\text{H}_2\text{O})$  where the typical stoichiometry of  $n < 3$  exists, the hexagonal rhabdophane crystal structure is adopted by the phosphate.<sup>27</sup> In inorganic hydrates, the water molecules are loosely attached to the compound. There is no chemical reaction involved, and the water is easily released when the compound is heated. In organic hydrates, however, the water chemically reacts with the compound. An inorganic hydrate can release its water molecules, becoming anhydrous, and the anhydrous form of the substance can absorb water, becoming hydrated. The water is known as the water of hydration or the water of crystallization. Xenotime is one of the few phosphate minerals that does not contain water molecules, hydroxides or chlorides. It belongs to an informal group of phosphates called anhydrous phosphates along with monazite, purpurite and lithiophyllite.

The repeated observation of the hydrated  $\text{YPO}_4$  contradicts this and suggests otherwise. Despite the appearance of this hydrate in some of the data revealed here, it is viewed with a significant level of skepticism. Without further testing it is just as likely some other isostructural phase or formation at ambient conditions may have been the reason for its observance. Though it was not possible in this work to positively identify another phase, it has been documented that rhabdophane-type  $\text{YPO}_4 \cdot 0.8\text{H}_2\text{O}$  changes to xenotime-type  $\text{YPO}_4$  above  $900\text{ }^\circ\text{C}$ .<sup>41</sup> No phase change was detected near this temperature in DSC data however, thereby giving some indication that this phase change was not observed in the course of this study.

All of the species involved in this complex reaction are classified as lithophile based on their Goldschmidt classification, readily combining with oxygen. It is not surprising therefore that REE preferentially partitions into silicates. It has been shown that xenotime solubility increases significantly with the per-alkalinity of a glass melt.<sup>3</sup> In the instance where excess Na<sub>2</sub>O or K<sub>2</sub>O are present in a melt, non-bridging oxygen atoms are produced through de-polymerization:



Non-bridging oxygen atoms which were originally coordinated with the Na may then exchange Na<sup>+</sup> against REE<sup>3+</sup>, stabilizing the rare earth cation in the melt as:



The failure of Al to play a role in the observed reaction between the melt and the xenotime refractory may be explained as being a result of the smaller size and higher charge of Al<sup>3+</sup> when compared to the Na<sup>+</sup>, K<sup>+</sup> and Ca<sup>2+</sup> found in the melt. The chemical bond between the Al<sup>3+</sup> and non-bridging oxygens is much stronger and therefore not easily exchanged with the REE<sup>3+</sup>.

A notable feature of the lanthanide series is the lanthanide contraction which is manifested as a systematic decrease in ionic radius when going from light (La) to heavy (Lu) across the lanthanide series. This feature is due to the inner electron f shell being built-up rather than a new shell being added. Because of their slightly larger sizes, LREE are generally less compatible in silicate minerals than the HREE. The heats of formation for this series are reported.<sup>4</sup> Revealed in these measurements is the trend that compounds (LaPO<sub>4</sub>) with larger cations have higher  $\Delta H_{\text{ox}}^{\text{f}}$  than compounds with smaller cations (YPO<sub>4</sub>). A smaller cation such as Y benefits much more than the larger cations by combining with the strong O<sup>2-</sup> ligand. The difference in binding strength between Y-O and Y-PO<sub>4</sub> is significantly larger than the difference between La-O and La-PO<sub>4</sub>. More generally, the smallest cation will tend to associate itself with the strongest lewis base while the larger cations will associate with the weakest lewis base. In the context of

xenotime in contact with a silicate melt, this concept may have some significance in predicting the stability of the reaction layer and defining the reaction products as likely being silicates and oxides of the refractory cations paired with phosphates of the common cations in the glass melt. To be sure, a thorough investigation into the heat of formation for these substances would need to be conducted. A large negative value for the free energy of formation  $\Delta G_f$  is indicative of a large driving force for compound formation. Therefore it is possible to correlate such large negative values to a high resistance of the compound to thermal decomposition.

$\text{Ca}^{2+}$  can substitute into the xenotime cation site though rarely more than 10 %. This may partially explain the strong level of penetration observed of  $\text{Ca}^{2+}$  into the refractory. Based on the work of Emden et al, it is surprising to see the extent of diffusion of  $\text{Ca}^{2+}$  into the refractory base.<sup>42</sup> Though it was shown to play a role in maintaining charge balance, the relative large size of the cation  $\text{Ca}^{2+}$  (100 pm) in comparison to  $\text{Y}^{3+}$  should act as a deterrent to significant concentrations in xenotime which appears to contradict the findings of this current work.

Apatite  $[(\text{Ca},\text{REE})_5(\text{PO}_4)_3(\text{OH},\text{F})]$  is a known rare earth mineral. The calcium potassium yttrium phosphate  $(\text{Ca}_{10}\text{K}(\text{PO}_4)_7)$  found in the sample bears similarities with the cation  $\text{K}^+$  likely providing a charge balance to the structure. In his work on rare earth minerals, Tin describes garnets as groups of minerals having similar physical and crystalline properties with the formula  $\text{X}_3\text{Y}_2(\text{SiO}_4)_3$ .<sup>3</sup> In this formula, X represents the divalent ions such as Ca and Y represents trivalent ions such as Al. The REE prefer entering the dodecahedral X-sites by substituting Ca, Mg or Fe. There may be a driving force owed to the formation of apatite which consumes the  $\text{Ca}^{2+}$  ions and lowers the  $\text{P}_2\text{O}_5$  concentration at the reaction interface.<sup>43</sup>

## CONCLUSIONS

The development of phases at the reaction interface between 727XW glass and xenotime refractory is of great complexity. In addition to reaction layers forming on the base refractory, crystals are observed forming in the glassy region adjacent to the interface. Two phases have been identified through a combination of SEM characterization and powder XRD. As was identified in the EPMA data, the crystals observed in the glass possess a significantly different chemistry than that of the light grey boundary layer on the base refractory adjacent to the glass. Utilizing both powder XRD and EPMA results, these crystal formations have been identified as calcium yttrium oxide silicate,  $\text{Ca}_4\text{Y}_6\text{O}(\text{SiO}_4)_6$ . Similarly, the light grey region at the interface between the glass and base refractory is calcium potassium phosphate,  $\text{Ca}_{10}\text{K}(\text{PO}_4)_7$ . These are distinctly different phases and not the result of dissolution of the interface into the glass.

In addition to these two positively identified phases, a third phase was observed but not identified. EPMA data on this phase shows it contains high concentrations of Ca, P and Na with lower levels of Sr, Y and Mg. Yttrium phosphate hydrate was identified in powder XRD samples but is not believed to be associated with any high temperature phase developments.

In the fusion glass industry, applications of Gorilla<sup>®</sup> type glass compositions utilizing xenotime refractory in direct contact with glass is likely to produce significant levels of defect formation. Multiple phases develop at the interface and devitrification is likely to occur. Though xenotime possesses the property of high levels of creep resistance at elevated temperature, its reactivity with these alkali aluminosilicate glass deems it unsuitable for this application.

## FUTURE WORK

In actual operation, the isopipe for a fusion draw is very much part of a dynamic glass manufacturing system. As such, it can be expected there will be a continuous replenishment of glass as flow moves across the refractory interface. All glass tests performed in this work provide a static system. Although these static tests may serve well in the exploration of phase development and understanding the development of reaction interfaces, they do not provide insight into the rates of corrosion and implications for this continuous replenishment.

Significant time was devoted to the identification of phases but often the results were convoluted due to the significant number of species involved and the small size of specific regions and features. A significant drawback of the electron characterization techniques utilized here is the relatively large interaction volume associated with them. Despite attempts to quantify chemistry with the EPMA, certain regions remain unsolved. It would be appropriate to employ other characterization methods such as the TEM where a thin section may be utilized so as to minimize this interaction volume with the sample.

The identification of yttrium phosphate hydrate in XRD results presented a significant challenge which even upon completion of this work remains not 100 % solved. It is believed the identification of this phase in powder XRD samples is likely as a result of ambient humidity being absorbed. With the temperatures involved in this study it is the opinion of this author and others who were consulted in this field that the temperatures at which this was detected exceeds practical limitations for its existence. It is possible that a previously unknown phase is present which is isostructural with the hydrate form has formed. It is suggested that work be performed to isolate and identify this phase. Additional HTXRD experiments in a purged atmosphere to control moisture in the sample may aid in isolating or eliminating it entirely. Water is well detectable through the use of infrared spectroscopy. It is suggested that any future work include measurements made through FTIR spectroscopy to identify water molecules in the samples. Hydrated samples make for excellent candidates for this type of examination.

The complexity of the system developed between 727XW glass and xenotime refractory was evident from the early stages of this work. Numerous active species were

identified at the reaction interface and there is evidence of uphill diffusion taking place with both Y and Ca. The field of uphill diffusion is developing and this may present for an interesting study of this behavior. Furthermore, significant work remains to develop diffusion coefficients for the dominant species.

It has been mentioned in the discussion that a large negative value for the free energy of formation  $\Delta G_f$  is indicative of a large driving force for compound formation. Therefore, it is possible to correlate such large negative values to a high resistance of the compound to thermal decomposition. In the role of refractory consideration, it may be possible to build on this information to aid in the identification of refractory materials and compatibility with specific glass compositions. Some work has been done utilizing the Material Genome Project (MGP) data base for the calculation of  $\Delta G_f$ . This could be applied to the species identified in the xenotime and monazite structures to better understand their corrosion behavior.

It is worth noting that the experiments conducted within this work utilized samples prepared in a static state. Commercial applications of xenotime materials for glass contact application are most likely to be in use in dynamic systems. It would be appropriate to create experiments which enable the development of samples which capture this dynamic interaction for analysis. The flow of glass over the materials as would be the case for the application with an isopipe is very likely to contribute to advanced corrosion of the refractory as the products of reaction are washed away and new glass is introduced into the system. It is suggested that measurements of rates of corrosion also be incorporated into any dynamic tests in order to capture data relative to the life expectancy of xenotime in this dynamic environment.

With regard to the sessile drop experiments, some interesting results were recorded between the SLS sample and SCIMOS CZ refractory. Further study of this is warranted to understand the wetting behavior of this refractory with more glass compositions. It would also be useful to perform this test in isoviscous conditions. The significant difference in viscosity between the SLS and 727XW glass compositions may have contributed to erroneous results.

## REFERENCES

- 1 J.J. McIntosh, "High delivery temperature isotope materials," U.S. Pat. 8028544, August 2010.
- 2 H.T. Godard, C.W. Tanner, M. Wallen, and E.M. Wheeler, "Refractory materials," U.S. Pat. 8383537, February 2013.
- 3 Q.D. Tin, "Experimental studies on the behaviour of rare earth elements and tin in granitic systems;" Eberhard-Karls-Universitat, Tubingrn, 2007.
- 4 S. V. Ushakov, K.B. Helean, and A. Navrotsky, "Thermochemistry of rare-earth orthophosphates," *J. Mater. Res.*, **16** [May 2015] 2623–33 (2001).
- 5 W. Szuszkiewicz and T. Znamierowska, "Phase equilibria in the system yttrium oxide-phosphorus pentoxide," *Pol. J. Chem.*, **63** [4-12] 381–91 (1989).
- 6 B. Rasmussen, I.R. Fletcher, and J.R. Muhling, "Response of xenotime to prograde metamorphism," *Contrib. to Mineral. Petrol.*, **162** [6] 1259–77 (2011).
- 7 C.J. Hetherington, M.J. Jercinovic, M.L. Williams, and K. Mahan, "Understanding geologic processes with xenotime: Composition, chronology, and a protocol for electron probe microanalysis," *Chem. Geol.*, **254** [3-4] 133–47 (2008).
- 8 Yunxiang Ni, J.M. Hughes, and A.N. Mariano, "Crystal chemistry of the monazite and xenotime structures," *Am. Mineral.*, **80** [1-2] 21–6 (1995).
- 9 R.S. Hay, P. Mogilevsky, and E. Boakye, "Phase transformations in xenotime rare-earth orthophosphates," *Acta Mater.*, **61** [18] 6933–6947 (2013).
- 10 H.J. Forster, "The chemical composition of REE-Y-Th-U-rich accessory minerals in peraluminous granites of the Erzgebirge-Fichtelgebirge region, Germany. Part II: Xenotime," *Am. Mineral.*, **83** [11-12 PART 1] 1302–15 (1998).
- 11 R. Hay and P. Mogilevsky, "Deformation Mechanisms in Refractory Rare-Earth Phosphates;" in *Symp. BB – Mech. Mech. Deform. Brittle Mater.* 2005.
- 12 P.E. Morgan and D.B. Marshall, "Ceramic composites having a weak bond material selected from monazites and xenomites," U.S. Pat. 5514474A, May, 1996.
- 13 E.E. Boakye, R.S. Hay, P. Mogilevsky, and M.K. Cinibulk, "Two phase monazite/xenotime 30LaPO<sub>4</sub>-70YPO<sub>4</sub> coating of ceramic fiber tows," *J. Am. Ceram. Soc.*, **91** [1] 17–25 (2008).

- 14 W. Helfinstine, J. Liebner, D. Martin, J. Neubauer, D. Powell, "Sag Control of Fusion Isopipes Used in Making Sheet Glass by the Fusion Process," U.S. Pat. 8796168, December 2005.
- 15 C. Tanner, H. Godard, E. Wheeler, and M. Wallen, *Yttrium Phosphate-A new material for specialty glass applications and isopipes*. Corning Inc., 2004.
- 16 J. Rustad, *Theoretical Calculation of the Thermodynamics of Spinel, Zircon and Xenotime*. Corning Inc., 2008.
- 17 J.E. Shelby, "Rare Earths as Major Components in Oxide Glasses," *Key Eng. Mater.*, **94-95** 1–42 (1994).
- 18 S.T. Misture, "Large-volume atmosphere-controlled high-temperature x-ray diffraction furnace," *Meas. Sci. Technol.*, **14** [7] 1091–98 (2003).
- 19 Y.Y. Chang and S.Y. Lin, "Surface tension measurement of glass melts using sessile or pendant drop methods," *J. Taiwan Inst. Chem. Eng.*, **42** [6] 922–28 (2011).
- 20 D.A. Weirauch, "The Surface Tension of Glass Forming Melts;" pp. 143–92 in *Prop. Glas. Form. Melts*. Taylor & Francis, New York, 2005.
- 21 Y. Rottenberg, L. Boruvka, and A.W. Neuman, "Determination of Surface Tension and Contact Angle from the Shapes of Axisymmetric Fluid Interfaces," *J. Colloid. Interface Sci.*, **93** [1] 169–83 (1983).
- 22 A. Kucuk, "Structure and the Physicochemical Properties of Glasses and Glass Melts"; Ph.D Thesis. Alfred University, Alfred, NY, 1999.
- 23 J.E. White and D.E. Day, "Rare Earth Aluminosilicate glasses for in vivo Radiation Delivery," *Key Eng. Mater.*, **94-5** 181–205 (1994).
- 24 D. Vielzeuf and A. Saúl, "Uphill diffusion, zero-flux planes and transient chemical solitary waves in garnet," *Contrib. to Mineral. Petrol.*, **161** [5] 683–702 (2011).
- 25 M.B. Wolf and D. London, "Incongruent dissolution of REE- and Sr-rich apatite in peraluminous granitic liquids: differential apatite, monazite, and xenotime solubilities during anatexis," *Am. Mineral.*, **80** [7-8] 765–75 (1995).
- 26 S. Lucas, E. Champion, D. Bregiroux, D. Bernache-Assollant, and F. Audubert, "Rare earth phosphate powders  $\text{RePO}_4 \cdot n\text{H}_2\text{O}$  (Re=La, Ce or Y) - Part I. Synthesis and characterization," *J. Solid State Chem.*, **177** [4-5] 1302–11 (2004).

- 27 T. Anfimova, Q. Li, J.O. Jensen, and N.J. Bjerrum, "Thermal stability and proton conductivity of rare earth orthophosphate hydrates," *Int. J. Electrochem. Sci.*, **9** [5] 2285–300 (2014).
- 28 W.D. Kingery, H.K. Bowen, and D.R. Uhlman, *Introduction to Ceramics*, 2nd ed. John Wiley & Sons, New York, 1976.
- 29 M. Dunkl, A. Gupta, and K. Selkregg, "Formation of Boundary layers on Different Refractories in Glass Melts," *62nd Conf. Glas. Probl. Ceram. Eng. Sci. Proc.*, **23** [1] 211–26 (2002).
- 30 V.L. Burdick, "The Corrosive Nature of Molten Glasses;" pp. 545–61 in *Introd. to Glas. Sci.* Plenum Press, New York, 1972.
- 31 G.A. Pecoraro, "How the Properties of Glass Melts Influence Refractory Materials;" pp. 339–403 in *Prop. Glas. Form. Melts*. Edited by L.D. Pye, A. Montenero and I. Joseph. Taylor & Francis, New York, 2005.
- 32 B.N. Samaddar, W.D. Kingery, and A.R. Cooper, "Dissolution in Ceramic Systems: II Dissolution of Alumina, Mullite, Anthorthite and Silica in a Calcium-Alumina-Silicate Slag," *J. Am. Ceram. Soc.*, **47** [5] 249–54 (1964).
- 33 A.R. Cooper, "Advances in glass technology (Technology papers of the VI International Congress on Glass)," Washington, DC, 1962.
- 34 G.V. McCauley, "Glass and Refractories Symposium," *J. Am. Ceram. Soc.*, **8** [11] 605–10 (1925).
- 35 A.R. Cooper and W.D. Kingery, "Dissolution in Ceramic Systems: I, Molecular Diffusion, Natural Convection, and Forced Convection Studies of Sapphire Dissolution in Calcium Aluminum Silicate," *J. Am. Ceram. Soc.*, **47** [1] 37–43 (1964).
- 36 C.W. Tanner, *Dissolution of Xenotime and Diffusion of Y2O3 and P2O5 in Alkaline Earth Display Glass*. Corning Inc., 2006.
- 37 Y.A. Guloyan and O.M. Pustyl'Nikov, "Diffusion kinetics in the reaction of corundum refractories with a glass melt," *Glas. Ceram. (English Transl. Steklo i Keramika)*, **63** [9-10] 346–350 (2006).
- 38 J.E. White and D.E. Day, "Rare Earth Aluminosilicate Glasses for in Vivo Radiation Delivery," *Key Eng. Mater.*, **94-95** 181–208 (1994).
- 39 H. Zhou and S.B. Bhaduri, "Preparation of Yttrium Phosphate and Yttrium-Doped Calcium Phosphate Microspheres via Hydrated Ions Exchange," *Int. J. Appl. Ceram. Technol.*, **12** E146–51 (2015).

- 40 E.K. Nazarova, A.J. Zaleski, A.L. Zahariev, A.K. Stoyanova-Ivanova, and K.N. Zalamova, "Effects of substituting calcium for yttrium on the superconducting properties of YBa<sub>2</sub>Cu<sub>3</sub>O<sub>z</sub> bulk samples," *Phys. C Supercond. its Appl.*, **403** [4] 283–89 (2004).
- 41 B. V. Emden and M.R. Thorbner, "The Incorporation of Actinides in Monazite and Xenotime from Placer Deposits in Western Australia," *Can. Mineral.*, **35** 95–104 (1997).
- 42 M. Pichavant, J.M. Montel, and L.R. Richard, "Apatite solubility in peraluminous liquids: Experimental data and an extension of the Harrison-Watson model," *Geochim. Cosmochim. Acta*, **56** [10] 3855–61 (1992).
- 43 J. Felsche, "The Crystal Chemistry of the Rare-Earth Silicates," *Structure Bond.*, **13** 99–197 (1973).

